A Path Towards Wearable Affective General Intelligence

Thesis by

Samuel Aaron Solomon

In Partial Fulfillment of the Requirements for

the Degree of

Doctor of Philosophy

CALIFORNIA INSTITUTE OF TECHNOLOGY

Pasadena, California

2025

(Defended April 25, 2025)

Samuel Aaron Solomon

ORCID: 0000-0001-7199-6659

ACKNOWLEDGEMENTS

I would like to extend my deepest gratitude to Professor Wei Gao in affording me the freedom to explore wearable health systems in a holistic and evolving manner during my time under his supervision. From sensor manufacturing, hardware fabrication, and artificial intelligence, this journey has provided me an intimate understanding of wearable platforms and their associated challenges in stability, scalability, generalizability, and user-adoption. By engaging with each component, Professor Gao has helped me build a strong foundation across both research and industrial domains, ultimately shaping my broader career trajectory.

I would like to further extend appreciation and gratitude to my doctoral committee—Professor Wei Gao, Professor Azita Emami, Professor Animashree Anandkumar, and Professor Pietro Perona—for the support, guidance, and technical insights that were critical to forming my doctoral thesis. Your thoughtful feedback and encouragement throughout my time as a graduate student have been invaluable.

I bid a special thanks to my colleagues and collaborators, including but not limited to Jiaobing Tu, Daniel Mukasa, Richard Yao, Jose Lasalde-Ramirez, Yadong Xu, and Ruixiao Liu. Thank you for your mentorship, friendship, and support. The last few years has been especially challenging for me, and I am blessed to have such a strong support network. It has been a privilege to learn, stumble, and grow alongside you.

I would like to reserve a special shoutout to my family, Hanna Haim and Sarah Solomon, whose support cannot be overstated in shaping my outlook and motivation from an early age. To Hanna—thank you for your persistence and commitment to standing by my side, even when others chose to walk away. To Sarah—thank you

for always having my back and being there when I need you, no matter where we are, no matter the problems we may face. Family is something chosen, defined by presence, loyalty, and love—and for that, I am endlessly grateful to you both.

To my grandfather, Melvin Solomon, this dissertation is dedicated to you. Writing these pages in the shadow of your passing on March 21st, 2025, has been incredibly difficult. Your belief in the power of education, and in my ability to pursue it, was unwavering. For that, I am eternally grateful. Thank you for living your life to its fullest and for holding onto it just long enough for me to come home and say goodbye. That final gift is one I will carry with me. I hope this work reflects the legacy you've left behind—one of encouragement, dignity, and pursuit of learning.

תהא נשמתו צרורה בצרור החיים

ABSTRACT

Artificial intelligence continues to support our daily decision-making tasks yet remains disconnected from our dynamic emotions driving these behaviors. Wearable technologies can supplement interactions with continuous emotion biofeedback, but existing models struggle to generalize across emerging biomarkers, platforms, and affective expressions. Here, we introduce a meta-analysis into embedding concurrent fragmented biosignals across 15 medical platforms, spanning five bodily locations, within a single profile that enables efficient and generalizable downstream affective analysis. We achieved this through a Lie manifold neural architecture that simultaneously reconstructs over 118,000 missing biometric details in 205 biomarkers and accurately forecasts 100 affective states across cohorts, questionnaires, and activities. We validated this framework across five datasets to propose a new skin-conformal, soft bioelectronic, affective computing platform that demonstrates closed-loop emotion modulation within thermal, audio, and visual interventions delivered through virtual, holographic, and conversational agents. Our framework establishes a new foundational bidirectional architecture for scalable, interpretable, and emotionally intelligent human-computer interactions.

PUBLISHED CONTENT AND CONTRIBUTIONS

1. Xu, C.; Song, Y.; Sempionatto, J. R.; Solomon, S. A.; Yu, Y.; Nyein, H. Y. Y.; Tay, R. Y.; Li, J.; Heng, W.; Min, J.; Lao, A.; Hsiai, T. K.; Sumner, J. A.; Gao, W. A physicochemical-sensing electronic skin for stress response monitoring. Nat Electron 7, 168–179 (2024). https://doi.org/10.1038/s41928-023-01116-6. S.A.S. and J.L. contributed to the electrochemical and physiological data processing and feature extraction. S.A.S. and C.X. contributed to the machine learning pipeline. W.G., C.X., Y.S., J.R.S., and S.A.S. cowrote the paper.

2. Yu, Y.; Li, J.; Solomon, S. A.; Min, J.; Tu, J.; Guo, W.; Xu, C.; Song, Y.; Gao, W. All-printed soft human-machine interface for robotic physicochemical sensing. Sci. Robot. 7, eabn0495(2022). https://doi.org/10.1126/scirobotics.abn0495. S.A.S. and J.L. contributed to the development of the robotic hand and boat platforms. S.A.S. developed the data analysis and machine learning pipelines. W.G., Y.Y., J.L., and S.A.S. cowrote the paper.

3. Heng, W.; Solomon, S. A.; Gao, W. Flexible Electronics and Devices as Human–Machine Interfaces for Medical Robotics. Adv. Mater. 2022, 34, 2107902. https://doi.org/10.1002/adma.202107902. W.H. and S.A.S. contributed equally to this work.

4. Dao, J., Liu, R., Solomon, S. L. & Solomon, S. A. State Anxiety Biomarker Discovery: Electrooculography and Electrodermal Activity in Stress Monitoring. Preprint at https://doi.org/10.48550/arXiv.2411.17935. S.A.S. conceived the project. S.A.S. and J.D. contributed to data analysis and the development of the machine learning pipeline. S.A.S. and J.D. performed data collection and human studies. S.A.S. and J.D. cowrote the paper.

5. Xu, C., Solomon, S. A. & Gao, W. Artificial intelligence-powered electronic skin. Nat Mach Intell 5, 1344–1355 (2023). https://doi.org/10.1038/s42256-023-00760-z. C.X. and S.A.S. contributed equally to this work.

TABLE OF CONTENTS

LIST OF ILLUSTRATIONS AND/OR TABLES

Chapter 1

INTRODUCTION

1.1 Motivation

Emotions emerge from the continuous interplay between physiological cues and cognitive interpretations[1], dynamically shaping decision-making[2], social interactions[3], and mental well-being. Despite negative affectivity and state-anxiety emerging as prominent long-term risk factors within cardiovascular, immune, and neuroendocrine systems[4], daily emotion management remains largely inaccessible due to costly, sparse therapy sessions that focus on retrospective coping strategies[5,6]. Wearable technologies provide a promising avenue for real-time emotion biofeedback for closed-loop mental health interventions as concurrent reproducible affective and biological states have been observed across the animal kingdom[7], even from individuals without access to sight, sound, and social cues[8]. While autonomic biometric responses present themselves as more reliable affective indicators than speech and text modalities[9–11], monitoring and generalizing affective intelligence across biological domains remains challenging when physiological datasets are temporally fragmented across a growing number of medical platforms, bodily locations, and sampling resolutions. When artificial systems fail to recognize and respond to negative affective cues, users experience frustration and disengagement, diminishing data-driven wellness recommendations[12,13]. Generalizing wearable affective intelligence for personalized mental health interventions will require a holistic

domain-agnostic approach for integrating fragmented temporal signals across emerging wearable modalities and therapies[14], similar to the generalizability and applicability of sentiment text-analysis frameworks[15].

There are significant barriers in translating physiological signals into reliable features for downstream affective analysis. Foremost, wearable platforms struggle to maintain long-term, large-area conformal skin contact, with motion artifacts, perspiration-induced signal degradation, and user discomfort continuing to hinder daily monitoring. Unfortunately, no sensing modality provides a complete representation of affective states, demanding multiple sensors that can span devices and bodily locations. In response, physiological affective datasets have become fragmented across medical platforms, biomarkers, and emotion labels that complicate any universal model generalization strategy. Unlike cognitive computing that benefits from extensively labeled open-source multilinguistic texts[16], wearable affective profiling must contend with limited, context-dependent, and privacy-protected data. This severely limits model scalability, resulting in wearable affective computing for emotion regulation remaining in its infancy. For personalized wellness interventions, wearable systems must maintain a unified approach that integrates diverse datasets across platforms, populations, biomarkers, and affective modalities.

To address these challenges, this thesis proposes a holistic and generalizable hardware–software framework for dynamic affective assessment and

modulation. This framework integrates sensor-rich hardware, advanced data analytics, and machine learning techniques to support the development of responsive wearable computing platforms. The chapters that follow are structured to reflect this interdisciplinary scope and are outlined below.

1.2 Structure and organization

The Human Machine Interface chapter explores the design, fabrication, and integration of wearable electronics within autonomous artificial systems. It begins by examining ultrathin substrates and nanocomposite inks used to create skin-conformal devices, with an emphasis on flexibility, durability, and long-term wearability. Here, we investigate the functionality of these materials within various sensing mechanisms for capturing chemical and physiological information within the context of environmental protection, agriculture, and public health. Communication strategies are applied for real-time, low-power transmission that enable continuous and scalable data exchange with minimal latency. Finally, the chapter concludes with closed-loop feedback for adaptive robotic interventions. This chapter establishes the hardware foundation for responsive medical robotic systems that can be readily adapted to personalized health agents in the subsequent sections.

The Wearable Biosignal Analysis chapter outlines the challenges and current strategies for interpreting physiological signals within human–machine interfaces, with a focus on building robust and generalizable models under

conditions of data scarcity and heterogeneity. This section addresses issues related to data transmission and latency, feature selection, and model complexity. Here, we explore the development of machine learning architectures that support scalable learning and generalization across diverse populations, sensor modalities, and conditions, with an emphasis on cross-dataset validation, domain adaptation, and robustness to distributional shifts in real-world model deployments. Collectively, this chapter establishes the computational foundation for transforming fragmented, noisy biosignals into actionable wellness insights, setting the stage for the Wearable Affective General Intelligence section, where these challenges are addressed through a geometrically grounded learning framework.

The State Anxiety Biomarker Discovery chapter investigates the connections between physiological pathways and behavioral expressions, offering both theoretical and empirical grounding for modeling anxiety-related biomarkers. Here, we focus on two common biometric modalities, electrooculography and electrodermal activity, and demonstrate how transient affective states such as state anxiety can be decoded from multimodal wearable signals. These findings establish the physiological feasibility of emotion profiling, forming a critical foundation for the affective computing framework and biomarkers introduced in subsequent chapters. Overall, this section motivates the development of personalized artificial agents that translate raw biosignals into structured affective representations—paving the way for real-time, wearable affective computing.

The Physicochemical Stress Response Monitoring chapter establishes a wearable affective computing platform for asynchronous state anxiety assessments. We achieve this through the design, fabrication, and validation of a robust biosensing system capable of monitoring pulse, skin temperature, galvanic skin response, three sweat metabolites, and three sweat electrolytes. We couple this skin-interfaced platform with a novel machine learning pipeline that retrospectively classifies different stressors and quantifies state anxiety levels with near-clinical precision. This chapter motivates further state anxiety assessments that generalize across wearable affective computing platforms, enabling research into universal mental health intervention strategies.

The Wearable Affective General Intelligence chapter introduces a novel mathematical and computational framework for learning structured representations of physiological signals. It begins by grounding the reader in the foundations of Lie theory, including Lie groups and manifolds, which provide a geometrically consistent approach to modeling biosignals by preserving temporal structures. Building on this foundation, the chapter presents an intrinsically invertible neural architecture designed to embed wearable biosignals within a Lie manifold, enabling precise signal reconstruction for compact downstream affective analysis. The model supports bidirectional learning, capturing both forward dynamics and latent temporal dependencies while allowing for interpretable two-dimensional decompositions of internal network operations. Applications are demonstrated across five heterogeneous, multi-modal

physiological datasets, showcasing the architecture's capacity to reconstruct over 118,000 missing signals and generalize affective forecasts across populations, activities, and contexts. Together, this chapter establishes a principled approach for embedding time-dependent signals for affective profiling within a unified, mathematically grounded neural framework.

References

1. Schachter, S. & Singer, J. Cognitive, social, and physiological determinants of emotional state. *Psychological Review* **69**, 379–399 (1962).
2. Bechara, A. & Damasio, A. R. The somatic marker hypothesis: A neural theory of economic decision. *Games and Economic Behavior* **52**, 336–372 (2005).
3. Van Kleef, G. A. How Emotions Regulate Social Life: The Emotions as Social Information (EASI) Model. *Curr Dir Psychol Sci* **18**, 184–188 (2009).
4. McEwen, B. S. Physiology and Neurobiology of Stress and Adaptation: Central Role of the Brain. *Physiological Reviews* **87**, 873–904 (2007).
5. Saxena, S., Thornicroft, G., Knapp, M. & Whiteford, H. Resources for mental health: scarcity, inequity, and inefficiency. *The Lancet* **370**, 878–889 (2007).
6. Mongelli, F., Georgakopoulos, P. & Pato, M. T. Challenges and Opportunities to Meet the Mental Health Needs of Underserved and Disenfranchised Populations in the United States. *Focus (Am Psychiatr Publ)* **18**, 16–24 (2020).
7. Darwin, C. EMOTIONS IN MAN AND ANIMALS.
8. Matsumoto, D. & Willingham, B. Spontaneous facial expressions of emotion of congenitally and noncongenitally blind individuals. *Journal of Personality and Social Psychology* **96**, 1–10 (2009).
9. Ekman, P. & Friesen, W. V. Nonverbal Leakage and Clues to Deception†. *Psychiatry* **32**, 88–106 (1969).
10. Vrij, A., Edward, K., Roberts, K. P. & Bull, R. Detecting deceit via analysis of verbal and nonverbal behavior. *Journal of Nonverbal Behavior* **24**, 239–263 (2000).
11. Ekman, P., Friesen, W. V. & O'Sullivan, M. Smiles when lying. *Journal of Personality and Social Psychology* **54**, 414–420 (1988).
12. Chaudhry, B. M. & Debi, H. R. User perceptions and experiences of an AI-driven conversational agent for mental health support. *Mhealth* **10**, 22 (2024).
13. Zhang, Z. & Wang, J. Can AI replace psychotherapists? Exploring the future of mental health care. *Front Psychiatry* **15**, 1444382 (2024).
14. Vos, G., Trinh, K., Sarnyai, Z. & Rahimi Azghadi, M. Generalizable machine learning for stress monitoring from wearable devices: A systematic literature review. *International Journal of Medical Informatics* **173**, 105026 (2023).
15. Souza, F. & Filho, J. BERT for Sentiment Analysis: Pre-trained and Fine-Tuned Alternatives. Preprint at https://doi.org/10.48550/arXiv.2201.03382 (2022).
16. Devlin, J., Chang, M.-W., Lee, K. & Toutanova, K. BERT: Pre-training of Deep Bidirectional Transformers for Language Understanding.

Chapter 2

HUMAN MACHINE INTERFACES

Materials from this chapter appear in "Yu, Y.; Li, J.; Solomon, S. A.; Min, J.; Tu, J.; Guo, W.; Xu, C.; Song, Y.; Gao, W. All-printed soft human-machine interface for robotic physicochemical sensing. Sci. Robot. 7, eabn0495(2022). https://doi.org/10.1126/scirobotics.abn0495."

Ultrasensitive multimodal physicochemical sensing for autonomous robotic decision-making has numerous applications in agriculture, security, environmental protection, and public health. Previously reported robotic sensing technologies have primarily focused on monitoring physical parameters such as pressure and temperature. Integrating chemical sensors for autonomous dry-phase analyte detection on a robotic platform is extremely challenging and substantially underdeveloped. Here, we introduce an artificial intelligence–powered multimodal robotic sensing system with an all-printed mass-producible soft electronic skin–based human-machine interface. A scalable inkjet printing technology with custom-developed nanomaterial inks was used to manufacture flexible physicochemical sensor arrays for electrophysiology recording, tactile perception, and robotic sensing of a wide range of hazardous materials including nitroaromatic explosives, pesticides, nerve agents, and infectious pathogens such as SARS-CoV-2. The fully printable platform decodes the surface electromyography signals collected from the human body through machine learning algorithms for remote robotic control and can perform in situ threat compound detection in extreme or contaminated environments with user-interactive tactile and threat alarm feedback. The printed electronic skin–based robotic sensing technology can be further generalized and applied to other remote sensing platforms. Such diversity was validated on an intelligent multimodal robotic boat platform that can efficiently track the source of trace amounts of hazardous compounds through autonomous and intelligent decision-making algorithms. This fully printed human-machine interactive multimodal sensing

technology could play a crucial role in designing future intelligent robotic systems and can be easily reconfigured toward numerous practical wearable and robotic applications.

2.1 Introduction

The development of advanced autonomous robotic systems that mimic and surpass human sensing capabilities is critical for public health and security[1–3]. Robotic tactile perception enables various task implementations while avoiding harm to the device, user, and environment[4,5]. In addition, embedding autonomous trace-level threat detection can prevent human exposure from toxic chemicals when operating in extreme and hazardous environments, detrimental to human health[6]. Such field-deployable, on-the-spot detection tools can be applied for the rapid identification of minute concentrations of nitroaromatic explosives that pose a health and security threat if they are left unchecked[7–9]. There are numerous toxic compounds that need to be tightly regulated in health and agriculture, such as organophosphates (OPs), which can cause neurological disorders, infertility, and even rapid death[10,11]. Wearable sensing platforms can be extended to monitor pathogenic biohazards such as SARS-CoV-2 without direct human exposure, which could play a crucial role in combating infectious diseases, such as COVID-19 which led to a worldwide pandemic[12–14]. The strong demand for autonomous sensitive hazard detection motivates the development of a controllable human-machine interactive robotic system with both physical and chemical sensing capabilities for task performing and point-of-use analysis.

Because of its high flexibility and conformability, electronic skin (e-skin) presents itself as the ideal interface between electronics and human/robot bodies. In the literature, e-skin has demonstrated a wide range of physical and chemical sensing applications, ranging from consumer electronics, digital medicine, smart implants, to environmental surveillance[15–19]. Despite such promise, several challenges exist for e-skin–based multifunctional robotic systems. Given that most rapid detection approaches for hazardous compounds require manual solution-based sample preparation steps, integrating chemical sensors for autonomous remote dry-phase analyte detection onto an e-skin–based robotic sensing platform is extremely challenging and substantially underdeveloped. However, a robotic manipulator would require tactile, chemical, and temperature feedback to handle arbitrary objects, collect target samples, and carry out accurate chemical analysis in extreme environments[20]. Another problem for e-skin interfaces is that preparing high-performance sensors generally requires manual drop-casting modifications of nanomaterials, which can lead to large sensor variations. Currently, there is a lack of scalable low-cost manufacturing approaches to prepare thin, ultra-flexible, multifunctional robotic physicochemical sensor patches. Additionally, there is a strong need for an efficient human-machine interface that can reliably extract physiological features as well as accurately control and receive real-time user-interactive feedback.

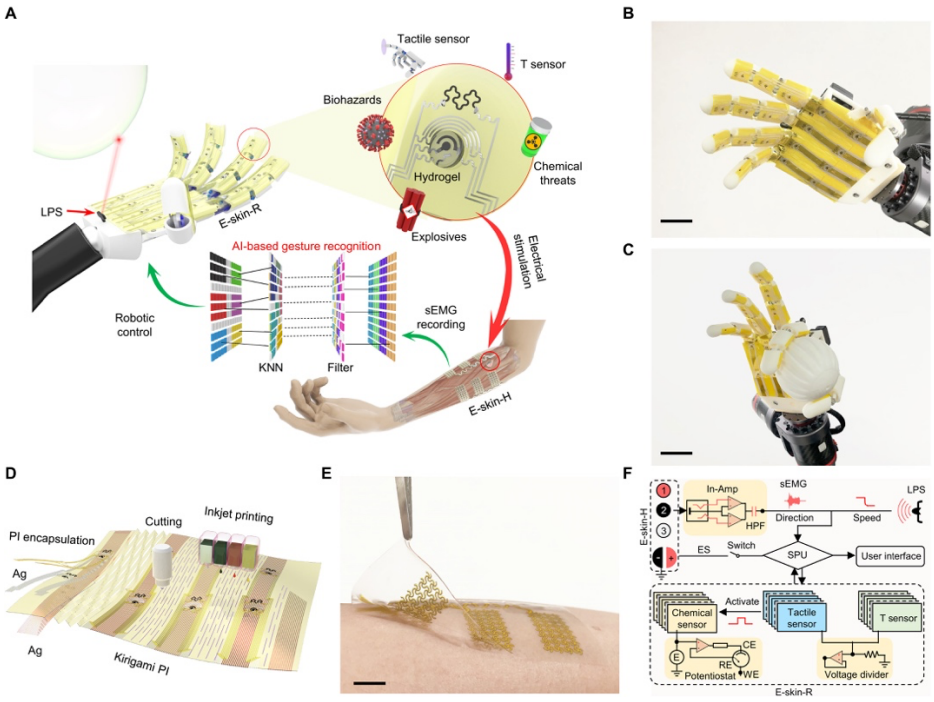

Figure 2.1. AI-powered fully printed soft human-machine interface. (A) Schematic of the M-Bot that contains a pair of fully printed soft e-skins: e-skin-H (interfacing with the human skin) and e-skin-R (interfacing with the robotic skin) for AI-powered robotic control and multimodal physicochemical sensing with user-interactive feedback. T, temperature. (B and C) Photographs of the robotic skin–interfaced e-skin-R consisting of arrays of printed multimodal sensors. Scale bars, 3 cm. (D) Schematic illustration of rapid, scalable, and cost-effective prototyping of the kirigami soft e-skin-R using inkjet printing and automatic cutting. (E) Photograph of the human skin–interfaced soft e-skin-H with arrays of sEMG and feedback stimulation electrodes. Scale bar, 1 cm. (F) Schematic signal flow diagram of the M-Bot. In-Amp, instrumentation amplifier; HPF, high-pass filter; E, applied voltage; ES, electrical stimulation; SPU, signal processing unit. WE, CE, and RE represent working, counter, and reference electrodes of the printed chemical sensor, respectively.

To address these challenges, we introduce an artificial intelligence (AI)–powered, human–machine interactive multimodal sensing robotic system (M-Bot) (**Fig. 2.1A**). The M-Bot consists of two fully inkjet-printed, stretchable electronic skin patches—e-skin-R and e-skin-H—which conformally interface with the robot and human skin, respectively. These e-skins exhibit advanced physicochemical sensing capabilities and are mass-producible and reconfigurable using a high-speed, low-cost, and scalable inkjet printing process, enabled by a suite of custom-developed nanomaterial inks. We further developed a machine learning model capable of decoding surface electromyography (sEMG) signals from muscular contractions—recorded via e-skin-H—for robotic hand control. Simultaneously, e-skin-R supports proximity sensing, tactile and temperature mapping, and real-time hydrogel-assisted electrochemical sampling and analysis of both solution-phase and dry-phase threat compounds, including explosives [e.g., 2,4,6-trinitrotoluene (TNT)], pesticides (e.g., organophosphates), and biohazards (e.g., SARS-CoV-2). Upon detection, real-time haptic and alarm feedback are delivered through electrical stimulation of the user via e-skin-H. The M-Bot's integrated threat sensing and feedback capabilities establish a pathway toward automated chemical detection and machine-mediated decision-making for a wide range of practical robotic assistance applications.

2.2 Results

2.2.1 Design of electronic skin for human-machine interactions

E-skin-R is composed of high-performance–printed nanoengineered multimodal physicochemical sensor arrays that can be placed on the palm and fingers of the

robotic hand (**Fig. 2.1B–C**). The entire sensor patch can be rapidly manufactured in a large-scale and low-cost method via a powerful drop-on-demand inkjet printing technology (**Fig. 2.1D**). On top of e-skin-R are engraved kirigami structures that provide high stretchability without conductivity changes under a 100% strain, which is crucial for any robotic hand with high degrees of freedom in movement. E-skin-H consists of four sEMG electrode arrays (channels), alongside a pair of electrical stimulation electrodes, which can be fabricated similarly with inkjet printing followed by transfer printing onto a stretchable polydimethylsiloxane (PDMS) substrate (**Fig. 2.1E**). With assistance from AI, multimodal physicochemical sensing, and electrical stimulation–based feedback control, e-skin-R and e-skin-H form a closed-loop human-machine interactive robotic sensing system (**Fig. 2.1F**).

2.2.2 Fabrication of fully inkjet-printed multimodal sensor arrays

The multimodal physicochemical sensor arrays on e-skin-R were fabricated via serial printing of silver (interconnects and reference electrode), carbon (counter electrode and temperature sensor), polyimide (PI) (encapsulation), and target-selective nanoengineered sensing films (tactile sensor and biochemical sensing electrodes) (**Fig. 2.2A**). Customized nanomaterial inks were developed to meet the viscosity, density, and surface tension requirement for inkjet printing and to achieve the desired analytical performance. The chemical sensors were coated with a soft gelatin hydrogel that was loaded with an electrolyte or redox probe to facilitate target analyte sampling and analysis in situ. The inkjet-printed carbon

electrodes (IPCEs) showed reproducible electroanalytical performance and rapid response for on-site detection of dry-phase analytes (redox probe Fe3+/Fe2+ was used in the hydrogel as an example). The detection area or resolution can be enhanced by increasing either hydrogel size or electrode density.

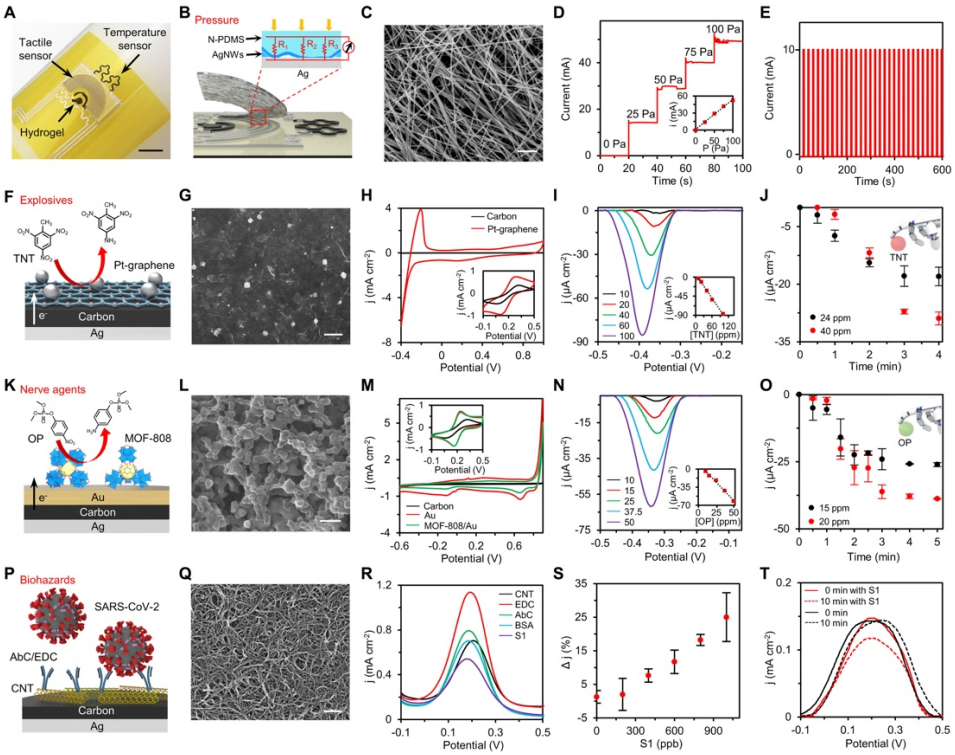

Figure 2.2. Characterization of fully inkjet-printed multimodal sensor arrays. (A) Photograph of a multimodal flexible sensor array printed with custom nanomaterial inks that consists of a temperature sensor, a tactile sensor, and an electrochemical sensor coated with a soft analyte-sampling hydrogel film. Scale bar, 5 mm. (B and C) Schematic (B) and SEM image (C) of the printed AgNWs/N-PDMS tactile sensor. Scale bar, 1 μm. (D and E) Response of a tactile sensor under varied pressure loads (D) and repetitive pressure loading (E). (F and G) Schematic (F) and SEM (G) of the printed Pt-graphene electrode for TNT detection. Scale bar, 4 μm. (H) Cyclic voltammograms (CVs) of an IPCE and a printed Pt-graphene

electrode in 0.5 M H2SO4 and in 5 mM K3Fe(CN)6 (inset). j, current density. (I) nDPV voltammograms and the calibration plots (inset) of TNT detection using a Pt-graphene electrode. (J) Dynamics of robotic fingertip detection of dry-phase TNT using a Pt-graphene sensor. (K and L) Schematic (K) and SEM image (L) of the printed MOF-808/Au electrode for OP detection. Scale bar, 100 nm. (M) CVs of an IPCE, a Au electrode, and a MOF-808/Au electrode in McIlvaine buffer and in 5 mM K3Fe(CN)6 (inset). (N) nDPV voltammograms of the OP detection. Inset: The calibration plots. (O) Robotic fingertip detection of dry-phase OP using a MOF-808/Au sensor. (P and Q) Schematic (P) and SEM image (Q) of the printed CNT electrode for SARS-CoV-2 detection. Scale bar, 250 nm. (R) DPV voltammograms of a printed CNT electrode in 5 mM K3Fe(CN)6 after each surface immobilization step. EDC, 1-ethyl-3-(3-dimethylamonipropyl)carbodiimide; AbC, capture antibody. (S) Calibration plots of the CNT-based sensor for S1 detection. Δj, percentage DPV peak current changes after target incubation. (T) Response of a CNT sensor in the presence and absence of dry-phase S1. All error bars represent the SD from three sensors.

To effectively manipulate objects and to avoid harming either the e-skin or the object, real-time tactile feedback was enabled by incorporating a piezoresistive pressure sensor based on a printed silver nanowires-based (AgNWs)/nanotextured PDMS (N-PDMS) sensing film (**Fig. 2.2B–C**). Such tactile sensation provides the robot with the haptic capability to grasp and handle samples. The geometry changes of the AgNWs/N-PDMS in response to a pressure load change the sensor's conductance (**Fig. 2.2D**). The pressure sensor displayed stable performance under repetitive pressure loading (**Fig. 2.2E**).

To demonstrate the feasibility of using the printed biosensors for hazardous chemical detection, a standard chemical explosive (TNT), an OP nerve agent

simulant (paraoxon-methyl), and a biohazard pathogenic protein from the SARS-CoV-2 virus were chosen. The detection of TNT was achieved using a Pt-nanoparticle–decorated graphene electrode, which was prepared by droplet inkjet printing of aqueous graphene oxide (GO), Pt ions, and propylene glycol and subsequently subjected to thermal reduction. The Pt-graphene showed superior electrocatalytic performance compared with classic carbon and graphene electrodes (**Fig. 2.2F–H**). The reduction of p-NO2 to p-NH2 catalyzed by the Pt-graphene can be detected via negative differential pulse voltammetry (nDPV). The obtained reduction peak amplitude in the nDPV voltammograms showed a linear relationship with the target TNT concentrations with a sensitivity of 0.95 μA cm−2 ppm−1 and a detection limit of 10.0 ppm (**Fig. 2.2I**). Note that a custom voltammogram analysis with an automatic peak extraction strategy was used by the robot to analyze the original nDPV curves. When integrated onto a robotic hand, the hydrogel-coated Pt-graphene sensor could sample the dry-phase TNT efficiently and provide a stable current response within 3 min (**Fig. 2.2J**); the TNT sensor can be regenerated in situ through repetitive nDPV scans to deplete the sampled analyte molecules toward continuous robotic sensing. For OP analysis, Pt-graphene and carbon have low electrochemical activity, because Zr-based metal-organic framework (MOF-808) was reported to have strong interaction with OPs[21,22]. Thus, the printed MOF-808–modified gold nanoparticle electrode (MOF-808/Au) was selected to achieve efficient nonenzymatic OP reduction at a relatively low voltage (**Fig. 2.2K–M**). In this way, the catalyzed reduction of paraoxon-methyl can be monitored via nDPV using the MOF-

808/Au sensors with a sensitivity of 1.4 μA cm−2 ppm−1 and a detection limit of 4.9 ppm (**Fig. 2.2N**). In addition to high sensitivity, these printed sensors could also perform high-concentration threat analysis. Like TNT detection, a 3- to 4-min sampling time was found to be sufficient for stable robotic dry-phase OP analysis (**Fig. 2.2O**). The Pt-graphene TNT sensors and MOF-808/Au OP sensors showed high selectivity over other nitro compounds. Because of the excellent stability of the catalytic performance of Pt-graphene and MOF-808/Au, the printed sensors can perform continuous TNT and OP analysis.

Label-free SARS-CoV-2 virus detection was demonstrated from a printed multiwalled carbon nanotube (CNT) electrode that was functionalized with antibodies specific to SARS-CoV-2 spike 1 protein (S1) (**Fig. 2.2P–Q**). The CNT layer had a high electroactive surface area for sensitive electrochemical sensing while providing rich carboxylic acid functional groups for amine-containing affinity probe immobilization to achieve versatile biohazard sensing. The successful surface modification of the S1 sensor was confirmed after each surface immobilization step (**Fig. 2.2R**). Parts-per-billion level S1 sensing was performed based on the signal change of the electroactive redox probe (Fe3+/Fe2+) caused by the blockage of the electrode surface due to the S1 protein binding (**Fig. 2.2S**). The response variations of such S1 sensors can be further reduced in the future with an automatic surface modification process. The SARS-CoV-2 S1 sensor shows high selectivity over other viral proteins. On-the-spot robotic S1 protein detection was successfully demonstrated using a collection and

detection hydrogel containing the redox probe on the sensor that touched a surface containing a dry blot of the S1 protein (**Fig. 2.2T**). Although the nonspecific adsorption could potentially reduce the selectivity of the hydrogel detection process, the semiquantitative data conveniently and automatically obtained on site by the sensor could still provide the users rapid, real-time feedback and alert on the presence of biohazard.

To ensure accurate hazard detection in extreme operational environments, a printed carbon-based temperature sensor was designed for on-site temperature sensing and chemical sensor calibration during operation. All printed sensors maintained similar performance under and after repetitive mechanical bending tests, indicating their high mechanical stability. The freshly prepared hydrogels can be stored at 4°C in a moist chamber for more than 1 week and maintain similar sensing performance. To minimize the influence of the shearing and normal forces on the sensor performance, the AgNWs/N-PDMS pressure sensor was designed to form a protection microwell for each hydrogel-coated biosensor and to facilitate reliable chemical analyte sample collection; moreover, the tactile feedback from the AgNWs/N-PDMS pressure sensor could ensure stable electrochemical sensing performance (contact pressure was maintained between 0 and 500 Pa during operation).

2.2.3 Evaluation of real-time human-machine interactions

E-skin-H acts as a human-machine interface for autonomous robotic control and object manipulation (**Fig. 2.3A**). E-skin-H achieves this by monitoring neuromuscular activity, which provides an intuitive interface to perform hand gesture recognition, through its inkjet-printed, PDMS-encapsulated, four-channel, three-electrode sEMG arrays (**Fig. 2.3B–C**). Analyzing the interfacial contact with the skin, e-skin-H demonstrates high stretchability with good mechanical compliance during physical activities through its serpentine structure to provide reliable sEMG recordings.

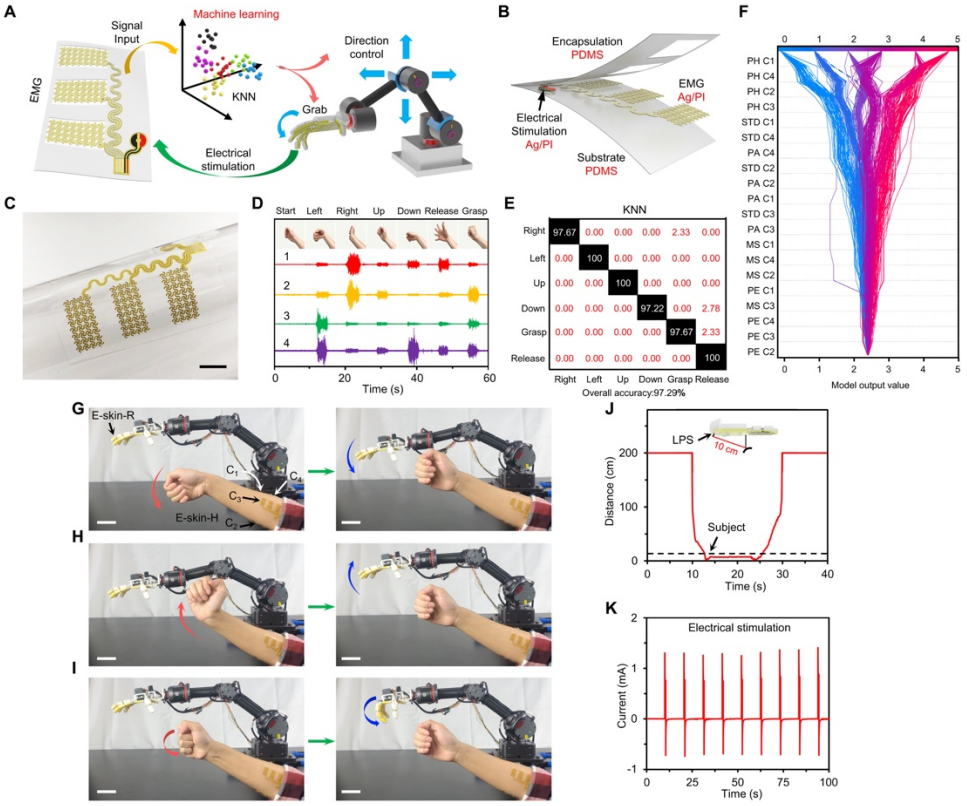

Figure 2.3. Evaluation of AI-assisted human-machine interactions. (A) Schematic of machine learning–enabled human gesture recognition and robotic control. (B and C) Schematic (B) and photograph (C) of a PDMS encapsulated soft e-skin-H with sEMG and electrical stimulation electrodes for closed-loop human-interactive robotic control. Scale bar, 1 cm. (D) sEMG data collected by the four-channel e-skin-H from six human gestures. (E) Classification confusion matrix using a KNN model based on real-time experimental data. White text values, percentages of correct predictions; red text values, percentages of incorrect predictions. (F) A SHAP decision plot explaining how a KNN model arrives at each final classification for every data point using all five features. Each decision line tracks the features contributions to every individual classification; each final classification is represented as serialized integers (that map to a hand movement). Dotted lines represent misclassified points. (G to I) Time-lapse images of the AI-assisted human-interactive robotic control using the M-Bot. Scale bars, 5 cm. (J)

Response of the LPS when the robot approaches and leaves an object. (K) Current applied on a participant's arm during the feedback stimulation.

Upon signal acquisition, various machine learning algorithms were evaluated for accurate gesture recognition including linear regression, random forest, artificial neural networks, support vector machines (kernels: radial, sigmoid, linear, and polynomial), and k-nearest neighbors (KNNs). Each algorithm was shown to extract motor intention from sEMG signals, acting as a bridge between conscious thought and prosthetic actuation. Of all the machine learning algorithms, the KNN model provided the highest prediction accuracy for all six hand gestures with an overall mean accuracy across 5000 randomly selected training data of 97.29 ± 1.11% based on real-time experimental results collected from a human participant (**Fig. 2.3D–E**). The next best model was the random forest classifier, which was found to have a similar average classification accuracy except with a higher variance. The KNN model was able to provide high-accuracy recognition of gestures with different angles when applying the e-skin-H to other body parts such as the neck, lower limb, and upper back—each time achieving an accuracy of greater than 90%.

For each gesture, five features were extracted from the associated peak in the root mean square (RMS)–filtered sEMG data: peak height (PH), peak standard deviation (STD), maximum slope (MS), peak average (PA), and peak energy (PE). The relevance of each feature and channel in the prediction method was further evaluated using Shapley additive explanation (SHAP) values[23]. Through

the SHAP values and the KNN accuracy, it was determined that PH was the most important feature for accurate gesture classification (**Fig. 2.3F**). When considered alongside PH, SD and PA both increased the classification accuracy, with SD being the most beneficial. In terms of channels, it was found that three EMG channels were sufficient to provide a high gesture accuracy of 96.31 ± 1.25%. Adding a fourth channel was beneficial but not statistically significant.

With the KNN algorithm, the robot can imitate the user's gesture in millisecond-level time for automatic object manipulation. The data acquisition and signal processing time delay to determine a gesture were around 200 ms, well below the required time for optimal real-time robotic control[24]. This was achieved using a sampling rate of 534 Hz and analyzing the data in batches of 100 points. The M-Bot's time delay was substantially reduced by training the KNN model on only half of any sEMG signal for gesture recognition. By reducing the required data needed to determine a gesture, the machine learning model was able to predict the movement almost immediately after the gesture was complete.

The AI-powered e-skin-H–enabled gesture recognition provides a framework for online multidirectional robotic control with high-accuracy remote object manipulation (**Fig. 2.3G–I**). After object contact, recognition, and positive threat detection, tactile and alarm feedback can be activated to inform the user of any potential danger using a pulsed current load between the two stimulation electrodes (**Fig. 2.3J**). To facilitate safe robotic handling and to protect e-skin-R

from uncontrolled collisions, a laser proximity sensor was integrated into the robotic hand to reduce the actuation speed as the hand approaches a barrier (<10 cm) (**Fig. 2.3K**).

2.2.4 Evaluation of human-interactive robotic physicochemical sensing

With delicate and precise control, the human-machine interactive M-Bot was successfully evaluated for fingertip point-of-use robotic TNT detection. The multimodal sensor data could be captured in real time using a portable multichannel potentiostat, wirelessly transmitted to the mobile phone, and displayed on the cellphone app. The M-Bot was also able to perform object grasping and multispot tactile and chemical sensing (**Fig. 2.4A–D**). Multiplexed physicochemical data were simultaneously recorded and automatically processed without signal interferences. In an example demonstration, seven AI-assisted gesture-controlled steps were used in sequence to control the robotic hand as it approached, grasped, and released a spherical object (**Fig. 2.4E**). In parallel, five sensor arrays were activated, displaying multiplexed tactile readings and surface TNT levels (**Fig. 2.4F–G**).

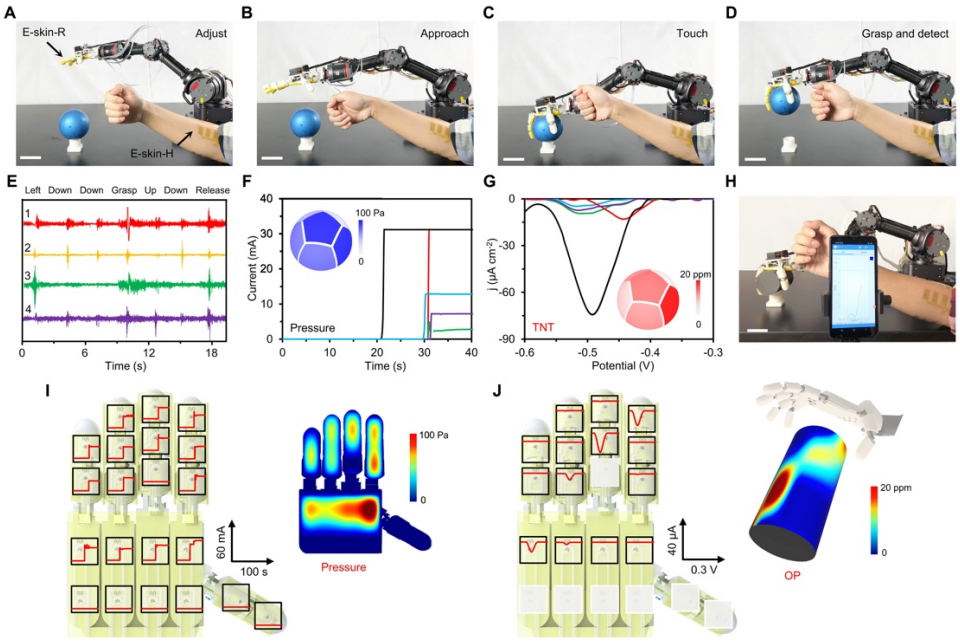

Figure 2.4. Evaluation of the M-Bot in human-interactive robotic physicochemical sensing. (A to D) Time-lapse images of the human-interactive robotic control for object grasping and on-site TNT detection. Scale bars, 5 cm. (E to G) The sEMG data collected in real time, which allow the robotic hand to approach and grasp a spherical object (E) and the corresponding tactile (F) and TNT (G) sensor responses. Insets in (F) and (G) represent the colored mapping of pressure and TNT distributions on the object. (H to J) Photograph of the robotic OP sensing on a cylindrical object (H) and the corresponding responses of the tactile sensors (I) and OP sensors (J) on an e-skin-R. Insets in (I) and (J) represent the color mappings of pressure and OP distributions on the object. Scale bar, 5 cm.

The use of the M-Bot for multiplexed physicochemical robotic sensing was further evaluated on an OP-contaminated cylindrical surface (**Fig. 2.4H**). During the experiment, 14 sensor arrays on e-skin-R were activated. The tactile and OP sensor responses from each sensor, along with the corresponding color mapping of their distributions across the three-dimensional (3D) surface (**Fig 2.4I–J**). We

anticipate that by further increasing the number and density of the multimodal sensor arrays, more accurate and informative data can be obtained from arbitrary objects and surfaces.

2.2.5 Assessment of electronic skin-based autonomous source tracking

The multimodal robotic sensing platform was further generalized onto an autonomous robotic boat capable of tracking pollutants, explosives, chemical threats, and biological hazards for risk prevention and mitigation, which is an important topic in civil security. In this regard, our printed multimodal e-skin-R technology was adapted onto a multimodal sensing robotic boat (M-Boat) for real-time hazard detection and to autonomously locate the source of water-based chemical leakages (**Fig. 2.5A**). 3D printed from simple computer-aided designs, the M-Boat contains an inkjet-printed multimodal sensor array with one temperature and three chemical sensors, two electrical motors (for boat propulsion and steering), and a printed circuit board (PCB) for data collection, signal processing, and motor control (**Fig. 2.5B–D**). The propulsion of the M-Boat can be precisely controlled by adjusting the individual duty cycle of pulsed voltages supplied to each motor (**Fig. 2.5E**). For source detection, an A* search algorithm was implemented for autonomous decision-making while searching for the maximum concentration of the chemical leakage (**Fig. 2.5F–G**). At each decision point, the sensors can detect small traces of the chemical leak in three equidistant locations around the boat. With this input, the algorithm calculates the optimal direction to travel using the gradient vector, indicating the direction of the highest concentration, and a heuristic estimate of the diffusion based on an

interpolated map from previous points. By using the heuristic map in parallel with the gradient, the algorithm takes advantage of both the past and present results to precisely predict the spatial location of the source. The performance of the M-Boat was evaluated through simulations and experimentally in water tanks containing various chemical gradients induced by a low pH-corrosive fluid (**Fig. 2.5H–I**) and OP leakage (**Fig. 2.5J–K**). In the water tank, the M-Boat performed real-time detection of the surrounding analyte concentrations, automatically adjusting its trajectory based on the A* algorithm, to successfully identify the leakage source. The M-Boat was also able to perform continuous hazard analysis and autonomous leakage tracking in seawater. The surrounding pH and ionic strength of a real-world sample matrix (e.g., lake water or seawater) did not show substantial influence on the sensor performance. When necessary, more real-time calibration mechanisms for precise hazard analysis can be introduced by incorporating more related biosensors (e.g., pH and conductivity sensors) into the e-skin-R. With more advanced robotic control and sensing designs, the M-Boat platform could serve as an important basis for intelligent path planning and decision-making of autonomous vehicles.

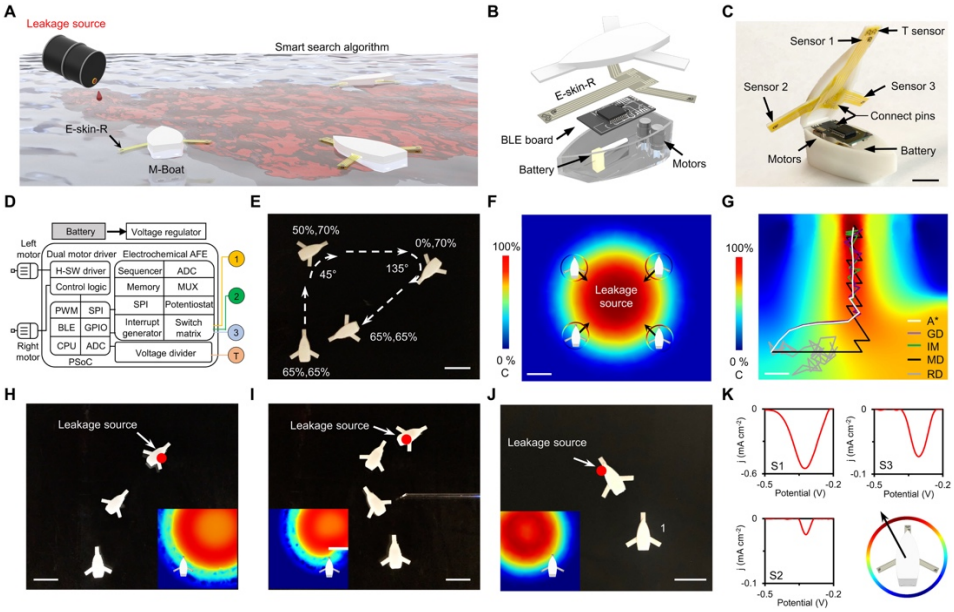

Figure 2.5. Evaluation of an electronic skin-based autonomous boat. (A) Schematic of the intelligent M-Boat integrated with a printed multimodal e-skin-R sensor array that can perform temperature and multiplexed chemical sensing for autonomous source tracking. (B and C) Schematic (B) and photograph (C) illustrating the assembly of the M-Boat components. (D) System block diagram of the M-Boat for autonomous propulsion, sensing, and signal processing. AFE, analog front end; CPU, central processing unit; H-SW, H-bridge software; MUX, multiplexer. (E) Wireless control of the M-Boat. (F) Simulated distributions of a hazardous chemical (OP) leak and the algorithm used by the M-Boat for autonomous source tracking. C, concentration. (G) Simulation comparison of different search algorithms used by the M-Boat for intelligent source tracking. GD, gradient descent; IM, interpolated map; MD, max direction; RD, random direction. (H and I) Time-lapse images showing example demonstrations of the M-Boat–enabled autonomous source tracking. Insets: Simulated target (proton from corrosive acid) distributions. Scale bars, 5 cm. (J and K) Time-lapse images (J) and the nDPV voltammograms collected at location 1 (K) for autonomous decision-making and chemical threat (OP) source tracking using an M-Boat. Insets: Simulated OP distribution. Scale bar, 5 cm.

2.3 Methods

2.3.1 Development of the multimodal sensing robot

The e-skin-R–interfaced 3D printed robotic hand was assembled onto a five-axis robotic arm (Innfos Ltd.). Afterwards, the e-skin-H was then set around a human participant's forearm after cleaning the skin with alcohol swabs. The sEMG data were acquired with four channels (three sEMG electrodes in each channel) through an open-source hardware shield (Olimex). The signals were sampled as integers between 0 and 1023 by a 10-bit analog-to-digital converter (ADC) and then processed through a serial (cluster communication) port. Each channel was then scaled back into voltages between 0 and 5 V. Although the robotic arm control was performed in real time, data processing was performed asynchronously to signal acquisition. During processing, the data were first put through a high-pass filter with a cutoff frequency of 100 Hz. The points were subsequently downsized using an RMS filter (batch size: 400 points and step size: 10 points). The peaks detected after processing were used as features for the machine learning model. Overlapping peaks from each channel (peaks within a half-peak width away) were categorized as a single group. If multiple peaks were detected in a single channel's set, then the first peak was used. The KNN training model was built using 60 samples per each of the six gestures. The training and testing datasets were divided 2:1, respectively, and were randomly selected using an equal representation of each gesture. After the model was developed, it was further evaluated for accuracy using new data from each gesture. The laser proximity sensor (LPS) (TOF10120) was operated through a customized

interactive control software in Python (Python 3.8). For dry blot threat detection, TNT and OP threat coatings were created by spraying analyte vapor onto the selected objects in a fume hood. Multimodal sensing data collected during robotic sensing operations were collected through a portable electrochemical workstation (PalmSens4) with a multiplexer.

The validation and evaluation of the M-Bot were performed using human participants in compliance with all the ethical regulations under protocols (ID 19-0895) that were approved by the Institutional Review Board at the California Institute of Technology. Three participates were recruited from the California Institute of Technology's campus and the neighboring communities through advertisement. All participants gave written informed consent before study participation.

2.3.2 Data analysis and machine learning pipeline

For each gesture, all five features were extracted from the associated peak in the RMS-filtered EMG data: height, average area, SD, average energy (intensity), and maximum slope. The features extracted were calculated in reference against their baselines, which were determined via a binary search of the previous data in 50-ms intervals.

After feature extraction, SHAP values were used to evaluate the performance enhancement of each feature extracted and EMG channel used. In addition to SHAP values, the average testing accuracy across 5000 training sessions was

taken for each permutation of features and EMG channels, which supplemented the SHAP values in providing further insight into which channels and features contained nonoverlapping beneficial information for gesture determination. For each of the 5000 trials, the testing points represented 33% of the dataset, with each gesture in the test set being proportionally represented in the full dataset. For the arm EMG dataset, this amounted to 387 movements split across six gestures; of those points, the KNN model was fit using 257 training points and scored on the remaining 128 testing points (testing and training were proportionally stratified across all six gestures).

2.3.3 Development of the autonomous sensing boat

To evaluate the performance of the M-Boat, the e-skin-R was assembled onto a 3D printed boat with a four-layer PCB. On the PCB, a Bluetooth low-energy (BLE) module (CYBLE-222014-01, Cypress Semiconductor) was used for controlling the electrochemical front end through a serial peripheral interface (SPI). This module was also used to control the motor driver through general purpose input/output (GPIO) pins and pulse width modulation (PWM) and to transmit data over BLE. An electrochemical front end (AD5941, Analog Devices) was set up via SPI to perform multiplexed electrochemical measurements with the sensor arrays and to send the acquired data to the BLE module for signal processing and BLE transmission. A BLE dongle (CY5677, Cypress Semiconductor) was used to establish a BLE connection with the M-Boat and to securely receive the sensor data via BLE indications. An A*

algorithm was used to analyze the sensor data and compute the next M-Boat's movement path with the optimal motor speed. The calculated motor speed information was sent back to the BLE module in real time for the pulse width–modulated control of two motors (Q4SL2BQ280001) through a dual dc motor driver (TB6612FNG, Toshiba). The entire system was powered by a 3.7-V Li-ion battery (40 mAh).

For the OP chemical threat tracking experiment, a natural diffusion gradient was generated by 10 droppings of 20 μl of 0.1 M OP into a 0.1 M NaCl solution tank. The seawater studies were performed in seawater samples collected from the Pacific Ocean in Los Angeles. The M-Boat was set into the tank after 30 min. For the corrosive acidic threat tracking experiment, pH sensors were modified on e-skin-R instead. Briefly, a polyaniline pH-sensitive film was electropolymerized on the IPCE in a solution containing 0.1 M aniline and 0.1 M HCl using a CV from −0.2 to 1 V for 25 cycles at a scan rate of 50 mV s−1. Then, 100 μl of H2SO4 (2 M) as the leakage source was dropped into the middle of the water tank. Last, the M-Boat was set after 45/30 min with/without barriers in the tank, respectively.

2.4 Materials

Graphite flake was purchased from Alfa Aesar. Sodium nitrate, potassium permanganate, hydrogen peroxide, potassium hexacyanoferrate(III), citric acid, chloroplatinic acid, PDMS, zirconium(IV) chloride, aniline, gelatin, paraoxon-

methyl, TNT solution, 4-nitrophenol, 2-nitrophenyl octyl ether, 2-nitroethanol, 2-nitropropane, 4-nitrotoluene, 2,4-dinitrotoluene, poly(pyromellitic dianhydride-co-4,4′-oxydianiline) amic acid (PAA) solution [12.8 weight % (wt %)], 1-methyl-2-pyrrolidinone (NMP), N-hydroxysulfosuccinimide sodium salt (Sulfo-NHS), N-(3-dimethylaminopropyl)-N′-ethyl carbodiimide hydrochloride (EDC), 2-(N-morpholino)ethanesulfonic acid hydrate (MES), potassium permanganate (KMnO4), bovine serum albumin (BSA), human immunoglobulin G (IgG), and lysozyme were purchased from Sigma-Aldrich. Sodium chloride, sulfuric acid, hydrochloric acid, disodium phosphate, 1,3,5-benzenetricarboxylic acid (H3BTC), formic acid, N,N′-dimethylformamide (DMF), potassium ferricyanide, propylene glycol, isopropyl alcohol (IPA), and phosphate-buffered saline (PBS) were purchased from Thermo Fisher Scientific. His-tagged SARS-CoV-2 S1 (PNA002), anti–Spike-RBD human monoclonal antibody (IgG) (S1-IgG, AHA013), SARS-CoV S1 (40150-V08B1), SARS-CoV nucleocapsid protein (NP; 40143-V08B), and SARS-CoV-2 NP (40588-V08B) were purchased from Sanyou Biopharmaceuticals. AgNW suspension (20 mg ml−1 in IPA) was purchased from ACS Material LLC. Silver ink (25 wt %) and carbon ink (5 wt %) were purchased from NovaCentrix. Gold ink (10 wt %) was purchased from C-INK Co. Ltd. Carboxyl-functionalized multiwalled CNT ink (2 mg ml−1; Nink-1000) was purchased from NanoLab Inc. PI film (12.5 μm) was purchased from DuPont.

2.4.1 Preparation and characterizations of printed inks

To prepare the Pt-graphene ink, GO was first prepared following a modified Hummer's method. One gram of graphite flake was mixed with 23 ml of H_2SO_4 for more than 24 hours, and then 100 mg of $NaNO_3$ was added inside. Subsequently, 3 g of $KMnO_4$ was added below 5°C in an ice bath. After stirring at 40°C for another 30 min, 46 ml of H_2O was added while the solution temperature was slowly increased to 80°C. In the end, 140 ml of H_2O and 10 ml of H_2O_2 were introduced into the mixture to complete the reaction. The GO was washed with 1 M HCl and filtered. After dried under vacuum at 60°C, a GO (2 mg ml−1) suspension was prepared followed by the addition of 5 mM chloroplatinic acid under sonication. Last, the suspension was mixed with propylene glycol (80:20, v/v) to form the Pt-graphene ink.

The MOF-808 was synthesized solvothermally. Briefly, H_3BTC (0.236 mM) and $ZrCl_4$ (1 mM) were mixed with 15.6 ml of the DMF and formic acid (1:0.56, v/v) solvent and sonicated for 20 min. Then, the mixture was transferred to a 25-ml Teflon-lined autoclave and kept at 120°C for 12 hours. After the reaction, the autoclave was naturally cooled to room temperature. The product was washed with DMF and methanol and then dried under vacuum at 60°C. Last, a MOF-808 suspension in deionized (DI) water was prepared and mixed with propylene glycol (80:20, v/v) to form the MOF-808 ink.

The AgNWs ink was prepared by diluting the AgNW suspension with IPA to 2 mg ml−1 and sonicating it for 10 min. The CNT ink was prepared by mixing the commercial CNT ink (2 mg ml−1) with propylene glycol (80:20, v/v). PAA ink was prepared by diluting the commercial PAA solution with NMP to 3 wt %. Commercial silver and carbon inks were used as received.

The dynamic viscosity (η), density (ρ), and surface tension (γ) for all inks were characterized before printing. Dynamic viscosity was characterized with an Anton Paar MCR302 rheometer. Surface tension was measured with a Ramé-Hart contact angle goniometer.

2.4.2 Fabrication and assembly of the soft inkjet-printed e-skin-R

The fabrication process of the inkjet-printed e-skin-R is illustrated in fig. S1. The PI substrate was cut with kirigami structures by automatic precision cutting (Silhouette Cameo 3). A 2-min O2 plasma surface treatment was performed with Plasma Etch PE-25 (10 to 20 cm3 min−1 O2, 100 W, 150 to 200 mtorr) to enhance the surface hydrophilicity of the PI substrate. The multimodal sensor arrays on e-skin-R were fabricated via serial printing of silver (interconnects and reference electrode), carbon (counter electrode and temperature sensor), PI (encapsulation), and target-selective nanoengineered sensing layers (e.g., AgNWs, Pt-graphene, Au, and MOF-808) using an inkjet printer (DMP-2850, Fujifilm). The ink composition, characterizations, and thermal annealing conditions are shown in table S1. Thirty layers of AgNWs were printed on an N-

PDMS substrate (cured on a 1000-mesh sandpaper) to form the piezoresistive tactile sensors. While printing, the plate temperature was set to 40°C to ensure the rapid vaporization of the IPA solvent. The AgNWs/N-PDMS were cut to semicircle shape and set on the e-skin.

For preparing biohazard S1 protein sensor (fig. S17), a CNT film was printed on the IPCE first. The carboxylic groups of multiwall CNTs were activated to NHS esters, by drop-casting 10 μl of EDC (400 mM) and NHS (100 mM) in MES buffer (25 mM, pH 5) for 35 min. In the next step, 5 μl of anti–Spike-RBD antibody (250 μg ml−1) in PBS were dropped on the modified electrode and incubated for 2 hours. Next, 10 μl of 1% BSA in PBS were dropped and incubated for 1 hour to deactivate residual NHS esters. The modified sensors were stored in the refrigerator until use.

To assemble the robotic e-skin, the pins of the finger-printed e-skin were connected with the bottom printed silver connections of palm part through a z axis conductive tape (3M), and then e-skin-R was set on a robotic hand printed with a 3D printer (Mars Pro, Elegoo Inc.).

2.4.3 Characterizations of the multimodal robotic sensing performance

The printed biosensors were characterized with cyclic voltammetry (scan rate: 50 mV s−1, unless otherwise noted), DPV, and amperometric current (i)-time (t) through an electrochemical workstation (CHI 660E). McIlvaine buffer solutions (pH 6.0) were used to prepare the analyte solutions. A commercial Ag/AgCl

reference electrode (CHI111) was used for characterizing the printed sensing electrodes in the solution, whereas printed Ag solid-state electrodes were used for hydrogel-based sensor characterization (there was an ~0.1-V difference between these two types of reference electrodes in McIlvaine buffer). To quantify the electrochemical performance and the electrochemical surface areas, the print electrodes were tested in 5 mM K3Fe(CN)6 and 1 M KCl with scan rates of 5 mV s−1 from −0.1 to 0.5 V.

For TNT and OP sensors, the conditions of nDPV measurements include a scan range of −0.15 to −0.5 V, an incremental potential of 0.004 V, a pulse amplitude of 0.05 V, a pulse width of 0.05 s, and a pulse period of 0.5 s. The reduction peaks of nDPV curves were extracted using a custom-developed iterative baseline correction algorithm. To prepare the electrolyte-loaded hydrogel for analyte sampling and sensing, 0.250 g of gelatin powder, 0.075 g of KCl, 0.071 g of citric acid, and 0.179 g of disodium phosphate were mixed in 10 ml of DI water and stirred at 80°C for 15 min. The hydrogel was stored and aged overnight. The gelatin electrolyte-loaded hydrogel was coated on the printed biosensors for dry blot detection.

For S1 protein detection, the modified electrode was incubated with 10 µl of S1 protein in PBS for 10 min, and the DPV measurements ranged from −0.1 to 0.5 V. The electrochemical signal of the sensor before and after antigen binding was measured in 5 mM K3Fe(CN)6. The difference between the peak current

densities (Δj) was obtained as sensor readout. A sampling hydrogel pad was prepared to demonstrate the feasibility for SAR-CoV-2 virus dry blot detection. To perform one-step detection, 10 μl of gelatin hydrogel [7.5 wt % gelatin, 10 mM K3Fe(CN)6, and 0.2 M phosphate buffer (pH 7.0)] was placed onto a dry S1 protein blot [from 10 μl of a SARS-CoV-2 S1 protein droplet (1 μg ml−1)]. Such amount of S1 protein could potentially be found in the saliva droplet of a patient with COVID-19. For dry-phase sensing selectivity study, the dry protein blots were created with the same amount of interference proteins (10 μl, 1 μg ml−1). The electrochemical signal of the gel was recorded immediately and 10 min after joining the biosensor with the gel.

The temperature sensor characterization was performed on a ceramic hot plate (Thermo Fisher Scientific), and an amperometric method (with an applied voltage of 2 V) was used to detect the temperature response. The piezoresistive tactile sensor characterization was also applied with a constant voltage of 2 V to record the current response under various pressure loads.

The scanning electron microscopy (SEM) images of the electrodes were obtained by a field-emission SEM (FEI Nova 600 NanoLab). Energy-dispersive spectroscopy (EDS) mapping were obtained by an EDS spectrometer (Bruker Quantax EDS).

2.4.4 Fabrication and assembly of e-skin-H

The fabrication process of e-skin-H was illustrated in fig. S26. A 2-min O2 plasma surface treatment was performed with Plasma Etch PE-25 to enhance the surface hydrophilicity of the PI substrate. Silver interconnects were printed with DMP-2850. The PI substrate without the printed patterns were removed with laser cut using a 50-W CO2 laser cutter (Universal Laser Systems). The optimized laser cutter parameters were power of 10%, speed of 80%, and pixels per inch (PPI) of 1000 in vector mode. After cleaned with ethanol and dried, the remaining patterns were transferred onto a 70-μm-thick PDMS substrate and then encapsulated with another layer of PDMS film as well (with sEMG and electrical stimulation electrodes exposed). An adhesive electrode gel (Parker Laboratories Inc.) was spread onto the electrodes before placing on human participants.

2.5 Discussion

Here, we have described a human-machine interactive e-skin–based robotic system with multimodal physicochemical sensing capabilities. The mass-producible flexible sensor arrays allow for high-performance on-site monitoring of temperature, tactile pressure, and various hazardous chemicals (in both dry phase and liquid phase) such as explosives, OPs, and pathogenic proteins. The integration of such multimodal sensors onto a robotic e-skin platform provides autonomous systems with interactive cognitive capabilities and substantially broadens the range of tasks that robots can perform, such as combating infectious diseases like COVID-19.

Existing robotic sensing technologies are largely limited to monitoring physical parameters such as temperature and pressure. To achieve high-performance chemical sensing, nanomaterials are commonly used via manual drop-casting methods, which could lead to large sensor variations. Moreover, most electrochemical sensing strategies require detection in aqueous solutions, making them impractical for dry-phase robotic analysis. Now, there are no reported scalable low-cost manufacturing approaches to prepare robotic physicochemical sensors. In this work, we proposed a scale solution to fabricate flexible, multifunctional, and multimodal sensor arrays prepared entirely by high-speed inkjet printing. Custom-developed functional nanomaterial inks are designed and optimized to achieve highly sensitive and selective sensors for the specific hazardous target analytes. The hydrogel-coated printed nano-biosensors allow for efficient dry-phase chemical sampling and rapid on-site hazard analysis on a robotic platform.

Manufactured using the same approach, e-skin-H ensured stable contact with the soft human skin for reliable recording of neuromuscular activity to facilitate remote robotic sensing and control. To minimize the amount of data collected and analyzed for human-robotic interaction, AI and smart algorithms were applied to decode incoming information and efficiently predict and control robotic movement. An in-depth analysis into each sEMG channel's individual contribution to the machine learning model was presented, allowing future researchers to optimize the number of electrodes needed for robotic control. Using the SHAP analysis, we further untangled the hidden overlapping

information between each channel's features and categorized which features present the most nonoverlapping information for gesture prediction. For the M-Bot, machine learning gesture prediction via e-skin-H was further coupled with user-interactive tactile and threat alarm feedback that allow seamless human-machine interaction for the remote deployment of robotic technology in extreme or contaminated environments. To obtain such real-time results, the robotic platform's data acquisition, signal processing, feature extraction, and gesture prediction of the sEMG signals were performed with millisecond-level time after the gesture was complete. The M-Boat similarly used a smart A* algorithm for autonomous source detection, minimizing the boat's path, and subsequently, time and energy, in finding potentially hazardous chemical leaks. In these applications, the systems demonstrated real-time autonomous movement, all within a low-cost mass-producible system, lowering the barrier for real-time robotic perception.

This human-machine–interactive robotic sensing technology represents an attractive approach to develop advanced flexible and soft e-skins that can reliably collect vital data from the human body and the surrounding environments. Full system integration to achieve high-speed, wireless, and simultaneous multichannel physicochemical sensing is strongly desired for future field deployment and evaluation. Moreover, we envision that, by integrating a high density and new types of multimodal sensors, this technology could substantially enhance the perceptual capabilities of future intelligent robots and pave the way to numerous new practical wearable and robotic applications.

2.6 Conclusion

Human–Machine Interfaces (HMIs) have progressed beyond bulky, rigid, task-specific systems to become ultrathin, skin-integrated platforms capable of providing continuous physiological monitoring and adaptive, personalized feedback. These advanced systems utilize soft, biocompatible materials combined with multimodal sensing capabilities to facilitate seamless, real-time communication between the human body and intelligent machines. Integrating tactile and physicochemical sensors into autonomous systems has enabled artificial platforms to replicate and surpass human perceptual abilities. This has enabled downstream applications for remote threat detection, safe navigation in hazardous environments, and task execution without exposing users to physical or chemical dangers. Technologies such as printed electronic skins with flexible sensor arrays have demonstrated scalable, cost-effective fabrication methods, providing a versatile approach for developing new wearable platforms. This chapter introduced an ultrasensitive, multimodal physicochemical sensing platform designed for autonomous robotic decision-making, with applications spanning agriculture, security, environmental protection, and public health. Furthermore, this fully printed, human–machine interactive sensing technology can be reconfigured for various practical wearable and robotic applications aimed at enhancing general well-being.

References

1. Yang, G.-Z. *et al.* The grand challenges of Science Robotics. *Sci Robot* **3**, eaar7650 (2018).
2. Cianchetti, M., Laschi, C., Menciassi, A. & Dario, P. Biomedical applications of soft robotics. *Nat. Rev. Mater.* **3**, 143–153 (2018).
3. Chortos, A., Liu, J. & Bao, Z. Pursuing prosthetic electronic skin. *Nat Mater* **15**, 937–950 (2016).
4. Yin, J., Hinchet, R., Shea, H. & Majidi, C. Wearable Soft Technologies for Haptic Sensing and Feedback. *Adv. Funct. Mater.* **31**, 2007428 (2021).
5. Boutry, C. M. *et al.* A hierarchically patterned, bioinspired e-skin able to detect the direction of applied pressure for robotics. *Sci Robot* **3**, eaau6914 (2018).
6. Ishida, H., Wada, Y. & Matsukura, H. Chemical Sensing in Robotic Applications: A Review. *IEEE Sens. J.* **12**, 3163–3173 (2012).
7. Wang, J. Electrochemical sensing of explosives. *Electroanalysis* **19**, 415–423 (2007).
8. Singh, S. Sensors - An effective approach for the detection of explosives. *J. Hazard. Mater.* **144**, 15–28 (2007).
9. Fainberg, A. Explosives detection for aviation security. *Science* **255**, 1531–1537 (1992).
10. Vucinic, S. *et al.* Environmental exposure to organophosphorus nerve agents. *Environ Toxicol Pharmacol* **56**, 163–171 (2017).
11. Bajgar, J. Organophosphates/nerve agent poisoning: mechanism of action, diagnosis, prophylaxis, and treatment. *Adv Clin Chem* **38**, 151–216 (2004).
12. Gao, A. *et al.* Progress in robotics for combating infectious diseases. *Sci Robot* **6**, eabf1462 (2021).
13. Shen, Y. *et al.* Robots Under COVID-19 Pandemic: A Comprehensive Survey. *IEEE Access* **9**, 1590–1615 (2021).
14. Yang, G.-Z. *et al.* Combating COVID-19-The role of robotics in managing public health and infectious diseases. *Sci Robot* **5**, eabb5589 (2020).
15. Gao, W. *et al.* Fully integrated wearable sensor arrays for multiplexed in situ perspiration analysis. *Nature* **529**, 509–514 (2016).
16. Ray, T. R. *et al.* Bio-Integrated Wearable Systems: A Comprehensive Review. *Chem Rev* **119**, 5461–5533 (2019).
17. Kim, D.-H. *et al.* Epidermal Electronics.
18. Shih, B. *et al.* Electronic skins and machine learning for intelligent soft robots. *Sci Robot* **5**, eaaz9239 (2020).
19. Kim, J., Campbell, A. S., de Ávila, B. E.-F. & Wang, J. Wearable biosensors for healthcare monitoring. *Nat Biotechnol* **37**, 389–406 (2019).
20. Amit, M. *et al.* Point-of-use robotic sensors for simultaneous pressure detection and chemical analysis. *Mater. Horizons* **6**, 604–611 (2019).
21. Troya, D. Reaction Mechanism of Nerve-Agent Decomposition with Zr-Based Metal Organic Frameworks. *J. Phys. Chem. C* **120**, 29312–29323 (2016).

22. de Koning, M. C., van Grol, M. & Breijaert, T. Degradation of Paraoxon and the Chemical Warfare Agents VX, Tabun, and Soman by the Metal-Organic Frameworks UiO-66-NH2, MOF-808, NU-1000, and PCN-777. *Inorg Chem* **56**, 11804–11809 (2017).
23. Lundberg, S. M. & Lee, S.-I. A Unified Approach to Interpreting Model Predictions. in *Advances in Neural Information Processing Systems* vol. 30 (Curran Associates, Inc., 2017).
24. Hudgins, B., Parker, P. & Scott, R. N. A new strategy for multifunction myoelectric control. *IEEE Trans Biomed Eng* **40**, 82–94 (1993).

Chapter 3

WEARABLE BIOSIGNAL ANALYSIS

Materials from this chapter appear in "Heng, W.; Solomon, S. A.; Gao, W. Flexible Electronics and Devices as Human–Machine Interfaces for Medical Robotics. Adv. Mater. 2022, 34, 2107902. https://doi.org/10.1002/adma.202107902." and "Min, J.; Tu, J.; Xu, C.; Lukas, H.; Shin, S.; Yang, Y.; Solomon, S.; Mukasa, D.; Gao, W. Skin-interfaced wearable sweat sensors for precision medicine. *Chemical Reviews* 123 (8), 5049-5138 (2023). https://doi.org/10.1021/acs.chemrev.2c00823."

Wearable sensors hold significant promise for enabling continuous health monitoring, predictive analytics, and timely intervention in support of personalized healthcare. As outlined in the previous chapter on Human–Machine Interfaces, advances in flexible electronics, material science, and scalable fabrication have accelerated the development of skin-conformal platforms capable of noninvasively capturing physiological signals relevant to human health. However, extracting clinically meaningful biometric information that enables real time actionable insights remains a major challenge. Learning temporal patterns across individualized biometric profiles requires robust data analytic strategies capable of handling noisy, high-dimensional, and fragmented inputs. This chapter highlights the computational challenges associated with transmitting, processing, and modeling wearable biomarkers—including the construction of low-dimensional representations, the mitigation of data scarcity, and the development of learning architectures that generalize across populations, contexts, and sensor configurations.

3.1 Data transmission and signal latency

Wearable data analysis pipelines must quickly decode, recognize, and respond to user sensations with minimal temporal latency. In abled-bodied patients, the latency period for tactile sensations to reach the cuneate nucleus is around 14–28 ms, where any delay beyond 300 ms will result in a user-perceived lag (**Fig. 3.1A**)[1,2]. Unfortunately, this poses a problem for multimodal ultrathin wearable platforms, where hardware constraints limit the amount of data that can be

processed simultaneously, as processing a high density of signals in parallel can result in electrical interference and sensor crosstalk. Transistor switches can minimize the magnetic overlap by sending signals asynchronously, but this adds an additional lag before data processing, health predictions, and mechanical interventions. Further research into quickly processing and transmitting data without electrical interference nor added electronic connections can help maximize the amount of data that medical robots can extract and process from their environment (**Fig. 3.1B–C**)[3].

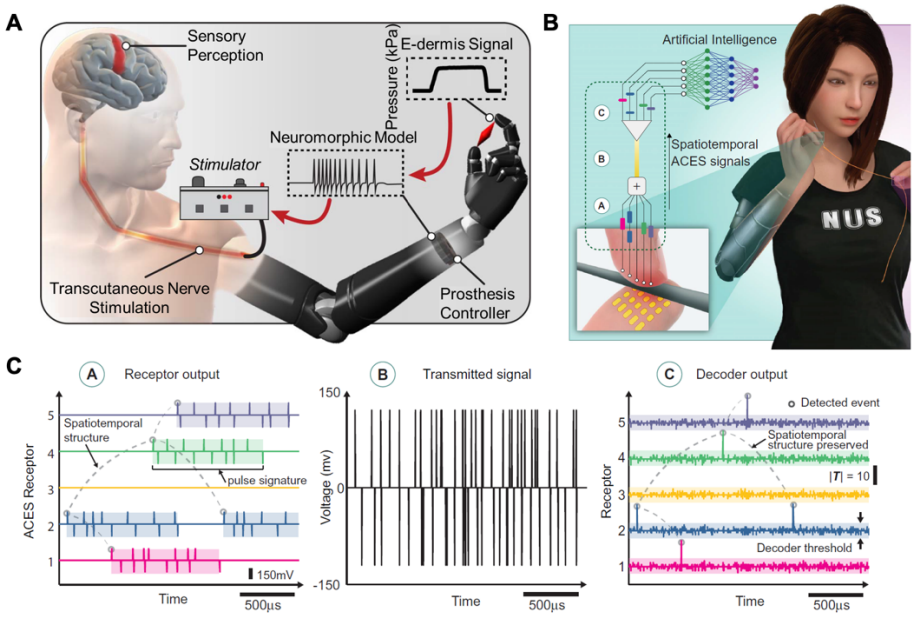

Figure 3.6 Data transmission within human machine interfaces. A) A neuromorphic interface producing receptor-like spiking neural activity for tactile stimuli feedback. Reproduced with permission. Copyright 2018, AAAS. B) Illustration of artificial receptors asynchronously transducing tactile events into pulse signatures. Reproduced with permission. Copyright 2019, AAAS. C) Artificial receptors generate tactile events with spatiotemporal structures (dashed

lines) that encode the stimulation sequence. Reproduced with permission. Copyright 2019, AAAS.

Beyond the latency challenges inherent within biosignal processing, most modern mechanical systems are further constrained by the von Neumann architecture—a computing model that physically separates memory from the central processing unit (CPU). This separation introduces a critical bottleneck, where only a limited bandwidth is available for data transfer between the memory and processor, meaning that each time the CPU retrieves or stores data, execution must pause until memory access is complete[4]. This interruption, known as the von Neumann bottleneck, results in a significant idle time during program execution and becomes increasingly problematic in real-time data processing environments such as wearable health systems. To mitigate this bottleneck, researchers have historically pursued improvements in the bandwidth by increasing transistor density, following Moore's Law. However, as chip architectures approach processing nodes smaller than 2–3 nanometers, continued miniaturization is increasingly hindered by physical limitations such as heat dissipation and quantum effects. As progress in traditional architectures slows, alternative approaches must be explored. One such approach is the parallelization of data access, inspired by the brain's ability to simultaneously transmit information through large networks of neurons. This neuromorphic paradigm enables multiple data streams to be processed concurrently, circumventing the serial limitations of von Neumann designs[5].

Recent research has focused on the development of non–von Neumann computing architectures using artificial intelligence, with particular interest in spiking neural networks (SNNs). In SNNs, information is encoded in discrete voltage spikes, and data transfer occurs only when a node surpasses a defined threshold—enabling asynchronous, event-driven computation across multiple nodes in parallel. SNNs have shown promise in dynamic neuromorphic asynchronous processors, offering minimal time delays and superior data throughput compared to conventional architectures. Their biologically inspired design holds potential for accelerating real-time processing in embedded AI applications, including wearable systems. As machine learning continues to influence computing architecture, further research into neuromorphic models may fundamentally reshape how information is accessed and transmitted—unlocking new levels of speed, efficiency, and scalability in biomedical computing.

3.3 Data privacy

A customer's perception of their data security during collection, transmission, and subsequent processing plays a critical role in their decision to adopt wearable technologies[29]. While the medical value of wearables is widely accepted, the associated privacy risk factors are a subject of concern and speculation. There is inherent danger in collecting and sharing health information with companies, between third parties, and with medical staff. For example, in 2021, major companies such as Fitbit (Google) and Apple were a part of a massive data breach

where 61 million customers' name, age, gender, geographic location, and health information were all exposed in an online database without any password protection. The problem with overseeing and managing data privacy concerns is that many wearable health trackers are not FDA approved medical devices and therefore are not required to follow strict medical privacy standards, allowing companies to provide minimal security guarantees as well as sell health data for marketing and advertising purposes. Moreover, once the health data is collected, there is no statute of limitation for companies to erase this information, regardless of whether the customer has terminated their internal profile. As the public's perceived risk of data privacy grows above their reported benefit, customers will discontinue use of wearable technologies[29]. Customer perception of their data privacy is therefore integral in their adoption of wearable devices and must be accounted for in wearable affective computing research.

3.3.1 Medical data security

There are two main entities that regulate the security of health information: the government and the device manufacturer. The United States Government secures the protection of medical data through the Health Insurance Portability and Accountability Act (HIPAA). HIPAA enumerates how to handle medical data through the Privacy Rule and the Security Rule, which applies to "business associates" dealing with "covered entities". In broad terms, covered entities are health plans, healthcare clearinghouses, and healthcare providers that transmit medical information electronically, while business associates use or disclose

protected health information for a covered entity. Under HIPAA protection, when sending medical information, companies must remove 18 key identifiers for security purposes, such as name, social security, health numbers, and medical records. Companies that violate these rules can be subjected to fines and criminal charges. However, companies can share private health data to third parties if the added entity agrees to protect the users' data according to HIPAA laws. This transfers the security grantees to potentially less trustworthy sources, where data breaches might not be reported back to the consumers.

Despite these restrictions, not all wearables adhere to HIPAA guidelines as their products are not considered medical devices but are rather classified as wellness tools. Even for FDA-approved medical devices such as Fitbit (FDA approval in 2020 for their ECG platform) and Apple watch (FDA approval in 2018 for their ECG platform and 2022 for atrial fibrillation), not all wearables have to adhere to HIPAA guidelines as their products do not electronically transfer sensitive information. For example, a wearable device such as a fitness tracker that monitors a user's health and displays that information on a smart watch does not need to be HIPAA compliant as the device does not share the data with a business associate or a covered entity, such as a physician. This provides an illusion of data security to the customer, while exposing individuals to a variety of attacks. It should be noted that the FDA is in the process of updating its guidelines for handling sensitive data and have already announced a new Office of Digital Transformation back in 2021.

Without government regulation, companies themselves can still adhere to strict data security and privacy standards. During data storage, companies can secure themselves against common hacks such as distributed denial of service (DDoS) attacks[30], Structured Query Language (SQL) injections, or back door attacks. Two common methods to secure data include authentication, such as a pin number to validate the customer, and encryption, such as storing data on a blockchain. Blockchain works through decentralized data sharing, where an immutable data table is validated for authenticity by all users on the chain, preventing hackers from easily altering the records[31]. If a hacker does want to permanently change health information on the chain, they would have to hack into every user who stores a copy of that block. While this protects data storage, attacks on wearable devices can still occur during real-time data transmission. Data transferred over WiFi, Bluetooth, or any near-field communication can be subjected to data leaks due to misconnections. Fortunately, there are a variety of different methods to protect data across the Internet of Things to identify and mitigate potential software attacks against wearable devices.

3.3 Machine learning model integration

Wearable devices have the potential to generate a large spectrum of medical data, that when handled properly, can provide real-time benefits across the physical and mental health space (**Fig. 3.2A**). This is achieved by recoding a continuous stream of biometric information across the body, with a large amount of overlapping comprehensive information that collectively paints a picture about

the health of a patient. Artificial intelligence (AI), specifically machine learning (ML), offers a way to organize this information in an interpretable or useful manner. In the literature, machine learning data analytic approaches have predicted the presence of diseases, mental disorders[6], emotional states[7], drug intake, and nutritional levels[8,9].

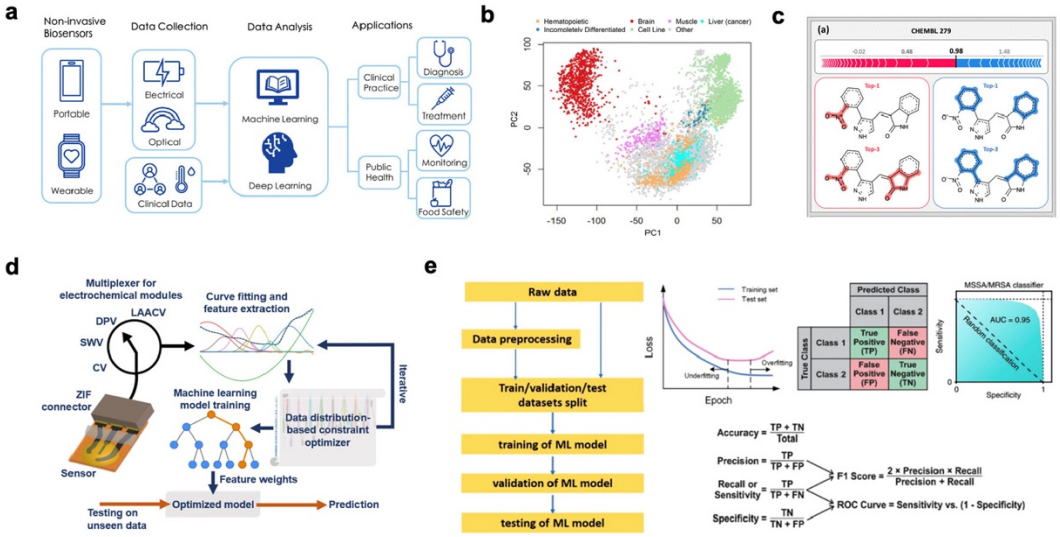

Figure 3.7 Data processing and machine learning. (A) Broad overview of the machine learning experimental pipeline from biosensor fabrication to industry application. Reproduced with permission. Copyright 2021 Wiley. (B) Principal component analysis (PCA) analysis that can categorize different cell lines based on gene expression. Reproduced with permission under CC BY 4.0. Copyright 2016 Lenz et al. (C) Shapley additive explanations (SHAP) analysis of two kinase inhibitors, displaying functional groups that help (red) or hurt (blue) its potency. Reproduced with permission under CC BY 4.0. Copyright 2020 Rodríguez-Pérez et al. (D) Flowchart for extracting features from electrochemical measurements, training a model, and predicting analyte concentrations. Reproduced with permission. Copyright 2022 Elsevier. (E) Generic training process for a neural network. Reproduced with permission. Copyright 2020 American Chemical Society.

When applying machine learning to wearable biosignals, there are three main general subcategories of algorithms: supervised learning, unsupervised learning, and reinforcement learning. Unsupervised and reinforcement learning can handle unlabeled data but require a large amount of experimental information before making predictions. In a research setting, this can be impractical as emerging wearable technologies are still being prototyped, without any feasible way to collected large high-quality datasets. Due to these limitations, we will focus on supervised learning algorithms for wearable data analysis, with the most common architectures being convolutional neural networks (CNNs), support vector machines (SVMs), k-nearest neighbors (KNNs), logistical regression, and artificial neural networks. Transformers are another common tool for wearable scientific computing, but they require a large amount of training data and have limited ability to model temporal patterns[10], which are characteristic of any wearable dataset.

3.3.1 Curse of dimensionality

From a data analytics perspective, features are quantifiable variables derived from raw data that serve as inputs to predictive models. In wearable systems, these may include biochemical analytes (e.g., uric acid) or physiological signals (e.g., heart rate variability) that correlate with health outcomes.

Despite a growing number of papers in biomarker discovery, extracting features does not always enhance prediction accuracies. While increased dimensionality

may initially enhance performance by enriching informational content, it also introduces additional degrees of freedom, raising the risk of overfitting. Model inputs interact with each other within a high-dimensional space, where the volume of data required to maintain statistical confidence grows exponentially. For instance, while four data points may suffice in modeling features across one dimension, sixteen or more may be needed in two dimensions to fully characterize the interdependencies and interactions. As such, adding features without sufficient data can obscure rather than clarify underlying relationships.

This trade-off is formalized in the curse of dimensionality, also known as the Hughes or peaking phenomenon, which describes the point where model performance degrades as feature count exceeds available data support. Wearable research datasets are especially susceptible to overfitting due to sensor variability, limited subject pools, and the logistical challenges of longitudinal studies. Data distributions are often uneven, clustered, subjective, and noisy, complicating model generalization strategies.

Unlike dimensionality, data volume imposes no theoretical upper bound on performance. Early data accumulation yields steep improvements, followed by diminishing returns as accuracy plateaus. Empirical validation on held-out test sets remains the standard for assessing whether sufficient data has been collected.

In data-constrained settings, enhancing feature quality is more impactful than simply increasing quantity. Robust, low-noise, and physiologically meaningful

features enable models to generalize with fewer samples. A key objective in wearable health analytics is to develop preprocessing and analytic pipelines that reduce noise and redundancy while preserving interpretability—ensuring that extracted features not only improve prediction accuracy but also retains biomedical relevance.

3.3.2 Feature selection strategies

Feature selection aims to identify the most informative, nonredundant subset of information that meaningfully contributes to model performance. While exhaustive search—evaluating all possible combinations—is guaranteed to yield an optimal feature set for static architectures, it is computationally prohibitive for high-dimensional datasets or adaptive models due to the exponential growth in training time. Nevertheless, brute-force feature selection remains widely used within research domains, such as in brain–machine interface biomarker identification[11], acoustic-based disease screening[12], and cancer detection from medical images.

To address the limitations of exhaustive approaches, a range of statistical and model-based algorithms have been developed. Among the most widely used are Principal Component Analysis (PCA), Linear Discriminant Analysis (LDA), and Shapley Additive Explanations (SHAP). PCA is an unsupervised dimensionality reduction method that transforms potentially correlated features into orthogonal principal components through an eigenvalue decomposition. These components,

expressed as linear combinations of the original features, capture the directions of maximal variance across the dataset. PCA has been successfully applied in diverse biomedical applications, including cancer classification[13], gene expression across cell lines[14] (**Fig. 3.2B**), and metabolite discovery and diagnostics[15].

In contrast, LDA is a supervised technique that identifies the linear combinations of features which maximize class separability. While both PCA and LDA are commonly used in biomarker discovery[16], PCA is preferred for exploratory analysis of unlabeled data, whereas LDA is more effective in classification tasks, particularly when the feature space is noisy. LDA explicitly accounts for inter-class variability, whereas PCA may preserve noise if it contributes significantly to overall variance.

Recently, SHAP analysis has emerged as a popular alternative for quantifying feature importance, offering a game-theory framework to assess the marginal contribution of each feature to the model's prediction[17]. SHAP values are calculated by comparing the model's output with and without a given feature across all permutations, providing interpretability at an individual feature level. SHAP has been applied to diverse modalities, from sweat-based drug detection[18] to image-based structural analysis for molecular activity predictions[19] (**Fig. 3.2C**). Despite its interpretability, SHAP is computationally expensive when applied to large feature spaces due to the model retraining across feature subsets.

Other techniques not discussed above include Local Interpretable Model-Agnostic Explanations (LIME)[20], Single Feature Importance (SFI), and Mean Decrease Accuracy (MDA). Ensemble approaches have also demonstrated success in metabolite discovery[21] and other biomarker identification tasks by combining the strengths of individual algorithms. However, this approach comes at the cost of significant computational overhead, especially when applied to large and heterogeneous feature pools.

3.3.3 Model architectures

A wide range of machine learning algorithms have been applied across wearable sensing applications, often with overlapping success. This diversity makes it challenging to determine the optimal architecture for a given task. For instance, convolutional neural networks (CNNs) have been used to quantify lactate in the sweat with an F1 score of 0.990[8], while decision trees have achieved a root mean squared error of 0.1 mg/dL for glucose[22]. Furthermore, k-nearest neighbors (KNN) algorithms have been employed to correct sensor drift in cortisol detection[23], in measuring tyrosine, and predicting uric acid levels[24] (**Fig. 3.2D**). Beyond chemical quantification, wearable systems have also leveraged random forests to detect depression[6], support vector machines to classify emotional states[7], and logistic regression to identify stress[25]. This broad utility across models and domains raises an important question: to what extent does model architecture matter when many algorithms yield similarly high accuracy?

In practice, machine learning models do not generate patterns but serve as tools to expose existing relationships between input features and observable outcomes. As such, different models can often achieve similar results by mapping input–output relationships through distinct computational pathways. Model selection should therefore be guided by practical constraints, including computational efficiency, interpretability, and reproducibility.

Complex models excel at uncovering subtle trends within noisy or high-dimensional data, such as inferring ethnicity or age from sweat lipid profiles using gradient boosting trees[26]. However, their performance gains come with drawbacks. Deep architectures require larger datasets to avoid overfitting and often act as black boxes, offering limited insight into why specific features are relevant. For example, a seven-layer convolutional neural network was used to monitor Parkinson's disease progression via wearable data[27], yet the physiological rationale behind the predictive features remained unclear. Similarly, deep learning methods have been used to surpass detection limits for metal ions in sweat[28], but reproducibility remains a challenge due to sensor variability, subject differences, and algorithmic randomness.

Ultimately, model selection represents a trade-off between complexity and interpretability. While advanced architectures may yield marginal improvements in accuracy, their deployment must consider transparency, reproducibility, and

resource efficiency—particularly in the context of real-world wearable health applications.

3.4 Model generalizability

The generalizability of machine learning models across populations within emerging wearable platforms is commonly overlooked due to the difficulties in sampling enough data points across all genders, ethnicities, race, age, education, and sexuality[32]. However, prejudice is quite common in many AI-based platforms already being used within industry. In practice, when trained across the whole population, ML models preferentially mislabel people from minority groups, but when applied to each individual subgroup, the models maintains its high accuracy[33]. Recognizing that there is a racial, gender, sexuality, and age component in medical data reaffirms the need to account for such risk factors in machine learning applications, preventing an algorithm from finding a local optimum that fits most of the population while underperforming on specific minority groups. This highlights the need to develop biomarker and platform agnostic data analysis strategies that can readily learn biometric patterns across populations, without exhaustively resampling for each new platform alteration.

3.5 Conclusion

Machine learning can be applied to the development of physiochemical sensors, personalized healthcare, and biomarker discovery. When developing machine learning models from wearable health data, there are a variety of factors to

consider from input features to model architecture. Adding robust, nonoverlapping information is the best way to increase the accuracy of a model; however, selecting these features can often be challenging as different feature selection algorithms may favor specific machine learning methods. When constructing a machine learning model, simple architectures with a small subset of features provide greater insight into the underlying mechanisms of how the feature-space maps the health of the patient. Therefore, while it is attractive to work on complex designs with many features, limiting the scope of the analysis can afford a deeper understanding of how each feature pairing effects the final diagnosis and health of the patient.

Finally, as the innovation in wearable technology scales, so does the collection and storage of private health information, creating a concern about the potential misuse of user medical data. The consequence of improperly handling sensitive information is that users can be targeted due to their security information and discriminated against based on their medical history. Due to this inherent risk, customers can often be skeptical about using wearable technology. The lack of trust in data protection, lack of control, and gaps in the legislature all contribute to this negative perception. To increase the adoption of valuable wearable medical devices, we must properly consider the storage, transmission, and use-cases of sensitive medical information when developing and researching new products.

References

1. Hudgins, B., Parker, P. & Scott, R. N. A new strategy for multifunction myoelectric control. *IEEE Trans Biomed Eng* **40**, 82–94 (1993).
2. Osborn, L. E. *et al.* Prosthesis with neuromorphic multilayered e-dermis perceives touch and pain. *Sci. Robot.* **3**, eaat3818 (2018).
3. A neuro-inspired artificial peripheral nervous system for scalable electronic skins. https://www.science.org/doi/10.1126/scirobotics.aax2198 doi:10.1126/scirobotics.aax2198.
4. Li, H. *et al.* A learnable parallel processing architecture towards unity of memory and computing. *Sci Rep* **5**, 13330 (2015).
5. A Scalable Multicore Architecture With Heterogeneous Memory Structures for Dynamic Neuromorphic Asynchronous Processors (DYNAPs). https://xplorestaging.ieee.org/document/8094868?denied=.
6. Kumar, S. & Chong, I. Correlation Analysis to Identify the Effective Data in Machine Learning: Prediction of Depressive Disorder and Emotion States. *International Journal of Environmental Research and Public Health* **15**, 2907 (2018).
7. Sharma, K., Castellini, C., Van Den Broek, E. L., Albu-Schaeffer, A. & Schwenker, F. A dataset of continuous affect annotations and physiological signals for emotion analysis. *Sci Data* **6**, 196 (2019).
8. Yüzer, E., Doğan, V., Kılıç, V. & Şen, M. Smartphone embedded deep learning approach for highly accurate and automated colorimetric lactate analysis in sweat. *Sensors and Actuators B: Chemical* **371**, 132489 (2022).
9. Monge, J. *et al.* Glucose Detection in Sweat using Biosensors. in *2019 E-Health and Bioengineering Conference (EHB)* 1–5 (2019). doi:10.1109/EHB47216.2019.8970023.
10. Zeng, A., Chen, M., Zhang, L. & Xu, Q. Are Transformers Effective for Time Series Forecasting? Preprint at https://doi.org/10.48550/arXiv.2205.13504 (2022).
11. Mend, M. & Kullmann, W. H. Human computer interface with online brute force feature selection. *Biomedical Engineering / Biomedizinische Technik* **57**, 659–662 (2012).
12. Stasak, B., Huang, Z., Razavi, S., Joachim, D. & Epps, J. Automatic Detection of COVID-19 Based on Short-Duration Acoustic Smartphone Speech Analysis. *J Healthc Inform Res* **5**, 201–217 (2021).
13. Hasan, H. & Tahir, N. M. Feature selection of breast cancer based on Principal Component Analysis. in *2010 6th International Colloquium on Signal Processing & its Applications* 1–4 (2010). doi:10.1109/CSPA.2010.5545298.
14. Fujisawa, K., Shimo, M., Taguchi, Y.-H., Ikematsu, S. & Miyata, R. PCA-based unsupervised feature extraction for gene expression analysis of COVID-19 patients. *Sci Rep* **11**, 17351 (2021).
15. Delgado-Povedano, M. del M., Calderón-Santiago, M., Priego-Capote, F., Jurado-Gámez, B. & Luque de Castro, M. D. Recent advances in human sweat metabolomics for lung cancer screening. *Metabolomics* **12**, 166 (2016).

16. Suhail, Z., Denton, E. R. E. & Zwiggelaar, R. Classification of micro-calcification in mammograms using scalable linear Fisher discriminant analysis. *Med Biol Eng Comput* **56**, 1475–1485 (2018).
17. Lundberg, S. M. & Lee, S.-I. A Unified Approach to Interpreting Model Predictions. in *Advances in Neural Information Processing Systems* vol. 30 (Curran Associates, Inc., 2017).
18. Bittremieux, W. *et al.* Physicochemical properties determining drug detection in skin. *Clinical and Translational Science* **15**, 761–770 (2022).
19. Rodríguez-Pérez, R. & Bajorath, J. Interpretation of machine learning models using shapley values: application to compound potency and multi-target activity predictions. *J Comput Aided Mol Des* **34**, 1013–1026 (2020).
20. Ribeiro, M. T., Singh, S. & Guestrin, C. 'Why Should I Trust You?': Explaining the Predictions of Any Classifier. Preprint at https://doi.org/10.48550/arXiv.1602.04938 (2016).
21. An ensemble feature selection method for biomarker discovery | IEEE Conference Publication | IEEE Xplore. https://ieeexplore.ieee.org/abstract/document/8388679.
22. A machine learning-based on-demand sweat glucose reporting platform | Scientific Reports. https://www.nature.com/articles/s41598-022-06434-x.
23. Shahub, S., Upasham, S., Ganguly, A. & Prasad, S. Machine learning guided electrochemical sensor for passive sweat cortisol detection. *Sensing and Bio-Sensing Research* **38**, 100527 (2022).
24. Kammarchedu, V., Butler, D. & Ebrahimi, A. A machine learning-based multimodal electrochemical analytical device based on eMoSx-LIG for multiplexed detection of tyrosine and uric acid in sweat and saliva. *Analytica Chimica Acta* **1232**, 340447 (2022).
25. Pandey, P. S. Machine Learning and IoT for prediction and detection of stress. in *2017 17th International Conference on Computational Science and Its Applications (ICCSA)* 1–5 (2017). doi:10.1109/ICCSA.2017.8000018.
26. Zhou, Z. & Zare, R. N. Personal Information from Latent Fingerprints Using Desorption Electrospray Ionization Mass Spectrometry and Machine Learning. *Anal. Chem.* **89**, 1369–1372 (2017).
27. Um, T. T. *et al.* Data augmentation of wearable sensor data for parkinson's disease monitoring using convolutional neural networks. in *Proceedings of the 19th ACM International Conference on Multimodal Interaction* 216–220 (Association for Computing Machinery, New York, NY, USA, 2017). doi:10.1145/3136755.3136817.
28. Cho, S.-Y. *et al.* Finding Hidden Signals in Chemical Sensors Using Deep Learning. *Anal. Chem.* **92**, 6529–6537 (2020).
29. Li, H., Wu, J., Gao, Y. & Shi, Y. Examining individuals' adoption of healthcare wearable devices: An empirical study from privacy calculus perspective. *Int J Med Inform* **88**, 8–17 (2016).
30. Arış, A., Oktuğ, S. F. & Yalçın, S. B. Ö. Internet-of-Things security: Denial of service attacks. in *2015 23nd Signal Processing and Communications*

Applications Conference (SIU) 903–906 (2015). doi:10.1109/SIU.2015.7129976.

31. Xie, Y. *et al.* Integration of Artificial Intelligence, Blockchain, and Wearable Technology for Chronic Disease Management: A New Paradigm in Smart Healthcare. *CURR MED SCI* **41**, 1123–1133 (2021).
32. Gianfrancesco, M. A., Tamang, S., Yazdany, J. & Schmajuk, G. Potential Biases in Machine Learning Algorithms Using Electronic Health Record Data. *JAMA Intern Med* **178**, 1544–1547 (2018).
33. Klare, B. F., Burge, M. J., Klontz, J. C., Bruegge, R. W. V. & Jain, A. K. Face Recognition Performance: Role of Demographic Information. *IEEE Trans. Inf. Forensic Secur.* **7**, 1789–1801 (2012).

Chapter 4

STATE ANXIETY BIOMARKER DISCOVERY

Materials from this chapter appear in "Dao, J., Liu, R., Solomon, S. L. & Solomon, S. A. State Anxiety Biomarker Discovery: Electrooculography and Electrodermal Activity in Stress Monitoring. Preprint at https://doi.org/10.48550/arXiv.2411.17935."

Mental health has become a serious public concern, intensified by the recent COVID-19 pandemic, with state anxiety increasingly recognized for its implications in both mental and cardiovascular health. This study assesses the viability of non-invasive wearable technologies for real-time physiological monitoring of state anxiety. Specifically, it examines negative affective states across two sensing modalities: electrooculography and electrodermal activity. By analyzing blink rate variability, skin conductance peaks, and arousal-related features, we identify biomarker characteristics strongly correlated with anxious mental states. To enhance model transparency and clinical interpretability, we employ SHapley Additive exPlanations to quantify feature relevance and refine predictive models. Our findings indicate that integrating electrooculography and electrodermal activity data improves sensitivity in modeling anxiety-related physiological responses, underscoring the promise of multimodal sensing in wearable health systems. This work contributes to the development of personalized, real-time anxiety assessment tools, thereby facilitating more effective mental health interventions within wearable platforms.

4.1 Introduction

Momentary state-anxiety (SA) represents an assembly of different emotions[11] that are captured within measurable physiological responses[2]. Although episodic in nature, sustained or recurrent SA has been linked to adverse outcomes across both cardiovascular and autonomic nervous systems[3]. Despite its high prevalence and comorbidity with mental disorders, reliable physiological signatures of SA

remain poorly defined within different sensory pathways. The identification of robust, interpretable biomarkers is critical for early detection and intervention. Wearable technologies thereby present new opportunities for continuous, non-invasive monitoring of stress-related states.

Recent advances in wearable biosensing platforms have enabled the real-time acquisition of high-resolution physiological data streams, including electrodermal activity (EDA) and electrooculography (EOG). While each modality has demonstrated sensitivity to emotional arousal, no single signal reliably captures anxiety when used in isolation. EDA, for instance, is a widely accepted marker of sympathetic nervous system arousal but lacks specificity—responding indiscriminately to both positive and negative affective stimuli. Similarly, EOG is modulated by both stress and fatigue. The context-dependent nature of these signals—shaped by baseline physiology, environmental stimuli, pharmacological factors, and individual differences—necessitates a multimodal, context-aware approach to biomarker discovery.

This chapter introduces a data-driven framework for identifying state anxiety biomarkers by jointly analyzing EDA and EOG signals through the lens of the two-factor emotion model, which posits that emotional states result from the dynamic interplay between physiological arousal and cognitive appraisal[4]. We investigate how blink dynamics and sweat-induced changes in skin conductance tracks stress responses under controlled sympathetic activation, particularly

during a cold pressor test (CPT)—a validated method for eliciting acute anxiety-like responses[5,6]. Moving beyond traditional signal averaging and coarse features, we leverage high-resolution time-series analytics and contextual annotations to uncover nuanced physiological patterns indicative of SA.

In support of this work, we collected EOG signals focused on blink morphology and noise discrimination as well as synchronized EOG and EDA recordings with demographic metadata, affective profiles, and physiological responses during CPT. Using SHapley Additive exPlanations (SHAP), we assess the contribution of candidate features and evaluate their stability across individuals and conditions[7]. Our approach prioritizes transparency and generalizability, enabling the translation of laboratory findings into real-world wearable applications.

Ultimately, this work offers new biomarkers for detecting state anxiety. By identifying interpretable and generalizable physiological markers, we contribute to the development of the next-generation of wearable systems for personalized mental health monitoring and adaptive intervention.

4.2 Dataset evaluation and experimental protocols

The study was conducted within a controlled research setting, with participants selected across different demographic backgrounds. Exclusion criteria included pregnancy, inability to provide informed consent, use of medications affecting psychiatric state, and psychiatric or physical conditions such as depression, anxiety, or chronic cardiovascular diseases (e.g., hypertension, hyperlipidemia).

The demographic of the participants was 65% Asian (38% female and 62% male), 10% Hispanic or Latino (50% male and 50% female), 5% Middle Eastern or North African (all male), 15% White (67% male and 33% female), and 5% Black or African American (all male). The age of participants ranged from 19 to 32 years, with educational backgrounds spanning from a high school diploma to a doctoral degree, ensuring a diverse representation of academic experiences.

Before each study, participants completed demographic forms and a screening questionnaire. The platform was mounted onto the forehead after skin cleansing with alcohol wipes to ensure optimal sensor contact. Baseline stress levels were assessed using the Positive Affect and Negative Affect Schedule (PANAS) and State Trait Anxiety Inventory (STAI) Y1 questionnaire at both the beginning and end of each session. During baseline evaluations, participants sat in a neutral position, remaining silent before completing the surveys. Each experimental condition lasted between 2–4 minutes, during which subjects were instructed to focus on their dominant emotional states.

The cold pressor protocol consisted of three consecutive sections, with the first and last components serving as baseline measurements. After completing the initial PANAS and STAI questionnaires, participants immersed their forearm into an ice bath (0°C) for 2-3 minutes. After removing their hand from the ice water, subjects again completed the PANAS and STAI assessments. This

structure enabled the collection of three stress evaluation points per participant per experimental session.

4.2.1 PANAS and STAI-Y1 scoring methodologies

The stress response can be activated by both positive and negative stimuli. Despite their similarities, positive and negative stressors do not follow a strict inverse relationship and can be triggered simultaneously by the same event. For instance, an individual may experience positive emotions upon graduating college while simultaneously feeling negative emotions about future uncertainty. In the context of mental health interventions, distinguishing eustress (e.g., motivation, engagement) from distress (e.g., guilt, anger) is critical, as therapeutic strategies should target negative stressors while maintaining healthy levels of positive stress that contributes to both motivation and resilience.

We selected the PANAS and STAI examinations for their high internal reliability, capacity to distinguish positive and negative affections, and short administration time that minimizes interruptions during experimental trials. The PANAS has demonstrated high internal consistency, with a Cronbach's alpha ranging from 0.86 to 0.90 for positive affect and 0.84 to 0.87 for negative affect across diverse populations. The PANAS questionnaire consisted of 10 items, with 5 positive affect (PA) and 5 negative affect (NA) descriptors, each rated on a 5-point Likert scale (1 = "very slightly or not at all" to 5 = "extremely"). Meanwhile the STAI Y1 exam consisted of 20 items, 10 positive and 10 negative anxiety-related

emotions, each rated on a 4-point Likert scale (1 = "not at all" to 5 = "very much so"). A strong test-retest reliability across both surveys ensured robust emotional assessments in dynamic experimental conditions. Within our study, the total and separate PA and NA ratings ranged from 5 to 25 points and state-anxiety scores ranged from 20 to 80 points.

The negative STAI emotions sampled were the following: I am tense, I feel strained, I feel upset, I am presently worrying over possible misfortunes, I feel frightened, I feel nervous, I am jittery, I feel indecisive, I am worried, and I feel confused. The negative affect emotions sampled were Upset, Hostile, Ashamed, Nervous, and Afraid.

The positive STAI emotions sampled were the following: I feel calm, I feel secure, I feel at ease, I feel satisfied, I feel comfortable, I feel self-confident, I am relaxed, I feel content, I feel steady, and I feel pleasant. The positive affect emotions sampled were Alert, Inspired, Determined, Attentive, and Active.

4.2.2 Single channel streaming of encrypted wireless signals

The voltage from each biomarker was sampled on the ESP32-S3 ADC port once every 3.5 ms. Each signal was streamed into the same ADC port to minimize conversion errors due to rapid analog port switching. A multiplexer with a switch rate of approximately 64 ns was used to feed each signal independently into the ADC channel. A 10 uF capacitor was placed before each multiplexer input to

reduce the incoming impedance to the ADC port as well as hold voltages in between sampling periods.

Encrypted wireless transmission: Wireless data streaming between two ESP32-S3 systems was performed using the ESP-NOW communication protocol developed by Espressif Systems. The ESP-Now protocol provides a stable and fast encrypted wireless transmission protocol, allowing for data transmission up to 190 meters away without access to any local internet network. Like any wireless protocol, some data packets can be lost to the air due to network congestion, hardware issues, or failed connection. Given proper setup, the main reason for data loss is due to network congestion: sending information faster than it can be received. When sending characters over the ESP-NOW protocol every 3.5 ms, we found that the largest data packet we could send without loss was 20 bytes. However, streaming in biomarkers alongside their respective timestamps can be slow.

We therefore compress the biometric information before wireless transmission. Each byte transmitted represents an 8-bit data packet that can be hashed to a number or symbol using an ASCII mapping. While this mapping allows for a broad range of applications, we note that we only utilize numbers 0 – 9, where all ten digits can be represented by 4-bits.

$$|\,0 = 0000\,| \quad |\,1 = 0001\,| \quad |\,2 = 0010\,| \quad |\,3 = 0011\,| \quad |\,4 = 0100\,|$$

$$|5 = 0101| \quad |6 = 0110| \quad |7 = 0111| \quad |8 = 1000| \quad |9 = 1001|$$

Since each ASCII character is 8-bits regardless of its value, half of the transmitted data would be a waste of memory (prepended zeros). Therefore, to reduce the number of bytes transmitted, we perform bit-packing by splices two adjacent bytes into one, reducing the memory by a factor of two. As an example, we can compress the number "4095" from 32 bits to 16 bits as follows:

$$|4 = \mathbf{0100}| \quad |0 = \mathbf{0000}| \quad |9 = \mathbf{1001}| \quad |5 = \mathbf{0101}|$$

$$|@ = 01000000| \quad |ò = 10010101|$$

Sending "4095" contains the same information as sending "@ò" after byte decompression. Each byte is decompressed in python, freeing up the ESP32-S3 to send/receive more data packets.

4.2.3 Asynchronous data streaming and preprocessing

All EOG and EDA signals were streamed in real-time from a custom PCB module, where incoming data was filtered and processed for feature extraction for downstream affective analysis. Physiological signals are transmitted at an average sampling frequency of 276 Hz. Each biomarker is continuously updated in memory with a rolling buffer and segmented into overlapping batches of 4000 points with a sliding window of 400 points, where data preprocessing is performed asynchronously to data streaming. This extra 3600-point buffer ensures numerical stability during forward-backward filtering using cascaded

second-order sections. For noisy signals, an artifact rejection pipeline removes segments where voltage readings fall outside numerical precision limits (below 0.1V or above 3.18V), ensuring robustness against contamination from electrode displacement and excessive motion artifacts.

For EOG preprocessing, a Butterworth bandpass filter (0.5–15 Hz, order 5) and a Savitzky-Golay filter (0.05 second window, second-degree polynomial) were applied to suppress low-frequency drifts and high-frequency noise from muscle activity and external interference.

For EDA preprocessing, a Butterworth low-pass filter (15 Hz, order 3) was applied before splitting the data into tonic (baseline) and phasic components, where the baseline was extracted through a Butterworth low-pass filter (0.5 Hz, order 1). All tonic and phasic features were extracted every second within a sliding 15 and 12 second time windows respectively.

4.3 Blink identification model

To isolate spontaneous blink events from movement-related artifacts, we developed a classification model based on five key blink attributes. Our approach extends prior work on non-intentional blink detection[8] by focusing on interpretable signal features (**Fig. 4.1**), particularly those tied to blink duration, slope, and temporal variability. Using blink duration alone, we achieved a classification accuracy of 87.46% and an F1 score of 0.7999 in distinguishing

blink events from wire movement artifacts—highlighting the discriminative power of well-chosen features, even in the absence of deep learning.

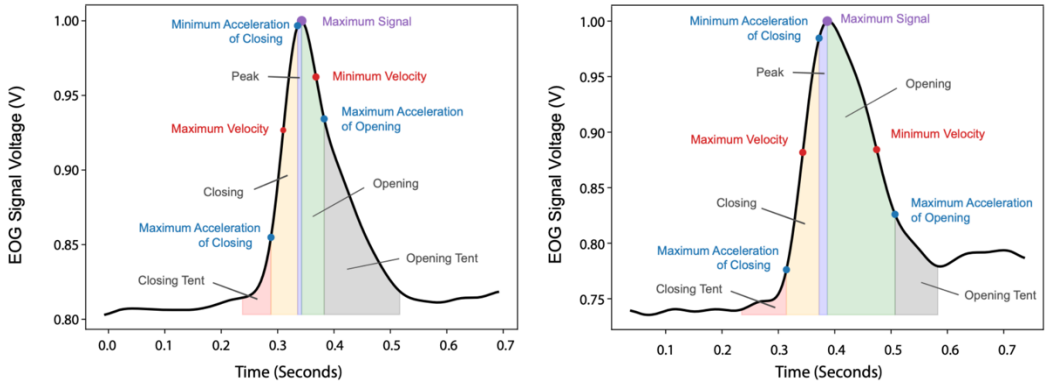

Figure 4.8 Blink segmentation and feature extraction. Two EOG blinks identified within the dataset with important feature characteristics highlighted.

To further improve classification performance, we systematically evaluated all possible feature combinations using a breadth-first search (BFS) traversal methodology. For each feature combination, we defined upper and lower bounds discretized into 15 bins. Each configuration of bounds formed a node in the BFS queue, with a delta step size derived from the bin width. The traversal proceeded by iteratively evaluating the classification accuracy and F1 score of each configuration using a performance function. When a new configuration outperformed the previous best configuration, it was recorded as the new current optimum. Neighboring configurations were then generated by incrementally tightening the bounds—squeezing the lower and upper bounds by one delta step—and enqueued for further evaluation.

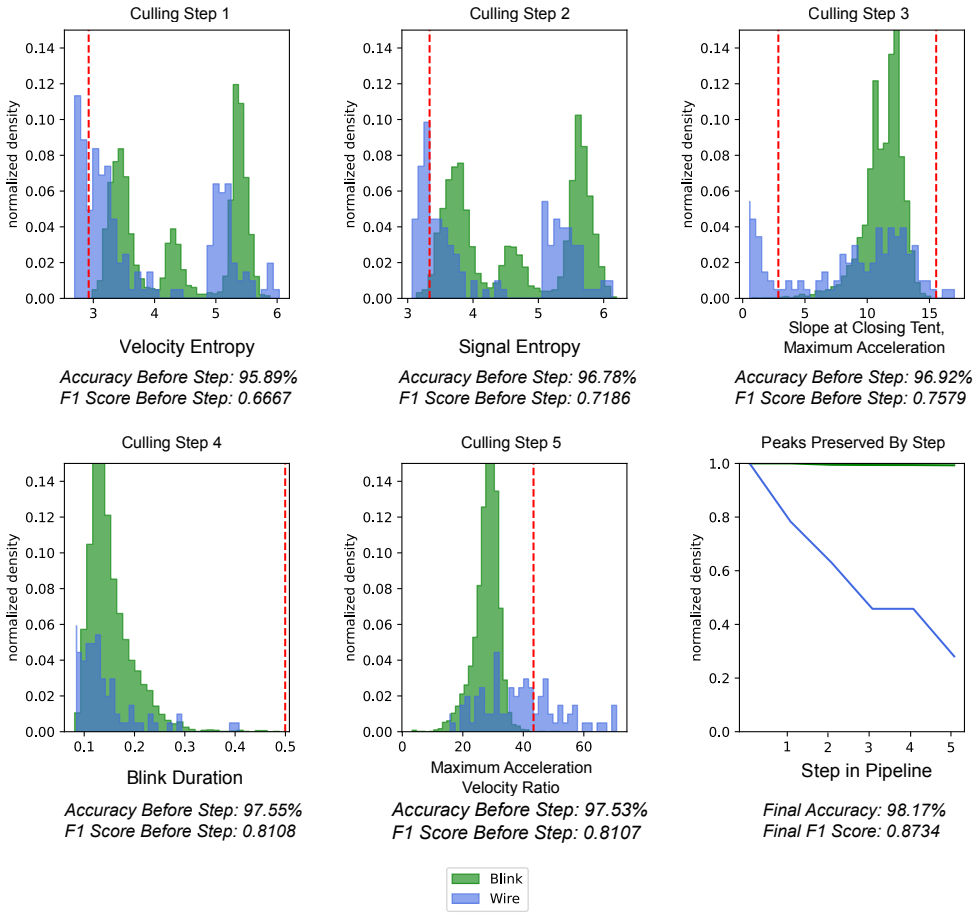

Figure 4.9 Blink identification and differentiation. This figure presents the sequential culling steps optimized to achieve the highest accuracy and F1 score in distinguishing blink events (green) from wire artifacts (blue) in EOG data. Each subplot demonstrates a unique culling step, applying specific feature thresholds to progressively refine the data. The final subplot illustrates the proportion of retained peaks at each stage for both blink and wire signals.

This traversal continued until all relevant permutations had been explored, yielding an empirically optimized culling strategy tailored to each feature combination (**Fig. 4.2**). The highest-performing configuration achieved an accuracy of 98.17% and an F1 score of 0.8734. The final feature set captured

distinct aspects of blink morphology: the entropy of the signal and its first derivative, the maximum acceleration during the closing phase, the total blink duration, and the ratio between maximum acceleration and velocity. These features collectively represented the temporal complexity, peak dynamics, and symmetry of blink events—enabling robust differentiation from motion artifacts.

4.4 Physiological associations with state anxiety

To enhance interpretability and understand the influence of individual features on affective predictions, we applied a SHAP analysis to predict state anxiety, negative affectivity, and positive affectivity. A SHAP analysis is a model-agnostic explanation framework grounded in cooperative game theory, which attributes each prediction to the additive contributions of individual features. By treating each feature as a "player" in a cooperative game, SHAP values quantify how each feature contributes to determining the model output, providing a principled way to dissect model behavior.

The overall quality of a feature set is evaluated using the mean absolute SHAP values across all samples, where higher values indicate greater overall importance. Importantly, this metric captures not only individual feature relevance but also the extent to which features interact to form meaningful and predictive combinations. SHAP analysis thus offers an interpretable benchmark for selecting feature combinations that maximize both predictive power and model robustness.

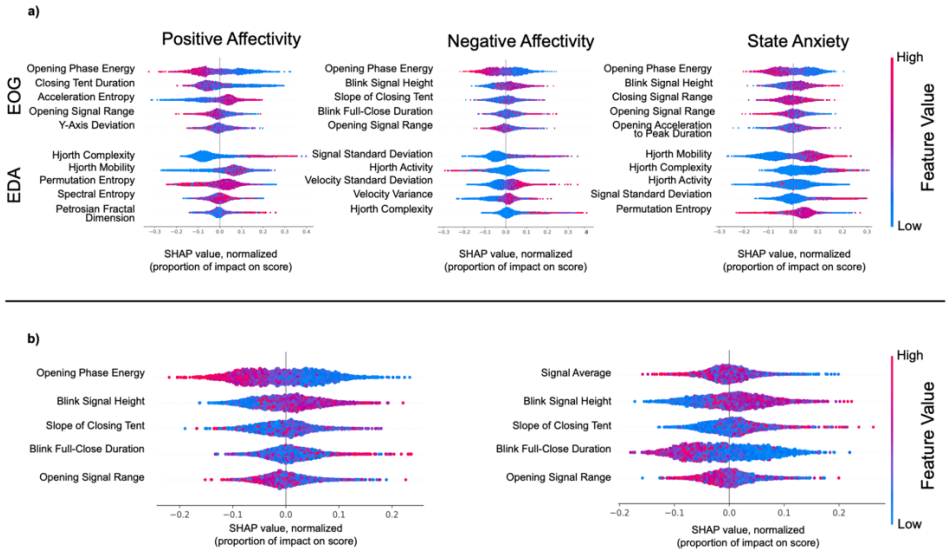

Figure 4.10 SHAP analysis of affective features. A) SHAP Analyses for optimal combinations of five EOG Features (top row) and five EDA Features (bottom row), for Positive Affectivity (left column), Negative Affectivity (middle column), and State Anxiety (right column) predictions. B) This analysis explores how different sets of features distinguish affectivity levels. Here, we show five EOG features and their impact on the Negative Affectivity score. Substituting one key feature with another can reveal new interdependencies among remaining features, thereby enhancing the model's interpretability.

The SHAP value distributions for both EOG and EDA features across three mental state prediction tasks are shown for positive affectivity, negative affectivity, and state anxiety measurements (**Fig. 4.3A**). Each subplot visualizes the influence of individual feature contributions to the model output, where higher SHAP values (rightward shift) indicate stronger positive contributions, and lower values (leftward shift) represent negative contributions. These maps allow for a direct interpretation of feature influence on classification outcomes.

Within the EOG domain, Opening Phase Energy—defined as the integral of the signal during the initial portion of the blink—and Opening Signal Range—the amplitude of that same phase—emerged as consistent influential features across all three affective outputs. Their repeated appearance in optimal feature combinations highlight their utility as robust, generalizable blink biomarkers. Meanwhile, Signal Height, another EOG-derived metric, was predictive of negative affectivity and state anxiety.

From the EDA signal space, Hjorth parameters and Signal Standard Deviation demonstrated the strongest relevance across all outputs. These features capture the statistical and spectral characteristics of skin conductance dynamics, supporting their role as meaningful indicators of physiological arousal under cold pressure stress.

SHAP comparisons further revealed the importance of feature context. The inclusion of Opening Phase Energy yielded the clearest separation in SHAP distributions, marking it as a pivotal feature in the five-feature combination selected for analysis (**Fig. 4.3B**). When this feature was omitted, model performance declined, and features such as the Blink Full-Close Duration began exhibiting greater distinction—likely compensating for the missing signal dimension. This shift underscores the importance of analyzing features not only in isolation but also in coordinated sets, where interactions among temporally and biomechanically linked features contribute significantly to prediction accuracy.

Together, these results highlight the value of interpretable machine learning in identifying meaningful, physiologically grounded biomarkers. They emphasize the role of signal morphology and temporal structure in modeling affective states, offering insight into how blink dynamics and skin conductance jointly encode stress and emotion-related responses.

4.5 Conclusion

This study demonstrates the potential of electrooculography and electrodermal activity as complementary modalities for identifying physiological biomarkers associated with state anxiety. Through the development and analysis of this dataset, we combined high-resolution feature extraction with interpretable machine learning techniques to uncover anxiety-specific signal patterns. By integrating SHAP analysis into our pipeline, we moved beyond identifying isolated features and instead characterized how groups of features interact to shape model predictions—advancing a more nuanced, context-aware understanding of physiological responses to stress.

While metrics such as blink duration and skin conductance peaks have been explored previously, we show that their predictive value is highly dependent on contextual factors, including the nature and intensity of the stressor. For instance, features that were effective under cold pressure may not generalize to more cognitively driven stressors such as public speaking. This highlights the necessity

of building adaptive models that incorporate context to maintain reliability across varying real-world scenarios.

One of the central contributions of this work is the identification of robust feature combinations that consistently enhance model performance. In EOG signals, blink duration, peak amplitude, and opening-phase integrals emerged as stable predictors across multiple affective states. For EDA, features such as mean signal amplitude, permutation entropy, and Hjorth activity contributed significantly to the classification accuracy. SHAP analysis revealed not only the relative importance of each feature, but also their interaction dynamics, offering interpretability without compromising predictive power.

Together, these results provide a systematic framework for addressing the variability and situational dependence of physiological biomarkers. By emphasizing feature interactions and context-sensitive model designs, this work lays the groundwork for more robust and generalizable anxiety assessment tools. Ultimately, these advances bring wearable biosensing closer to enabling real-time, personalized mental health interventions that are responsive to the dynamic nature of human emotional experiences.

References

1. Freud, S. *Inhibitions, Symptoms, and Anxiety*. (Norton, New York, 1989).
2. Cognitive, Social, and Physiological Determinants of Emotional State. In: Psychological Review 69(5): 379-399. *ResearchGate* https://www.researchgate.net/publication/9090242_Cognitive_Social_and_Physiological_Determinants_of_Emotional_State_In_Psychological_Review_695_379-399.
3. McEwen, B. S. Physiology and Neurobiology of Stress and Adaptation: Central Role of the Brain. *Physiological Reviews* **87**, 873–904 (2007).
4. Schachter, S. & Singer, J. Cognitive, social, and physiological determinants of emotional state. *Psychological Review* **69**, 379–399 (1962).
5. Bullock, T. *et al.* Habituation of the stress response multiplex to repeated cold pressor exposure. *Front. Physiol.* **13**, (2023).
6. McIntyre, M. H., Kless, A., Hein, P., Field, M. & Tung, J. Y. Validity of the cold pressor test and pain sensitivity questionnaire via online self-administration. *PLoS One* **15**, e0231697 (2020).
7. Lundberg, S. M. & Lee, S.-I. A Unified Approach to Interpreting Model Predictions. in *Advances in Neural Information Processing Systems* vol. 30 (Curran Associates, Inc., 2017).
8. BLINKER: Automated Extraction of Ocular Indices from EEG Enabling Large-Scale Analysis - PMC. https://pmc.ncbi.nlm.nih.gov/articles/PMC5289990/.

Chapter 5

PHYSICOCHEMICAL STRESS RESPONSE MONITORING

Materials from this chapter appear in "Xu, C.; Song, Y.; Sempionatto, J. R.; Solomon, S. A.; Yu, Y.; Nyein, H. Y. Y.; Tay, R. Y.; Li, J.; Heng, W.; Min, J.; Lao, A.; Hsiai, T. K.; Sumner, J. A.; Gao, W. A physicochemical-sensing electronic skin for stress response monitoring. Nat Electron 7, 168–179 (2024). https://doi.org/10.1038/s41928-023-01116-6."

Approaches to quantify stress responses typically rely on subjective surveys and questionnaires. Wearable sensors can potentially be used to continuously monitor stress-relevant biomarkers. However, the biological stress response is spread across the nervous, endocrine and immune systems, and the capabilities of current sensors are not sufficient for condition-specific stress response evaluation. Here we report an electronic skin for stress response assessment that non-invasively monitors three vital signs (pulse waveform, galvanic skin response and skin temperature) and six molecular biomarkers in human sweat (glucose, lactate, uric acid, sodium ions, potassium ions, and ammonium). We develop a general approach to prepare electrochemical sensors that relies on analogous composite materials for stabilizing and conserving sensor interfaces. The resulting sensors offer long-term sweat biomarker analysis of more than 100 h with high stability. We show that the electronic skin can provide continuous multimodal physicochemical monitoring over a 24-hour period and during different daily activities. With the help of a machine learning pipeline, we also show that the platform can differentiate three stressors with an accuracy of 98.0% and quantify psychological stress responses with a confidence level of 98.7%.

5.1 Introduction

Ultimately, stress is a process triggered by demanding physical or psychological events and may cause anxiety as a prototypical psychological response. Although acute stress responses in healthy individuals can be adaptive and manageable, persistent experiences of stress can have deleterious effects on mental and

physical health[1,2], and many mechanisms behind the stress response are yet unknown[3]. In the United States alone, more than 50 million adults suffer from depression, and after the onset of the COVID-19 pandemic, the number of people suffering from mental disorders has drastically risen, causing a heavy burden on the healthcare system[4]. Elevated levels of stress and anxiety also pose a large burden to high-demand occupation workers[5] such as athletes, soldiers, first responders and aviation personnel[6], potentially interfering with their cognitive performance and decision-making process[7]. In response to these effects, understanding and evaluating the stress response has become a cornerstone of clinical healthcare. However, current gold standards for clinical stress response assessments rely on surveys and performance evaluations, which can be highly subjective. Thus, there is a need to develop a more efficient and effective stress assessment tool that is not characterized by these limitations[8].

Non-invasive biomarkers are potentially a reliable alternative for monitoring the stress response because of the interdependencies between biological and psychological stress. Stress induces a complex biological response in the nervous, endocrine and immune systems (**Fig. 5.1A**)[9,10]. The perception of stress activates the hypothalamic–pituitary–adrenal (HPA) axis and sympathetic adrenal medullary axis from the hypothalamus in the brain. Acetylcholine in nerve fibers from both axes stimulates the adrenal gland, releasing stress hormones (for example, epinephrine, norepinephrine, and cortisol) into the blood. Acetylcholine can also activate sudomotor neurons connected to sweat glands that release ion-

rich fluids. This sympathetic activity can be indirectly measured through the galvanic skin response (GSR) and sweat electrolyte levels20. The released stress hormones inhibit insulin production, affecting the synthesis of metabolites such as glucose, lactate, and uric acid (UA), as well as narrow arteries, boosting cardiac activities. By monitoring these stress-relevant biomarkers, it is possible to develop a comprehensive and objective health profile relating biophysical and biochemical signals to dynamic stress response monitoring[11–13].

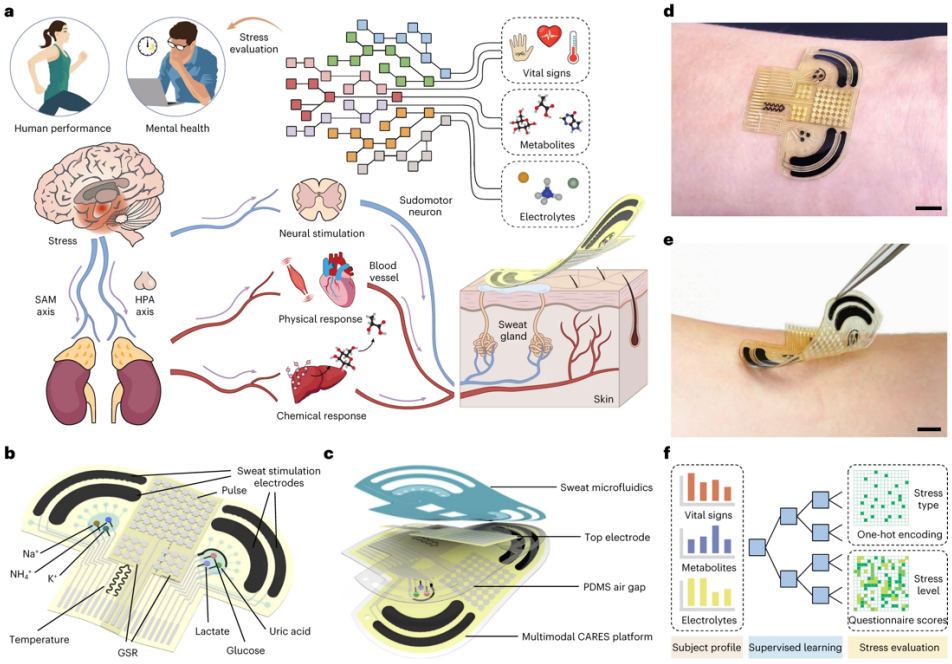

Figure 5.11 Overview of Physicochemical Stress Monitoring. A) Illustration of the CARES patch that continuously monitors multimodal physiological and biochemical responses from the skin and performs artificial-intelligence-powered stress assessments. B) Schematic of the flexible CARES sensor patch and main functionalities: vital sign monitoring, sweat stimulation and sampling, and key metabolite and electrolyte detection. C) Schematic of layered structure of the

CARES that assembles the sensor and microfluidics module. (D, E) Optical images of a CARES attached to the skin of a human subject D) and the soft electronic-skin interface E). Scale bars, 1 cm. f, ML pipeline for CARES-enabled stressor classification and stress/anxiety level assessment. SAM, sympathetic–adreno–medullar.

Recent advances in wearable sensors have enabled real-time and continuous monitoring of physical vital signs[14–17]. Through in situ human sweat analysis, wearable biosensors can provide insightful information about an individual's health at the molecular level[18–21]. However, various challenges remain to be addressed before such sensors can be of use in clinical applications: a limited set of physical signals is not sufficient for condition-specific assessment of psychological and physiological stress[22]; existing wearable biochemical sensors suffer from poor operational stability in biofluids, which precludes reliable long-term continuous monitoring[23]; access to human sweat usually requires physical activity that can affect an individual's stress; and despite recent progress on stress hormone analysis, continuous monitoring of sweat stress hormones at physiologically relevant levels using wearable sensors has not yet been achieved because of the hormones' extremely low concentrations[24,25]. Therefore, although understanding and monitoring the endocrine response to stress is a promising approach, it is still underdeveloped.

In this Article, we report a consolidated artificial-intelligence-reinforced electronic skin (CARES) with robust long-term sensing capabilities for stress response monitoring (**Fig. 5.1A**). Fabricated using a scalable inkjet-printing

approach, the wearable device is capable of multiplexed, non-invasive monitoring of key stress-related physiological signals (pulse waveform, GSR, and skin temperature), sweat metabolites (glucose, lactate, and UA), and electrolytes (Na+, K+, and NH4+) during daily activities (**Fig. 5.1B–C**). Through the integration of a miniaturized iontophoresis (IP) module, sweat can be induced autonomously at rest without the need for vigorous exercise.

We develop a general approach to prepare highly stable and sensitive electrochemical biosensors, which uses analogous composite materials for stabilizing and conserving sensor interfaces. The resulting biochemical sensors offer long-term stability of more than 100 h of continuous operation with minimal signal drifts (amperometric signals decaying less than 0.07% per hour and potentiometric signals drift less than 0.04 mV per hour).

Built on an ultrathin flexible polyimide (PI) substrate (4 μm) for flexibility and robustness as well as integrated with microfluidics, the CARES device conformally laminates on the wrist for reliable and robust sensing (**Fig. 5.1D–E**). This allows for 24-hour continuous monitoring of daily activities, yielding greater insight into how these signals vary throughout the day. With a machine learning (ML) pipeline incorporating previously inaccessible multimodal data (**Fig. 5.1F**), we show that the physicochemical sensor data obtained by the wearable technology can be used to classify responses to stressors at high

accuracies and predict state anxiety levels (a key psychological response to stress) with high reliability.

5.2 Wearable platform development and evaluation

The CARES platform consists of a multilayered sensor patch and a skin-interfaced laser-engraved microfluidic module (**Fig. 5.1D–E**). The sensor patch contains carbachol hydrogel-loaded sweat-stimulation electrodes, three enzymatic biosensors, three ion-selective sensors (ISEs), a capacitive pulse sensor, a resistive GSR sensor, and a skin temperature sensor. The platform can be mass-fabricated through serial inkjet printing of silver and carbon as the interconnects and electrodes for the top and bottom layers. A middle polydimethylsiloxane (PDMS)-based airgap layer was spin-coated between the top and bottom layers, as the soft PDMS facilitates pulse pressure sensitivity and sweat reservoir collection. The microfluidic module was assembled in a sandwiched structure (PDMS/polyethylene terephthalate/medical tape) and contains two separate reservoirs that enable fresh sweat sampling and rapid refreshing for accurate sweat analysis with high temporal resolution. Carbachol was used for sweat induction as it enables long-lasting sudomotor axon reflex sweat secretion from the surrounding sweat glands owing to its nicotinic effects. In this work, six molecular biomarkers (glucose, lactate, UA, Na+, K+, and NH4+) were selected as the detection targets because of their strong associations with stress responses[26–30]. Together with laser-patterned microfluidics, the

CARES device can be attached to the subject's wrist comfortably and performs multiplexed metabolic sensing in situ.

5.2.1 Sensors fabrication for long-term signal fidelity

Serveral electrochemical sensing strategies based on enzymes, ionophores, molecularly imprinted polymers, aptamers and antibodies are reported, and most existing wearable chemical sensors are primarily based on amperometric enzymatic sensors or potentiometric ISEs as these sensors can offer real-time continuous monitoring with high temporal resolution. However, one main bottleneck for the practical applications of these sensors is their limited operation lifetime and long-term stability during continuous wearable sensing. Large sensor drifts are evident when they are used in body fluids, which substantially hinders the long-term continuous usability of wearable chemical sensors.

Most wearable enzymatic biosensors are based on Prussian blue (PB), which serves as an efficient electron-transfer mediator with a low redox potential of around 0 V. However, PB-based biosensors suffer from poor stability during long-term use in biofluids because PB degrades in neutral and alkaline solutions as the hydroxide ions (OH^-), a product of H_2O_2 reduction, can break the Fe–(CN)–Fe bond (Supplementary Note 3). To stabilize PB while retaining its catalytic activity, we use a PB-analogue nickel hexacyanoferrate (NiHCF) with a similar zeolitic crystal structure that is catalytically inactive but forms a stabilized solid solution composite, protecting the PB sensor interface (**Fig.**

5.2A). Additionally, the enzymes were protected in a glutaraldehyde-crosslinked bovine serum albumin (BSA) matrix. To fabricate enzymatic sensors, gold nanoparticles were electrodeposited onto an inkjet-printed inert carbon electrode to provide a high electroactive area for sensitive electrochemical sensing followed by PB–NiHCF deposition. Scanning transmission electron microscopy (STEM) and energy dispersive spectroscopy (EDS) analyses (**Fig. 5.2B**) indicate that NiHCF forms a thin protective layer on PB with an obscure boundary. Our electrochemical characterizations confirmed that compared to PB—which suffered from rapid degradation during electrochemical measurement—and other transition metal hexacyanoferrates (PB–CoHCF and PB–CuHCF), PB–NiHCF could withstand pH corrosion and maintain the most consistent electrochemical catalytic activity. This could be attributed to two mechanisms: (1) nickel is inert compared with iron and can withstand OH^- group corrosion, and (2) the Ni ion has a smaller ionic radius than other transitional metal ions (such as Co and Cu ions), which is better able to withstand ion insertion. Both mechanisms were further supported with scanning electron microscope characterizations of the electrodes and inductively coupled plasma–mass spectrometry analysis of the dissolved Fe^{2+} from the electrodes before and after electrochemical tests. These results indicated that PB dissolved after tests under different pHs and repeated cyclic voltammetry scans, whereas NiHCF did not show any substantial degradation and maintained the highest stability among the transition metal hexacyanoferrates for PB stabilization.

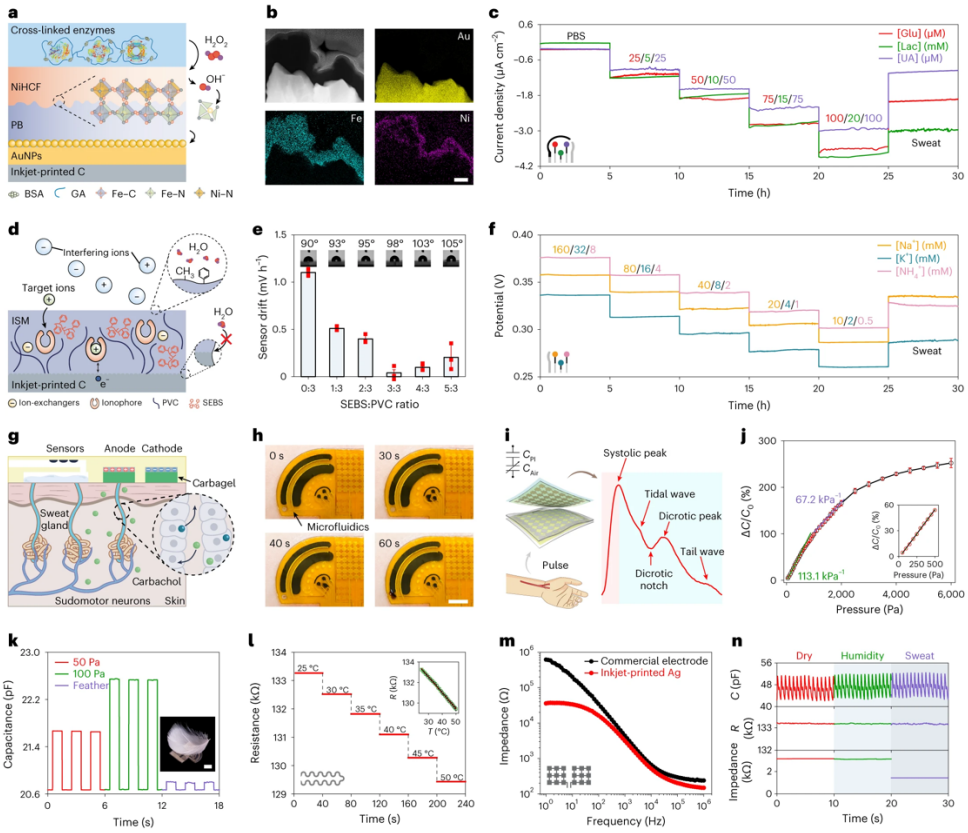

Figure 5.12 Design and characterization of highly robust multimodal sensors. A) Mechanism of enzymatic metabolite sensors. B) Cross-sectional STEM and EDS images of the PB–NiHCF interface. Scale bar, 100 nm. C) Operational long-term stability of enzymatic glucose, lactate and UA sensors in PBS and sweat samples for 30 h. D) Mechanism of ISEs. e, SEBS to PVC ratios in regard to sensor stability. Insets, contact angle measurements for different SEBS ratios. Data are presented as mean ± s.d. (n = 3 sensors). F) Operational long-term stability of ion-selective Na+, K+ and NH4+ sensors in standard solutions and sweat samples for 30 h. (G, H) Schematic (G) and on-body evaluation (H) of the microfluidic IP module for autonomous sweat induction and sampling at rest. Timestamps in h represent the period after a 5 min IP session. I). Schematic of the pressure sensor and a pulse waveform measured at the wrist. CPI, capacitance of the polyimide; CAir, capacitance of the airgap. J). Pressure versus capacitance (C)

characterizations of the pressure sensor, where C0 is flat-state C. Data are presented as mean ± s.d. (n = 3 sensors). K) Repetitive response of the pressure sensor on small pressure loads. Inset, a goose feather placed on a sensor. Scale bar, 1 cm. L) Response of the temperature (T) sensor in the physiological temperature range. m, Impedance of the skin–electrode interface measured with inkjet-printed Ag electrodes and commercial electrodes for GSR monitoring. N) Performance of encapsulated pulse, T and GSR sensors under environmental humidity and body sweat test. All error bars represent the s.d. from three sensors. AuNPs, gold nanoparticles; carbagel, carbachol hydrogel; GA, glutaraldehyde; Glu, glucose; Lac, lactate; ISM, ion-selective membrane; R, resistance.

Highly stable, continuous and selective monitoring of sweat glucose, lactate, and UA was realized amperometrically, and a linear response between current output and target concentrations was obtained for all three sensors in physiologically relevant concentration ranges over a 25 h evaluation period (**Fig. 5.2C**). The sensitivities for glucose, lactate, and UA sensors were 33.65 nA μM−1 cm−2, 185.56 nA mM−1 cm−2 and 26.36 nA μM−1 cm−2, respectively. These sensors also showed long-term stability of more than 100 h of continuous operation in phosphate-buffered saline (PBS) solutions and untreated human sweat samples, which greatly exceeded that obtained with previous widely adopted wearable sweat sensors. Note that as sweat lactate is present in high concentrations (up to 60 mM), a further diffusion-limited polyvinyl chloride (PVC)/bis(2-ethylhexyl) sebacate (DOS) membrane was introduced on top of the enzyme film to achieve a wide linear range while maintaining high sensor stability.

Existing wearable ISEs are based on PVC/DOS membranes and are plagued with a potential drift of typically ~2 mV per hour over time, which is attributed to ionophore leaching and water formation below the ion-selective membrane[31]. To address this issue during long-term operation, we adopted another analogous composite materials design strategy by introducing polystyrene-block-poly (ethylene butylene)-block-polystyrene (SEBS) into the PVC system; it shares a similar long-chain structure but holds more methyl and phenyl groups at the sensor interface to promote hydrophobicity and mechanical strength (**Fig. 5.2D**). High hydrophobicity suppresses ionophore leaching and prevents water layer formation at the interface. To fabricate ISEs, electrodes made from inkjet-printed carbon nanoparticles, which are inert but have a large surface area, were used without the need to deposit further ion-charge transducer materials. Ion-selective membranes, based on the PVC–SEBS matrix, were drop-casted onto the carbon electrode, and the SEBS to PVC ratio was evaluated to identify the optimal stability (**Fig. 5.2E**). The optimized ISEs obtained prolonged stability of 100 h of continuous operation in both standard solutions and human sweat samples, with the potential value decaying less than 0.04 mV per hour. A logarithmic–linear relationship between the potentiometric output of Na+, K+, and NH4+ with near-Nernstian sensitivities of 58.9, 60.6, and 61.2 mV per decade, respectively, were identified during a 25 h prolonged sensor evaluation in physiologically relevant ranges (**Fig. 5.2F**).

With an analogous composite materials' approach, our sensors demonstrated high reproducibility, selectivity and long-term continuous operation stability in both standard solutions and untreated human sweat over several days. Such sensor performance, to the best of our knowledge, was among the best in wearable sweat sensing. The low-cost, mass-producible sensor patch is designed to be disposable after use: the anticipated wearable use time for each patch is 24–48 h, and users can easily replace the sensor patch. Thus, our sensors can provide a stable response for longer than the expected wearable use time. The general material strategy demonstrated here, based on electrodes prepared by inkjet printing, can be applicable to electrodes manufactured using other scalable technologies, including laser engraving and thin-film evaporation. In addition, the sensor preparation approach here is not limited to the six sensors we proposed in this study; it can serve as a universal and readily reconfigurable method for other enzymatic and ionophore-based biosensors towards a broad range of practical applications.

To realize practical molecular biomarker monitoring without the need for vigorous exercise, miniaturized IP electrodes coated with carbachol hydrogels were incorporated into the CARES for autonomous, local sweat induction (**Fig. 5.2G**). Sweat can be continuously secreted from the surrounding glands over a prolonged period because of the nicotinic effects of carbachol (transdermally delivered for 5 min by means of a 50 μA current). Efficient sampling was

obtained through custom-developed microfluidics for real-time bioanalysis with high temporal resolution (**Fig. 5.2H**).

In addition to chemical sensors, the CARES also contains several physical sensors to monitor stress-related vital signs. We placed a capacitive pressure sensor above the radial artery for pulse waveform monitoring (**Fig. 5.2I**). Because of the soft PDMS-engraved airgap, the pressure sensor is highly sensitive to soft pressure loads (such as a feather), with an impressive sensitivity of 113.1% kPa−1 in the range of 0 to 500 Pa (**Fig. 5.2J–K**). The pressure sensor also displays highly robust performance and mechanical stability during a repetitive pressure-loading test involving 5,000 cycles, mimicking daily use on the skin. A printed resistive temperature sensor was integrated into the CARES for skin temperature recording in situ, with a sensitivity of around 0.115% °C−1 in physiological temperature ranges between 25 and 50 °C (**Fig. 5.2L**). Considering that temperature has a strong influence on enzymatic activities, the temperature information is used for calibrating the response of the three enzymatic biosensors to achieve highly accurate in situ metabolic analysis. Note that other environmental factors such as humidity showed minimal influence on the performance of our chemical sensors. Additionally, a pair of printed Ag electrodes was used as a GSR sensor, which demonstrated high conductivity compared with commercial gel electrodes (**Fig. 5.2M**). Because of the ultrathin flexible PI substrate and strong interfacial strength enabled by the medical adhesive, the CARES showed excellent skin contact and mechanical resilience

against undesirable physical deformations during continuous operations. The impermeable PI packaging also eliminated the influence of humidity from environmental surroundings and sweat (**Fig. 5.2N**).

5.2.2 Continuous daily monitoring across various activities

Because of the excellent long-term stability of wearable sweat biosensors, the CARES enables long-term real-time continuous monitoring of physicochemical biomarkers. As illustrated in (**Fig. 5.3A**), the CARES can successfully record dynamic changes in metabolites and vital signs over 24 h of activity involving casual and vigorous exercise, dietary intake, lab work, relaxing entertainment, and sleep. Glucose and UA levels spiked after food intake, indicating rapidly increased metabolic activities. During vigorous exercise, substantial increases in vascular activity and skin electrolyte/conductivity were observed, and stable output for both metabolites and vital signs was detected during sleep at night. Such powerful capabilities of continuous multimodal monitoring will enable various personalized healthcare and human performance monitoring applications.

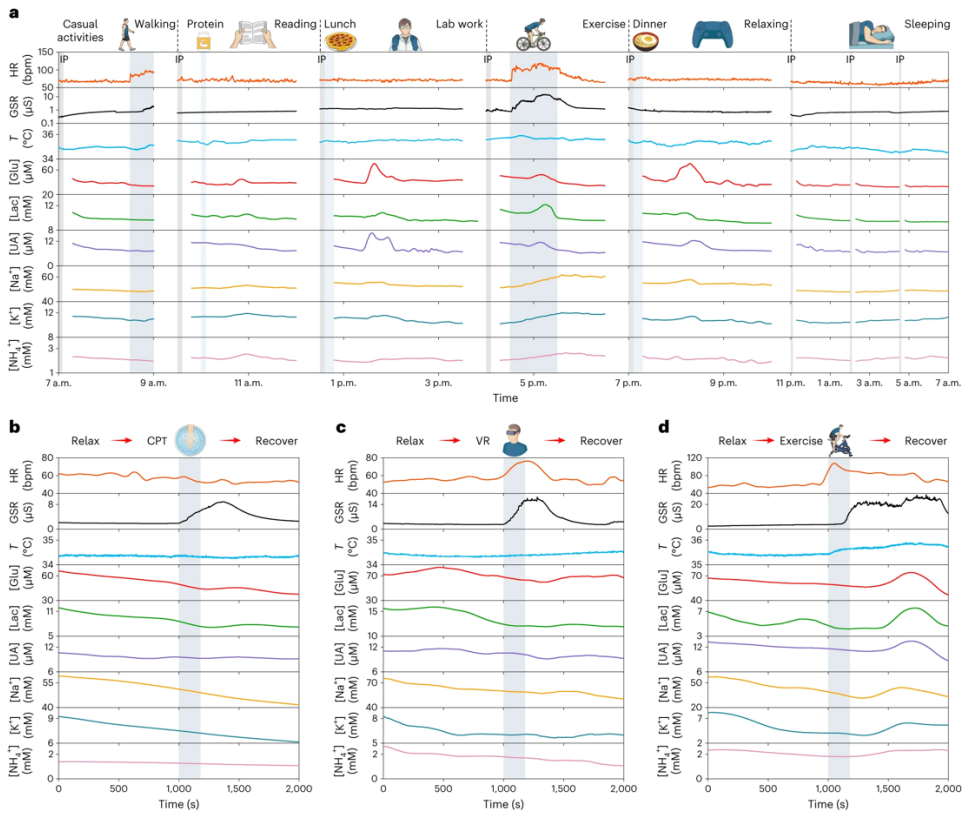

Figure 5.13 On-body evaluation of the CARES platform. A) Continuous 24 h multimodal monitoring during a subject's daily activities. (B–D), Multimodal monitoring of a selected subject's stress response under three different stressors: a CPT challenge, during which the subject was asked to immerse one hand in ice water (B); a VR challenge, during which the subject was asked to play a VR rhythm game (C); and a cycling exercise test, during which the subject was asked to perform a maximum-load cycling challenge on a stationary exercise bike (D). HR, heart rate; bpm, beats per minute.

5.2.3 ML approach for stress evaluation

To evaluate the use of the CARES for stress response monitoring, controlled experiments were performed on ten healthy subjects using three different physiological and psychological stressors: a cold pressor test (CPT), a virtual

reality (VR) challenge and intense exercise. The dynamic profiles of all individual sensors integrated in the CARES were collected during each study (**Fig. 5.3B–D**). State anxiety levels, as measured by the State-Trait Anxiety Inventory Form Y (STAI-Y) questionnaire, with scores ranging between 10 and 40 points (10 indicating little to no anxiety), were the psychological stress response measure for data training. The questionnaire was administered before and after each stressor to quantify the induced anxiety levels in a subject.

For each experiment, on-body chemical and physical data showed notable variations in response to each stressor. During the CPT experiment, subjects immersed one hand in ice water for 3 min. A natural reaction of vasoconstriction occurred, and the blood vessel constricted in response to cold temperatures. As a result, immediate physiological responses including altered pulse waveform and elevated GSR were observed, consistent with previous reports on the variations of physiological signals with cold-stimulated stress response. In addition, delayed mild fluctuations in metabolite concentrations of glucose, lactate, and UA in some subjects were also observed. During the VR test, subjects wore an Oculus VR headset to play a rhythm game (Beat Saber) while the gaming screen was mirrored to a computer monitor with an audience, resulting in both physiological and social–evaluative psychological stress. We observed substantial differences in the pulse waveform and GSR amplitude during and after the stress stimulus, along with elevated glucose, lactate, and UA levels minutes later. During vigorous exercise, profound activation of the HPA axis led to dramatic changes

of all physiological signals as well as sweat metabolites and electrolytes (for example, Na+), in agreement with previous studies on exercise-induced stress response. These results indicate that the CARES can reliably monitor stress-induced biological signals.

To quantify the stress-response-related features, data-driven stress and anxiety evaluations were performed after each experiment was complete: an ML pipeline was developed to extract features and deconvolute connections between physicochemical information and stressor types and state anxiety levels (**Fig. 5.4A**). We undertook this challenge using three separate ML analyses: stress detection versus relaxation, stressor classification, and anxiety level evaluation, where we trained and tested each model across three experiments (VR, CPT, exercise) with all ten subjects for a total of 60,000s of physiological CARES signals. All signals were calibrated and normalized to ensure that the features extracted after data preprocessing were stable against patch variations and any moderate motion artifacts. Feature extraction was validated before ML analysis by projecting the multidimensional feature space into 2D space by means of t-distributed stochastic neighbor embedding, where data from stress/relaxation naturally formed distinctive clusters, indicating the discriminative power of the features (**Fig. 5.4B**).

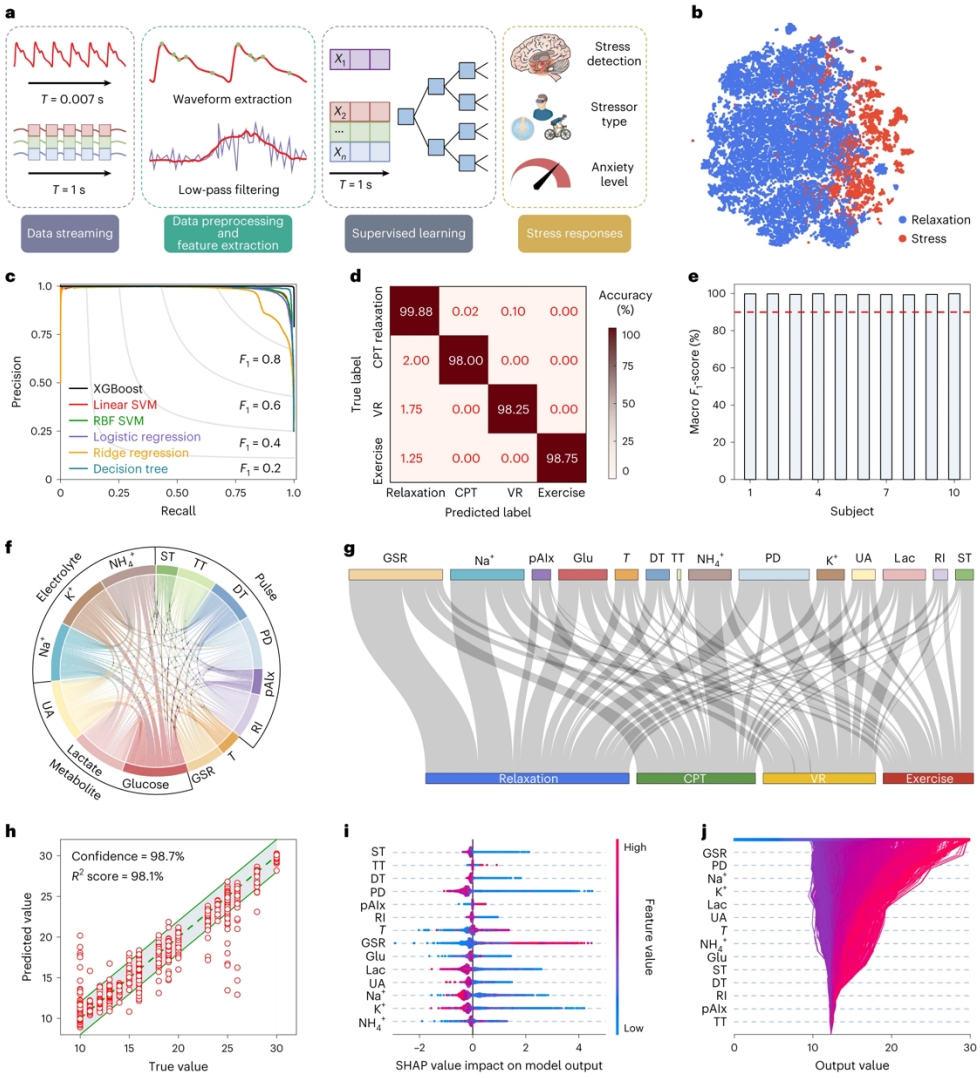

Figure 5.14 Machine learning analysis of stress response assessment. A) Schematics of the ML architecture for data preprocessing, feature extraction, supervised learning and evaluation. B) t-distributed stochastic neighbor embedding plot from the dataset recorded by the CARES, visually showing feature separation in a two-dimensional space. C) Precision–recall curve of different ML models for stressor classification. D) Confusion matrix displaying the classification accuracy for predicting each type of stressor in test set. E) The overall stress classification accuracy based on macro-averaged F1-score for each subject. F) Chord diagram showing the relative correlation between different sensors. G) Sankey diagram of

SHAP analysis depicting the relative contribution of different sensors to stressor classification. H) True versus ML-predicted state anxiety scores. Data are presented as ±2 state anxiety score buffer based on the potential error in the anxiety questionnaires. I) SHAP summary plot for state anxiety level evaluation based on the dataset collected by the CARES. Each axis plots the distribution of SHAP values of a given feature for each prediction instance. J) SHAP decision plot explaining how the ML model determines the state anxiety level using both physiological and biochemical features. DT, dicrotic peak time; PD, pulse duration; pAIx, peripheral augmentation index; RBF, radial basis function; RI, reflection index; ST, systolic time; TT, tidal peak time.

Different ML models were evaluated, and the trained boosting decision tree model Extreme Gradient Boosting (XGBoost) outperformed typical ML models, including linear and radial basis function support vector machines (SVMs), logistic and ridge regression and conventional decision trees (**Fig. 5.4C**). Combined with features extracted from both physiological and metabolic data, it was found that our XGBoost ML model could yield much higher accuracy, with stress response classification accuracy of 99.2% for stress/relaxation detection and an accuracy of more than 98.0% for stressor classification, which to the best of our knowledge is the highest accuracy reported for stressor classification (**Fig. 5.4D**). Note that differentiating stressors has high importance, as each stressor carries varying physiological and psychological influences and could act as a risk factor for coping responses and cardiovascular diseases[32–34]. Distinguishing types of stressors has been recognized as a necessary condition for understanding the complex interrelationships among distinct stress experiences, as well as the collective effects of stress on mental health. Moreover, the XGBoost ML model

resulted in highly consistent overall accuracies of more than 99.3% across different individuals (**Fig. 5.4E**).

The Pearson correlation coefficients between all sensors in the CARES show the interrelatedness between physiological and chemical biomarkers (**Fig. 5.4F**). The relatively homogeneous correlation shows the high independence of the extracted features. To evaluate each physicochemical sensor's contribution to the model, feature importance of each biomarker towards each stressor was evaluated using a Shapley additive explanation (SHAP) (**Fig. 5.4G**). Through SHAP analysis, the feature importance of GSR, pulse, glucose, and Na+ indicates that these biomarkers play an important role in stressor classification. These results support the fact that stress responses involve participants' vascular dynamics, neural stimulation, and metabolism.

In terms of the classification results, we expanded our analysis to the evaluation of state anxiety levels. We adopted a similar XGBoost regression model and could predict state anxiety levels with a high confidence level of 98.7% and 98.1% coefficient of determination of scores from the STAI-Y1 (with a s.d. of 4 points or less48) (**Fig. 5.4H**). The relevance of each feature was evaluated using SHAP analysis as well (**Fig. 5.4I–J**). Through SHAP analysis, it was determined that GSR, pulse, Na+, K+, and lactate played the most important roles in predicting state anxiety levels. Note that SHAP values show the relative importance of each feature in the ML model. Additionally, given the intrinsic

limitations of questionnaires, which can only characterize state anxiety levels in each period rather than continuous dynamic stress change, we analyzed the stress response event to mimic questionnaire functionalities. In this circumstance, features were extracted from the stress region by taking mean signal changes from the moving average (MA) of sensor data rather than segmented at each timepoint, and a simple linear regression model was trained with fewer features selected to correspond to questionnaire scores and prevent overfitting. With the reduced size of the dataset and analyzing the overall sensor responses in the CARES, we performed a brute-force feature selection in each biomarker and found that combined physicochemical features outperformed those of physical and chemical sensors alone.

To realize convenient data collection for real-life applications, in addition to using flexible cables connecting the CARES patch with laboratory instruments, we further designed a fully integrated wearable CARES system with a flexible printed circuit board for multiplexed and multimodal signal processing as well as Bluetooth wireless communication. The wireless system was successfully used for on-body tests and validation of our CARES systems in the laboratory setting and in real-life daily casual activities. Our ML models obtained from the laboratory tests were able to accurately classify the types of stressors and state anxiety levels based on the wirelessly collected sensor data in the laboratory as well as real-life settings. We anticipate that for large-scale human trials, the CARES will surpass the current gold standards for stress response quantification

and provide a highly robust stress response monitoring tool that is not reliant on subjective reporting with its potential for errors. In this regard, we envision a high potential for wearable multimodal physicochemical monitoring of dynamic stress response.

5.3 Methods

5.3.1 Materials

SEBS (Tuftec) was provided by the Asahi Kasei Corporation. UA, sodium tetraphenylborate, and glutaraldehyde (25% aqueous solution) were purchased from Alfa Aesar. Agarose, carbachol, BSA, gold chloride trihydrate, hydrochloric acid, iron(III) chloride, potassium ferricyanide (III), potassium ferrocyanide (IV), PVC, polyvinyl butyral (PVB), DOS, 3,4-ethylenedioxythiophene, poly(sodium 4-styrenesulfonate), aniline, l-lactic acid, sodium ionophore X, sodium tetrakis[3,5-bis(trifluoromethyl) phenyl] borate, valinomycin, nonactin, tetrahydrofuran (THF), toluene, glucose oxidase from Aspergillus niger (216 U mg−1), and uricase from Bacillus fastidiosus (15.6 U mg−1) were purchased from Sigma-Aldrich. Methanol, ethanol, sodium chloride, potassium chloride, nickel chloride, urea, l-ascorbic acid, dextrose (d-glucose) anhydrous, and PBS were purchased from Thermo Fisher Scientific. Lactate oxidase (106 U mg−1) was purchased from Toyobo Co. Medical tapes (M-tapes) were purchased from 3M (468 MP). Polyethylene terephthalate (PET) films (12 μm thick) were purchased from McMaster-Carr. PI (2611) was purchased from HD MicroSystems, Inc. PDMS (SYLGARD 184) was purchased

from Dow Corning. PI film (12.5 μm) was purchased from DuPont. STAI questionnaire license was purchased from Mind Garden, Inc.

The morphology of materials was characterized by field-emission scanning electron microscopy (Nova 600). Cross-sectional lamella was prepared by standard focus ion beam cutting (Nova 600). The STEM characterizations and EDS analyses were performed using a JEOL JEM-ARM300CF S/STEM system (300 keV).

5.3.2 Fabrication and assembly of the CARES device

PI was spin-coated on the silicon oxide wafer at a speed of 5,000 revolutions per minute (r.p.m.) for 30 s and then cured at 350 °C for 1 h with a ramping speed of 4 °C min−1. The resulting PI substrate thickness is about 4 μm. For mass fabrication, 12.5 μm PI film was used for large-area patterning demonstration. The CARES patch was then patterned with sequential printing of silver (interconnects and pin connections, reference electrode, pulse sensor, and GSR sensor), carbon (IP electrodes, counter electrode, temperature sensor, and working electrodes for biosensors), and PI (encapsulation) using an inkjet printer (DMP-2850, Fujifilm). The CARES patch was then annealed at 250 °C for 1 h. A 1:12 mixture of curing agent to PDMS elastomer was prepared and stirred thoroughly for 10 min, after which the solution was spin-coated at a speed of 800 r.p.m. for 30 s directly onto the inkjet-printed bottom layer of the CARES patch, followed by curing at 60 °C for 1 h. The resulting PDMS thickness is about

120 μm. Both the bottom and top layers of the CARES patch were then laser patterned to define outlines and sweat outlets using a 50 W CO2 laser cutter (Universal Laser System) with power 25%, speed 50% and pulse per inch (PPI) 1,000 in vector mode. The bottom layer was further cut to define IP reservoirs, sweat reservoirs and airgaps without cutting through the PI substrate, with optimized parameters of power 2%, speed 20%, PPI 500 in vector mode, twice. The PDMS layer was cleaned with ethanol and deionized water to remove debris, followed by 30 s of O2 plasma surface treatment using Plasma Etch PE-25 (10 cm^3 min^{-1} O2, 100 W, 150 mTorr) to clean its surface and promote surface adhesion. The entire CARES patch was then assembled by dry transferring the top layer onto the bottom layer using a PDMS stamp. Biosensors were prepared before microfluidics integration. Note that the sweat reservoir was predefined during fabrication of the 120-μm-thick PDMS middle layer of the CARES patch, which has dimensions of 17.15 mm2 and therefore a reservoir volume of 2.06 μl. The small volume allows a fast refreshing rate and enables rapid detection of dynamic changes during human performance.

The microfluidics layers were fabricated with a laser cutter, layer by layer, by patterning double-sided M-tape, PET and PDMS with IP gel reservoirs, gel electrolytes reservoirs, sweat inlets, flowing channels, and outlets. The optimized laser parameters to cut M-tape were set to power 62%, speed 100%, PPI 500 in vector mode, twice; and the optimized parameters to cut PDMS were power 2%, speed 20%, PPI 500 in vector mode, twice, to minimize debris. The IP gel and

gel electrolytes reservoirs were patterned by cutting through all microfluidics layers to define the gel area and establish a gel connection with the skin. The first microfluidics layer is a PDMS-based sweat channel layer, which was spin-coated on a PET petri dish and cured at 60 °C for 1 h. The PDMS layer was treated with O2 plasma before laminating a thin layer of 12 μm PET, followed by laser-defining sweat inlets. Then the third layer of double-sided M-tape was patterned and aligned onto PET, which contacts the skin and forms the sweat accumulation layer. After attaching the microfluidics module to the CARES patch, the system was further encapsulated with PDMS backings to avoid potential sweat contact and leakage. The device was connected with a flexible printed circuit connector for further characterization.

Both the anode and cathode of IP gel were prepared by mixing agarose (3% w/w) into deionized water and then heated to 250 °C under constant stirring until the solution became homogenous. The solution was then cooled to 165 °C, during which 1% w/w carbachol and 1% w/w NaCl were added to the anode and cathode solutions, respectively, and mixed thoroughly. The solution was further cooled and poured into the IP gel reservoirs: 41.95 mm2 for the anode and 28.19 mm2 for the cathode, respectively. Together with the IP gel, electrolyte gel (SignaGel, Parker Laboratories, Inc.) was cast onto the GSR electrodes before the CARES device was placed on human subjects.

On-body flow tests were conducted to evaluate the sweat flow of dual-reservoir designs. An assembled microfluidic patch predeposited with black dye in the sweat reservoir was attached to a subject's forearm, followed by in situ sweat induction using IP.

Experimental flow tests were also conducted to evaluate the dynamic response of sensors using a syringe pump (78–01001, Thermo Fisher Scientific). Different fluids were injected into the pre-assembled CARES device with a varying flow rate of 1–4 μl min−1.

5.3.3 Biosensor preparation and characterization

An electrochemical workstation (CHI 760E, CH Instruments) was used to prepare enzymatic biosensors. Pulsed voltammetry from −0.9 to 0.9 V (3,000 cycles total) in 50 mM HAuCl4 was used to deposit gold nanoparticles on the carbon electrode at a signal frequency of 50 Hz, to increase surface area and enhance sensitivity. A thin PB transducer layer was deposited by applying cyclic voltammetry for two cycles for glucose and UA and four cycles for lactate (from −0.2 to 0.6 V with a scan rate of 50 mV s−1) in a fresh solution consisting of 2.5 mM FeCl3, 2.5 mM K3Fe(CN)6, 100 mM KCl, and 100 mM HCl. The electrodes were then deposited with a NiHCF protection layer by applying cyclic voltammetry for 50 cycles (from 0 to 0.8 V with a scan rate of 100 mV s−1) in a fresh solution containing 0.5 mM NiCl2, 0.5 mM K3Fe(CN)6, 100 mM KCl, and 100 mM HCl. The electrodes were then dried before drop-casting with an enzyme

cocktail. For all three amperometric enzymatic sensors, the enzyme cocktails were prepared as follows: BSA (1% w/w), 2.5% glutaraldehyde (2% v/v), and 10 mg ml−1 enzyme (4% v/v) were mixed in 1 ml PBS. Then 0.5 µl of enzyme cocktail was drop-casted onto each enzymatic sensor electrode surface and dried overnight at 4 °C. For the lactate sensor, a limit-diffusion membrane was further drop-casted by applying 0.5 µl of a solution containing 17 mg PVC and 65 mg DOS in 660 µl THF.

To prepare the shared reference electrode, 10 µl of 0.1 M FeCl3 solution was drop-casted onto the Ag surface for 20 s and rinsed with deionized water. Then 1.5 µl PVB reference cocktail was applied on the Ag/AgCl surface by dissolving 79.1 mg PVB and 50 mg NaCl into 1 ml methanol and left to dry overnight.

The Na+ selective cocktail was prepared as follows: 1 mg Na ionophore X, 0.55 mg sodium tetrakis[3,5-bis(trifluoromethyl) phenyl] borate, 30 mg PVC, 30 mg SEBS, and 65 mg DOS were dissolved in 660 µl THF. The K+ selective cocktail was prepared as follows: 2 mg valinomycin, 0.5 mg sodium tetraphenylborate, 30 mg PVC, 25 mg SEBS, and 70 mg DOS were dissolved in 350 µl THF. The NH4+ selective cocktail was prepared as follows: 1 mg nonactin, 30 mg PVC, 30 mg SEBS, and 65 mg DOS were dissolved in 660 µl THF. The inkjet carbon electrode was activated in 0.5 M HCl with cyclic voltammetry scans of ten cycles (−0.1 to 0.9 V with a scan rate of 100 mV s−1). The electrodes were baked in a vacuum oven at 120 °C for 1 h to remove

moisture. Then 2 µl Na+ selective cocktail, 2 µl K+ selective cocktail and 2 µl NH4+ selective cocktail were drop-casted onto the carbon electrode and dried overnight.

To obtain the best performance for long-term continuous measurements, all sensors were placed in a buffered solution containing 100 µM glucose, 5 mM lactate, 25 µM UA, 40 mM NaCl, 8 mM KCl, and 2 mM NH4Cl for 30 min to minimize potential drift. All the in vitro biosensor characterizations were performed with cyclic voltammetry and amperometry through a multichannel electrochemical workstation (CHI 1430, CH Instruments). For in vitro enzymatic sensor characterizations, analyte solutions were prepared in PBS, with glucose ranging from 0 to 100 µM, lactate ranging from 0 to 20 mM and UA ranging from 0 to 100 µM. For in vitro ISE sensor characterizations, analyte solutions were prepared in deionized water, with NaCl ranging from 10 to 160 mM, KCl ranging from 2 to 32 mM and NH4Cl ranging from 0.5 to 8 mM. The enzymatic sensors were characterized chronoamperometrically at a potential of 0 V, and the ISE sensors were characterized using open circuit potential measurement. Both potentiometric and chronoamperometric responses were set to a 1 s sampling interval, except for long-term monitoring, where the sampling interval was set to 10s to minimize data overload. To test the pH influence on PB–NiHCF-based enzymatic biosensors, McIlvaine buffer solutions were prepared and calibrated containing 0–100 µM H2O2. Temperature influence characterizations were carried out on a ceramic hot plate (Thermo Fisher Scientific).

To characterize the stability of the PB and PB–NiHCF electrodes, dissolved Fe2+ concentrations were determined by inductively coupled plasma–mass spectrometry using an Agilent 8800. The sample introduction system consisted of a micromist nebulizer, Scott-type spray chamber, and fixed-injector quartz torch. A guard electrode was used, and the plasma was operated at 1,500 W. All elements were measured in Helium tandem mass spectrometry mode.

For in vitro temperature and GSR sensor characterizations, an amperometric method was used with an applied voltage of 1 V using a dual-channel electrochemical workstation (CHI 760E).

For in vitro pulse sensor characterizations, a parameter analyser (Keithley 4200A-SCS) was applied to record the fast-changing capacitive signals at a sampling frequency of around 137 Hz. The influence of mechanical deformation on physical sensor performance was investigated through pressing-releasing for 5,000 cycles using a Mark-10 force gauge. The influence of humidity was investigated by immersing the subject hand with the CARES in a customized glove box with a humidity gauge.

5.3.4 On-body evaluation for long-term continuous monitoring

The validation and evaluation of the CARES device were performed on healthy human subjects in compliance with the protocols (19–0892 and 19–0895) approved by the Institutional Review Board at the California Institute of Technology (Caltech). Participating subjects were recruited from the Caltech

campus and neighbouring communities through advertisement by posted notices, word of mouth, and email distribution. Ten healthy subjects (eight males and two females, age range 23–38 years) were included in this study. The participants were healthy, without anxiety or depression issues. All subjects gave written informed consent before participation in the study. The study was fully voluntary, and no compensation was given.

The CARES was mounted on the subject's wrist after skin cleaning with alcohol wipes. Participants were requested to refrain from meals, alcohol, caffeine, and exercise within 3 h before the tests. The CARES was sealed in PDMS, leaving output pins exposed with an M-tape backing as support for wire connections. We further designed a plug-and-play input–output to connect with the flexible flat cable. A 50 μA current was implemented on both pairs of IP electrodes for 5 min simultaneously for sweat induction. The data were collected with an eight-channel multiplexer (CHI Instrument 1430) and a Keithley 4200A-SCS parameter analyser. A wireless wearable CARES system was also developed for convenient data collection in real-life settings.

Continuous monitoring of 24 h of physiological and biochemical signals was recorded using the CARES device. Five-minute periodical IP sweat induction was performed at 7 a.m., 9:30 a.m., 12:30 p.m., 4 p.m., 7 p.m., 11 p.m., 1:30 a.m., and 4:30 a.m. The physiological data were collected continuously, and data from the biosensors were collected 10 min after IP.

STAI is a self-evaluation questionnaire that consists of two forms (Y1 and Y2) to measure state and trait anxiety, respectively. It has a high internal consistency coefficient of 0.91–0.93 for college students and working adults. In our study, we used short form Y1, which measures state anxiety, as a key psychological response to stress. This measure can be proctored during real-time experiments without major intervention during the stress event. One challenge for quantifying stress is the subjective nature of the questionnaire, which inherently leads to small fluctuations of various stress points, with a s.d. of more than four points in most cases. In our study, we take ±2 points as the confidence interval buffer for state anxiety level evaluation.

During CPT, the participants were asked to wear the CARES and relax for 10 min after IP sweat induction, during which no sensor signals were collected. After the relaxing stage, the physical sensors and biosensors simultaneously started monitoring baseline vital and molecular data. The STAI-Y1 questionnaire was administered to assess state anxiety levels during this relaxed baseline state. Subjects were asked to relaxation for another 1,000 s, after which a 3 min CPT was conducted. Subjects were asked to immerse their other hand without the CARES device up to the forearm into a tank containing iced water (0 °C) for 3 min. Another STAI-Y1 questionnaire was then given to evaluate state anxiety levels, and subjects were asked to finish within 20 s. Afterwards, subjects were instructed to remove the hand from the iced water and recover in ambient air. Continuous monitoring of multimodal physiological and biochemical data was

performed throughout the stress challenge and recovery stage until 1,000 s after the CPT was finished. The subjects were seated during the whole procedure.

During VR, the sensor data recording process was the same as the aforementioned, except that subjects were asked to play a VR game (Beat Saber) while wearing a VR headset (Oculus Quest 2, Meta). The game was set to one-handed mode with expert difficulty, and the game screen was projected onto a monitor. Subjects were strongly encouraged verbally and asked to compete with other participants' record scores so that mixed physical and psychological stress could be stimulated. The STAI-Y1 questionnaire was used to assess state anxiety levels.

During exercise, the sensor data recording process was the same as the aforementioned. Subjects performed maximum-load cycling (>70 r.p.m.) on a stationary exercise bike (Kettler Axos Cycle M-LA) for 3 min or until fatigue, during which strong verbal encouragement was given. The STAI-Y1 questionnaire was used to assess state anxiety levels.

For data collection in real-life activities, subjects were asked to perform indoor activities, including relaxation on the phone, playing a long-term VR game (Superhot VR) while wearing a VR headset and reading journal papers. Subjects then performed outdoor activities, including running and walking recovery. The STAI-Y1 questionnaire was used to assess state anxiety levels during each activity.

5.3.5 Machine learning pipeline for stress assessment

Although all the multimodal sensor signals were monitored in real time, data preprocessing was performed asynchronously to extract features. A pulse feature extraction algorithm was developed because of its unique peripheral pulse sampling frequency of $T = 0.007$ s. To match the other sensors' sampling frequency of $T = 1$ s, each pulse waveform was autonomously analysed through our pulse analysis algorithm, and a floor function was used afterwards to select the closest pulse feature within each time interval. Signals from the biochemical sensors were manually shifted by 300 s to align with physical signals due to natural sweat delay; heart rate data in figure plots were extracted from the pulse features and smoothed by the MA of 100 s to show the trends more clearly. The time stamp when each subject expressed stress was recorded, and manual data labelling was performed. To minimize variations from intersubject responses, all features were normalized before the ML pipeline with regard to each subject during each stress test, to generalize the model among the population. After data collection and analysis, the training and testing datasets were shuffled and divided 8:2, respectively, and data points were randomly selected using an equal representation of each class. The ML model was developed to link biological and chemical features to stress detection, stress types, and state anxiety levels from questionnaire scores.

All training models were built using Python (v.3.8) based on the data collected from ten subjects facing three different stressors, with a set of 60,000 s of CARES

recordings. Segmentation of the sensor signals was done using a sliding window with a sampling interval of 1 s, given each stress type representation. Several ML models were evaluated according to their precision–recall curves and F1-scores, including linear and radial basis function SVMs, logistic and ridge regression, conventional decision trees, and the gradient-boosted decision tree XGBoost model. The trained XGBoost model outperformed typical ML models for both stress detection and stress type classification.

The ML algorithms were developed on a password-protected local computer with individual graphics processing unit module Nvidia 3080. The training models were built as mentioned earlier, except that the kernel was changed to a regressor instead of a classifier. For overall stress level evaluations, on the other hand, features were extracted from stress regions by taking average signal changes from the MA of sensors rather than segmented at each timepoint, and simpler ML models such as linear regression and SVM were evaluated because of the reduced size of the datasets, to prevent overfitting. A brute-force examination of features was performed to compare the contributions of physicochemical biomarkers.

5.4 Conclusion

We have reported a CARES platform that performs multiplexed monitoring of key physiological signals, metabolites and electrolytes simultaneously during a prolonged operation. By applying analogous composite materials for stabilizing and conserving sensor interfaces, we developed a general approach to prepare

stable and sensitive biochemical sensors including both enzymatic and ISE sensors, which offer long-term stability of more than 100h of continuous operation with negligible sensor degradation. Continuous 24h monitoring of prolonged daily activities was also obtained. Real-time multimodal data for stress responses were generated from three different stressors using both biochemical and physiological signals. With the enhanced reliability of sensor readings, we showed that a state of stress versus relaxation, and state anxiety as a key psychological response to stress, can be classified and predicted through multimodal health profiles at the metabolic level, with the ability to detect and classify stressor types with an accuracy of more than 98.0% and evaluate state anxiety levels at a confidence level of 98.7%. By capturing a broader range of signals through more integrated biosensors, a more complete metabolic profile could be achieved for next-generation healthcare and human performance monitoring. Our CARES could be of use in the development of numerous practical wearable applications including intelligent healthcare and personalized medicine.

References

1. Schneiderman, N., Ironson, G. & Siegel, S. D. Stress and Health: Psychological, Behavioral, and Biological Determinants. *Annual Review of Clinical Psychology* **1**, 607–628 (2005).
2. Kivimäki, M., Bartolomucci, A. & Kawachi, I. The multiple roles of life stress in metabolic disorders. *Nat Rev Endocrinol* **19**, 10–27 (2023).
3. Podsakoff, N. P., Freiburger, K. J., Podsakoff, P. M. & Rosen, C. C. Laying the Foundation for the Challenge–Hindrance Stressor Framework 2.0. *Annual Review of Organizational Psychology and Organizational Behavior* **10**, 165–199 (2023).
4. Pfefferbaum, B. & North, C. S. Mental Health and the Covid-19 Pandemic. *New England Journal of Medicine* **383**, 510–512 (2020).
5. Gutshall, C. L., Hampton Jr.,David P., Sebetan ,Ismail M., Stein ,Paul C. & and Broxtermann, T. J. The effects of occupational stress on cognitive performance in police officers. *Police Practice and Research* **18**, 463–477 (2017).
6. Haines, M. M., Stansfeld, S. A., Job, R. F. S., Berglund, B. & Head, J. Chronic aircraft noise exposure, stress responses, mental health and cognitive performance in school children. *Psychological Medicine* **31**, 265–277 (2001).
7. Kulshreshtha, A. *et al.* Association of Stress With Cognitive Function Among Older Black and White US Adults. *JAMA Network Open* **6**, e231860 (2023).
8. Drew, D. A. *et al.* Rapid implementation of mobile technology for real-time epidemiology of COVID-19. *Science* **368**, 1362–1367 (2020).
9. Charmandari, E., Tsigos, C. & Chrousos, G. ENDOCRINOLOGY OF THE STRESS RESPONSE1. *Annual Review of Physiology* **67**, 259–284 (2005).
10. Dolan, R. J. Emotion, Cognition, and Behavior. *Science* **298**, 1191–1194 (2002).
11. Acosta, J. N., Falcone, G. J., Rajpurkar, P. & Topol, E. J. Multimodal biomedical AI. *Nat Med* **28**, 1773–1784 (2022).
12. Axelrod, J. & Reisine, T. D. Stress Hormones: Their Interaction and Regulation. *Science* **224**, 452–459 (1984).
13. Buergel, T. *et al.* Metabolomic profiles predict individual multidisease outcomes. *Nat Med* **28**, 2309–2320 (2022).
14. Niu, S. *et al.* A wireless body area sensor network based on stretchable passive tags. *Nat Electron* **2**, 361–368 (2019).
15. Kim, D.-H. *et al.* Epidermal Electronics.
16. Wang, C. *et al.* Bioadhesive ultrasound for long-term continuous imaging of diverse organs. *Science* **377**, 517–523 (2022).
17. Ates, H. C. *et al.* End-to-end design of wearable sensors. *Nat Rev Mater* **7**, 887–907 (2022).
18. Ray, T. R. *et al.* Bio-Integrated Wearable Systems: A Comprehensive Review. *Chem Rev* **119**, 5461–5533 (2019).
19. Kim, J., Campbell, A. S., de Ávila, B. E.-F. & Wang, J. Wearable biosensors for healthcare monitoring. *Nat Biotechnol* **37**, 389–406 (2019).

20. Wang, M. *et al.* A wearable electrochemical biosensor for the monitoring of metabolites and nutrients. *Nat. Biomed. Eng* **6**, 1225–1235 (2022).
21. Gao, W. *et al.* Fully integrated wearable sensor arrays for multiplexed in situ perspiration analysis. *Nature* **529**, 509–514 (2016).
22. Stress Markers for Mental States and Biotypes of Depression and Anxiety: A Scoping Review and Preliminary Illustrative Analysis - Megan Chesnut, Sahar Harati, Pablo Paredes, Yasser Khan, Amir Foudeh, Jayoung Kim, Zhenan Bao, Leanne M. Williams, 2021. https://journals.sagepub.com/doi/10.1177/24705470211000338.
23. Translational gaps and opportunities for medical wearables in digital health | Science Translational Medicine. https://www.science.org/doi/10.1126/scitranslmed.abn6036.
24. Wang, B. *et al.* Wearable aptamer-field-effect transistor sensing system for noninvasive cortisol monitoring. *Science Advances* **8**, eabk0967 (2022).
25. Sheibani, S. *et al.* Extended gate field-effect-transistor for sensing cortisol stress hormone. *Commun Mater* **2**, 1–10 (2021).
26. Sancini, A. *et al.* Work related stress and blood glucose levels. *Ann Ig* **29**, 123–133 (2017).
27. Hermann, R., Lay, D., Wahl, P., Roth, W. T. & Petrowski, K. Effects of psychosocial and physical stress on lactate and anxiety levels. *Stress* **22**, 664–669 (2019).
28. Kubera, B. *et al.* Rise in plasma lactate concentrations with psychosocial stress: a possible sign of cerebral energy demand. *Obes Facts* **5**, 384–392 (2012).
29. Klous, L., de Ruiter, C. J., Scherrer, S., Gerrett, N. & Daanen, H. a. M. The (in)dependency of blood and sweat sodium, chloride, potassium, ammonia, lactate and glucose concentrations during submaximal exercise. *Eur J Appl Physiol* **121**, 803–816 (2021).
30. Goodman, A. M. *et al.* The hippocampal response to psychosocial stress varies with salivary uric acid level. *Neuroscience* **339**, 396–401 (2016).
31. Recent advances in solid-contact ion-selective electrodes: functional materials, transduction mechanisms, and development trends - Chemical Society Reviews (RSC Publishing). https://pubs.rsc.org/en/content/articlelanding/2020/cs/c9cs00587k.
32. Pow, J., Lee-Baggley, D. & DeLongis, A. Threats to communion and agency mediate associations between stressor type and daily coping. *Anxiety Stress Coping* **29**, 660–672 (2016).
33. Crestani, C. C. Emotional Stress and Cardiovascular Complications in Animal Models: A Review of the Influence of Stress Type. *Front Physiol* **7**, 251 (2016).
34. Hay, E. L. & Diehl, M. Reactivity to daily stressors in adulthood: the importance of stressor type in characterizing risk factors. *Psychol Aging* **25**, 118–131 (2010).

Chapter 6

WEARABLE AFFECTIVE GENERAL INTELLIGENCE

Emotions fundamentally shape decision-making, social interactions, and overall well-being; however, current emotion regulation strategies are largely reactive, costly, and inaccessible, often requiring frequent professional support that is impractical for daily assistance. Autonomic physiological signals offer continuous and reliable indicators of emotion dysregulation across populations that could supplement current mental health approaches; however, existing wearable platforms face critical barriers in generalizing affective intelligence across arbitrary samples, settings, and devices. The main obstacles include limited and temporally fragmented datasets, inconsistent platform and sensing modalities, and evolving emotion sampling metrics. Consequentially, wearable affective computing models are cohort-, platform-, and emotion-specific, impeding cross-platform validation in ongoing mental health research. Addressing these unmet needs requires a new approach that generalize health predictions by contextualizing across the existing research into comprehensive, overlapping, and multimodal biometric and affective states. In response to these challenges, we introduce a new foundational, intrinsically invertible machine learning architecture designed for stable time-series analysis. We demonstrate its effectiveness within a wearable affective computing platform, providing a new dataset for emotion research. We combine this work with five other distinct datasets to propose a unified hardware-software framework for generalizable, real-time emotion decoding and modulation across populations, settings, and devices.

6.1 Introduction

Emotions emerge from the continuous interplay between physiological responses, behavioral cues, and cognitive interpretations, dynamically shaping decision-making, social interactions, and overall well-being[1-6]. With negative affect and related emotion disorders (e.g., anxiety, depression) being well-established risk factors for cardiovascular, immune, and neuroendocrine dysfunction[7], there is a need for effective emotion management strategies that can be employed on-demand in real-world settings. Current evidence-based therapies are costly, infrequent, and often retrospective, leaving individuals to independently monitor and apply regulation strategies during critical emotional episodes[8,9]. Wearable technologies can supplement the use of therapeutic strategies in response to real-time affective triggers by offering point-of-care assistance for daily emotion monitoring and regulation.

Currently, there are well-documented, reproducible, and autonomic physiological and affective responses that are observed independent of sight, sound, and social cues[10,11], providing wearable platforms with more reliable affective indicators than traditional speech and text modalities[12–14]. However, generalizing wearable affective markers remains challenging when datasets are split across a growing number of medical platforms, bodily locations, and sampling resolutions. When artificial systems fail to recognize and respond to negative cues, users can experience frustration and disengagement, diminishing data-driven strategies for well-being[1,2]. Attaining wearable emotion regulation

support requires a centralized platform-agnostic framework capable of integrating fragmented physiological signals across emerging wearable modalities and intervention strategies[3].

There are several barriers hindering the generalizability of wearable affective computing models. Foremost, many platforms struggle to maintain long-term conformal skin contact over large areas, resulting in motion can span devices and bodily locations. Consequently, physiological datasets are both noisy and artifacts, perspiration-induced signal degradation, and overall discomfort that reduces user compliance. Moreover, no sensing modality provides a comprehensive representation of affective states[15,16], demanding multiple sensors that fragmented, biomarkers, and emotions, undermining the development of universally interpretable and generalizable models. Furthermore, unlike sentiment text analysis frameworks that benefit from extensively labeled open-source multilinguistic passages[17], wearable affective profiling must contend with limited, context-dependent, and privacy-protected data. This severely limits model scalability, resulting in wearable affective computing for emotion regulation remaining in its infancy. For personalized wellness interventions, wearable systems must maintain a unified approach that integrates diverse datasets across platforms, populations, biomarkers, and affective modalities.

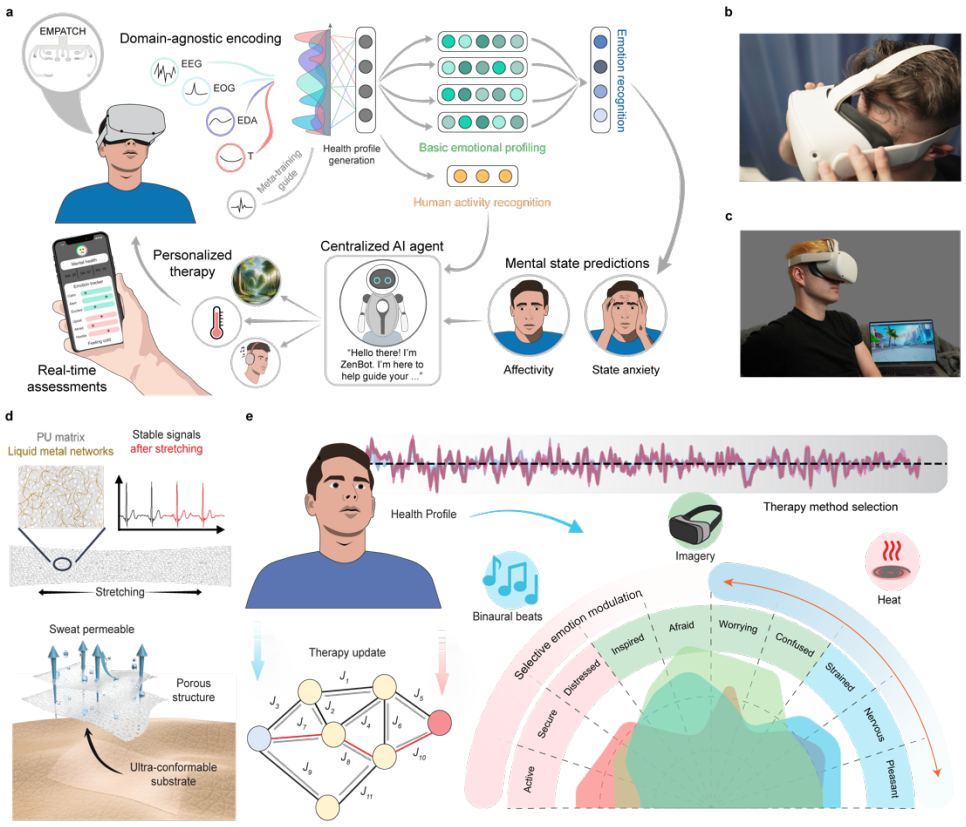

Figure 6.15 Real-time emotion monitoring and adaptive intervention. A) Overview of the closed-loop emotion monitoring and sensory intervention framework. Here, EMPATCH continuously records physiological signals—including electroencephalogram (EEG), electrooculogram (EOG), electrodermal activity (EDA), and temperature (T)—for artificial intelligence-powered affective state prediction and therapy personalization. B) Photograph of EMPATCH applied to the forehead for physiological signal acquisition. C) Photograph of an EMPATCH-assisted generative therapy session utilizing a VR headset with visual feedback displayed on a laptop screen. D) Schematic of the EMPATCH materials, highlighting its ultra-thin, porous polyurethane (PU) matrix embedded with liquid metal interconnects. This stretchable and sweat-permeable design ensures long-term wearability and stable signal acquisition despite high motion and perspiration. E) Illustration of therapy method selection and adaptive intervention strategies. The

system generates a dynamic health profile from biometric data, guiding real-time therapy updates using binaural beats, heat therapy, and immersive imagery for selective emotion modulation.

To address these challenges, we introduce a holistic generalizable hardware–software framework for dynamic affective assessment and modulation (**Fig. 1a**). We achieve domain agnostic profiling by framing a meta-analysis into embedding concurrent biomarkers within a single health profile (HP), reconstructing 118,483 missing biometric details across five bodily locations in 205 features. We demonstrate generalized affective intelligence by meta-learning across five established affective computing datasets—AMIGOS[18], DAPPER[19], CASE[20], EMOGNITION[21], and WESAD[22]—that collectively span different platforms, locations, sensors, and emotional states. Unlike conventional methods that rely on arbitrary feature selection, our approach leverages shared information by treating each input as an independent time-dependent observable constraint that discriminates improper embedding profiles. Central to this framework is a foundational, intrinsically invertible Lie manifold neural architecture that minimizes free parameters in small datasets while providing clear geometric interpretations of the model's behavior. As a comprehensive lossless physiological snapshot, the health profile enables efficient generalizable downstream evaluation of 100 affective expressions across 49 real-life and laboratory scenarios.

To demonstrate real-world potential, we further introduce the Emotion Monitoring Patch for Therapeutic Healthcare (EMPATCH), a conformal, ultrathin epidermal electronic platform that continuously monitors electroencephalogram (EEG), electrooculogram (EOG), electrodermal activity (EDA), and temperature (**Fig. 1b**,**c**). EMPATCH is fabricated through a phase-separated float assembly (PSFA) process that yields ultrathin, breathable and porous materials optimized for long-term wearability, motion artifact resistance, and perspiration stability, enhancing long-term signal fidelity and comfortability in large area designs (**Fig. 1d**). We validate EMPATCH within affect-inducing sensory triggers, including cold pressor test (CPT), exercise, music, and virtual reality (VR) imagery. We demonstrate EMPATCH's closed-loop therapeutic potential using thermal, visual, and auditory sensory intervention strategies delivered through virtual, holographic, and conversational artificially intelligent (AI) agents (**Fig. 1e**). This closed-loop AI-powered framework enables real-time emotion monitoring and modulation, offering a scalable and generalizable foundation for the next-generation of emotionally intelligent wearable healthcare.

6.2 Generating low-dimension physiological representations

While transformer architectures have demonstrated remarkable proficiency in understanding emotions within text and speech—an essential criterion for effective human-computer interactions—they are primarily designed to capture semantic correlations rather than continuous temporal trends. This limitation poses a challenge in wearable affective computing, where biometric signals

evolve through nonlinear temporal dynamics. Lie theory offers a complementary and structured approach for modeling time-series data through smooth rotations on a differentiable manifold. The associate Lie group transformations are intrinsically invertible, preserve covariant properties, and decompose into intuitive two-dimensional operations. These features position Lie theory as a strong candidate for enhancing the interpretability of deep neural networks in scientific computing health applications.

Wearable scientific computing platforms must address challenges such as temporal fragmentation caused by motion artifacts, data loss, variability across biomarkers, and electrode misalignment between trials. Lie group transformations offer a geometrically consistent framework for modeling these variations by leveraging differential symmetries across physiological signals. Like neural operators, Lie manifolds define a continuous, smooth, and differentiable domain over which discretized signals can be rotated and transformed. Their structured and interpretable formulation improves transparency within deep learning models, mitigating the “black box” limitation often associated with conventional architectures. These properties support more robust, reliable, and explainable wearable affective computing models.

The use of Lie theory in scientific computing is already well-established, from deep learning Lie group symmetries to defining interactions in the Standard Model of particle physics. However, despite its rich mathematical foundation,

Lie manifolds remain underexplored within foundational deep learning architectures, where structured invertibility, differentiability, and geometric preservation could offer significant advantages. This is especially relevant in wearable affective computing, where biometric signals exhibit nonlinear dynamics that would benefit from geometrically consistent operations. Given the challenges outlined, incorporating Lie group transformations into neural models presents a promising avenue for advancing the field of wearable affective computing, offering a mathematically grounded approach for extracting biometric patterns from multivariate signals.

6.2.1 Lie manifold-based neural embeddings

To learn cross-platform biometric information for downstream affective analysis, we first consolidate all physiological signals into a unified health profile that corrects for temporal misalignment, data fragmentation, and sensor dropout (**Fig. 2a**). We maintain biological significance within each embedded profile by introducing an intrinsically invertible Lie manifold neural architecture that preserves biometric covariant properties and relative spatial relationships within a lossless, differentiable domain. Here, all inputs are bidirectionally linked to the HP with transformations that intuitively simplify into a series of planar operations, enabling direct visualizations of deep learning model dynamics. The need for such geometric consistency and model interpretability in scientific computing applications motivates a deeper exploration of Lie theory within

neural architectures[23], offering a bounded, periodic learnable domain with structured, visualizable, and interpretable components.

Conventional reversible architectures, such as normalizing flows, maintain invertibility through affine coupling layers that partition and process signals as fragmented chunks, disrupting temporal coherence and often storing Jacobians, principal axes, or activation parameters for the backward pass[24–26]. In contrast, Lie manifold architectures (see Methods) maintain temporal properties through scaled Lie group transformations, $a_h e^{\hat{S}_h}$, in distinct non-linear coordinate systems (**Fig. 2b,c**), reversibly rotating information along the temporal axis. Here, the Lie group $e^{\hat{S}_h}$ preserves signal volume, L_2-normalization, and relative spatial relationships[24]. The scalar a_h provides controlled magnitude adjustments, modulating the layer's Lipschitz constant to stabilize intermediate amplitudes without spectral normalization strategies[27–29]. Meanwhile, the learnable non-linear projection permits invertible non-volume preserving transformations. Lie manifold architectures are thereby structured to be intrinsically invertible (**Fig. 2d**) across arbitrary weight updates with constant-time complexity, $\left(e^{\hat{S}_h}\right)^{-1} = \left(e^{\hat{S}_h}\right)^{T}$. This inherent reversibility eliminates the need for auxiliary memory structures while ensuring stable backpropagation for time-series signals.

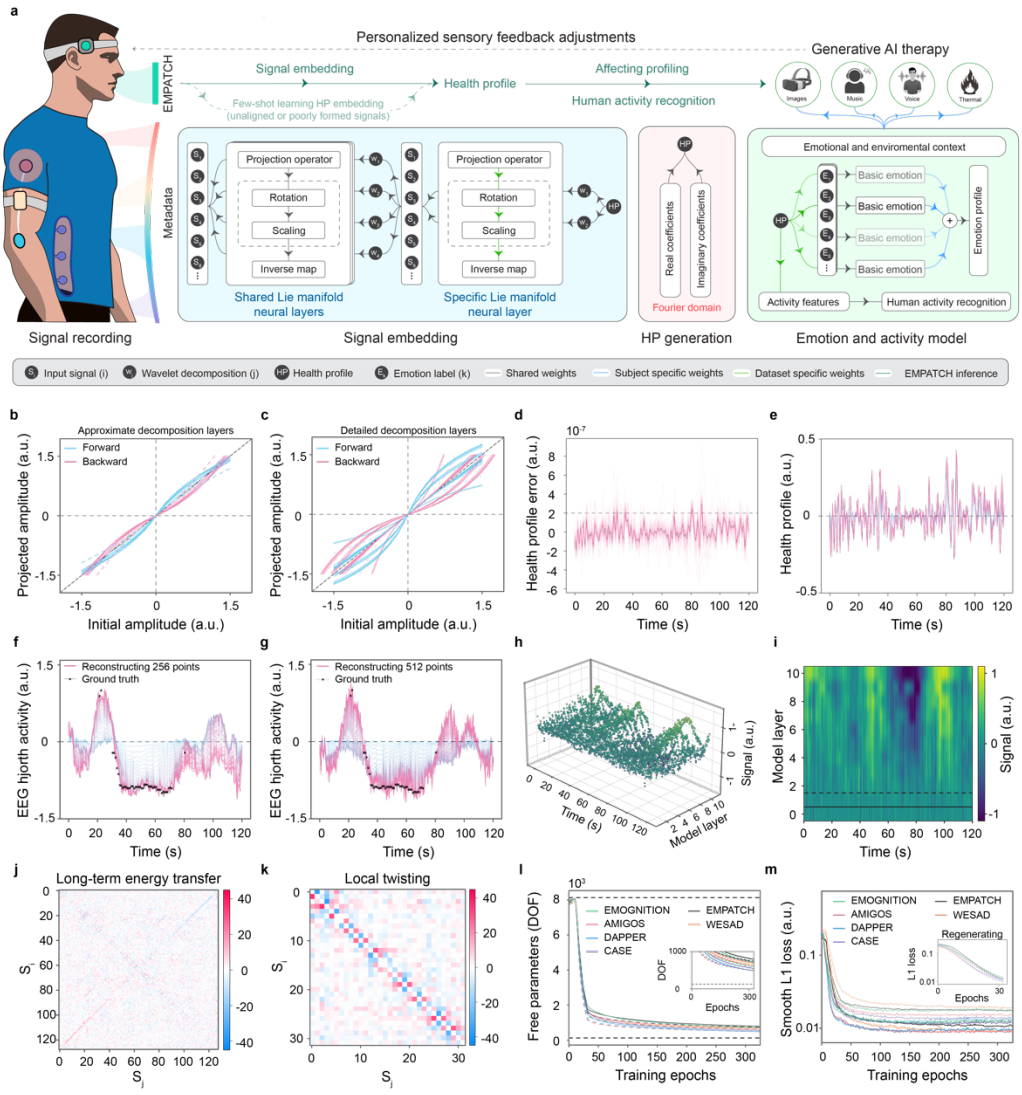

Figure 6.16 Lie manifold neural architecture for biomarker embedding. A) Schematic of the Lie manifold neural architecture illustrating the full dual pipeline from (left) biomarker reconstruction and health profile generation to (right) downstream affective profiling. (B–C), The final learned nonlinear projections within the wavelet neural operators for the approximate wavelet decomposition (B) and the detailed (C) wavelet decompositions. D) Reconstruction error of the health profile after inverting eight hidden Lie manifold layers with four wavelet decompositions. E) Health profile inference after 32 training epochs. (F–G), Two

separate EEG Hjorth activity model inferences from the health profile with (F) 256 (G) and 512 points. H) 3D visualization of the health profile evolving across hidden layers. I) 2D representation of the signal flow through hidden layers. (J–K), Rotational generator heatmaps for the detailed (J) and approximate (K) wavelet decompositions. L) Reduction of parameters during training through progressive angular pruning (threshold: 0.05°–5°), starting from an initial 8128 degrees of freedom in the signal-specific wavelet decomposition layers with an initial health profile dimension of 256 elements. The inset zooms into the curve from 0 to 1000 parameters. M) Smooth L1 loss curves for embedding the AMIGOS, CASE, EMOGNITION, and DAPPER datasets, with analogous results for WESAD and EMPATCH (trained separately). The inset shows the health profile inference losses from 32 epochs with fixed model layers.

To learn both short- and long-term biometric patterns, we embed Lie manifold architectures within biorthogonal wavelet neural operators for multi-resolution temporal analysis. Neural operators learn complex relationships by projecting discretized signals onto continuous functional spaces[30]. However, traditional wavelet and fast Fourier methods typically assume uniformly sampled inputs, which is problematic in real-time wearable datasets where motion artifacts and data loss introduce temporal irregularities and frequency distortions.

To accommodate notoriously fragmented and irregularly sampled inputs, we train the bidirectional Lie manifold architecture in reverse mode, learning to generate a uniformly oversampled HP embedding that describes all observable signals (**Fig. 2e**). The HP sampling frequency is treated as a tunable hyperparameter that sets the minimum Nyquist limit required for fine-detail

reconstruction—a temporal resolution that is already bounded by hardware-specific constraints. This oversampled representation temporally aligns input signals without introducing ground truth distortions. Meanwhile, fully aligned readings permit direct inference of the HP for immediate downstream affective analysis.

We discriminate improper HP embeddings by calculating the loss between the associated hyper-sampled reconstruction and the recorded timepoints, treating each input point as an independent observable time constraint. By embedding comprehensive and overlapping biomarkers into the profile, the model can infer and regenerate missing signals from concurrent physiological information, accommodating sensor dropout or data packet loss (**Fig. 2f**,**g**). Through wavelet neural operators, the architecture learns the underlying surrounding structure, enabling smooth reconstruction while preserving the latent signal properties across hidden layers (**Fig. 2h**,**i**). We can assess the model's internal structure through its predominant angular parameters. In the detailed wavelet decomposition, we observe anti-diagonal banding associated with long-term temporal attention (**Fig. 2j**), while the approximate coefficients reveal phase-shifted, twisted structures (**Fig. 2k**).

During training, Lie manifold architectures readily highlight identity transformations for removal, $e^0 = I$, which is typically challenging in traditional deep neural layers without distorting downstream predictions[31]. We can therefore

begin in an overparameterized state, with $O(n^2)$ complexity per layer, avoiding restrictive assumptions about the solution space. As training progresses, the model refines its angular distributions, naturally converging toward a dataset-specific compressibility limit (**Fig. 2l**). This principled reduction in free parameters enables efficient data compression within small datasets, allowing the model to choose its weights without imposing a priori sparsity constraints.

A Lie manifold architecture is particularly well-suited for wearable affective computing, where fragmented signals, heterogeneous sensors, limited data, and temporal misalignment remain persistent challenges. By pruning redundant transformations, we reduce dataset-specific parameters from $O(n^2) \rightarrow O(n)$ (**Fig. 2l**), effectively shifting reconstruction information from the model to the embedded profile. Any remaining weights serve as a statistical metric for evaluating dataset-specific learning dynamics. Through a reversible architecture, we further ensure that downstream affective analyses remain grounded in biologically meaningful patterns, even when data is sparse. Notably, all weights carry physical meaning (e.g. rotation or scaling), permitting an intuitively bounded, periodic learning domain that stabilizes training. We validated the generalizability of our meta-analysis by extending the model to embed two small out-of-domain datasets—EMPATCH and WESAD (**Fig. 2m**), establishing a new class of foundational bidirectional architectures for learning temporal patterns in small, fragmented biometric samples.

6.3 Fabrication of the EMPATCH platform

Effective real-time affective computing additionally requires wearable platforms capable of capturing high-fidelity multimodal physiological signals while maintaining long-term stability, adaptability, and comfortability during high-stress daily activities[15]. While recent advances in soft bioelectronics have improved skin conformability, most current fabrication approaches rely on time-intensive, cleanroom-dependent processes[32–36] that limit scalability and adaptability in large-area designs. To overcome these challenges, we developed an ultrathin, stretchable electronic skin—EMPATCH—engineered for continuous biometric monitoring under sweat, motion, and extended wear.

EMPATCH is fabricated through a phase-separated float assembly technique that enables rapid and scalable fabrication of ultrathin, elastic, breathable, and sweat-permeable polyurethane-based (PSFA-PU) electronic skins with porous silver nanowire (PSFA-PN) sensors (**Fig. 3a**). This process begins with nanocomposite precursor solution, where polyurethane (PU) is dissolved in tetrahydrofuran (THF) and silver nanowires (AgNWs), which are dispersed in ethanol[37]. When drop-cast onto a water bath, the THF and ethanol dissolve, reducing surface tension and inducing Marangoni flow, which expands the droplet boundary and forms an ultrathin nanocomposite film at the water–air interface (**Fig. 3b**). Concurrently, evaporation-driven liquid–liquid demixing induces phase separation, forming PU-rich and PU-poor regions (**Fig. 3b**). AgNWs, due to their amphiphilic ligands and immiscibility with PU, localize within the PU-poor

domains. The path trajectory of the precursor solution illustrates the in situ phase separation process, which transitions from co-continuous phase formation to spontaneous drying, yielding continuous porous PU structures.

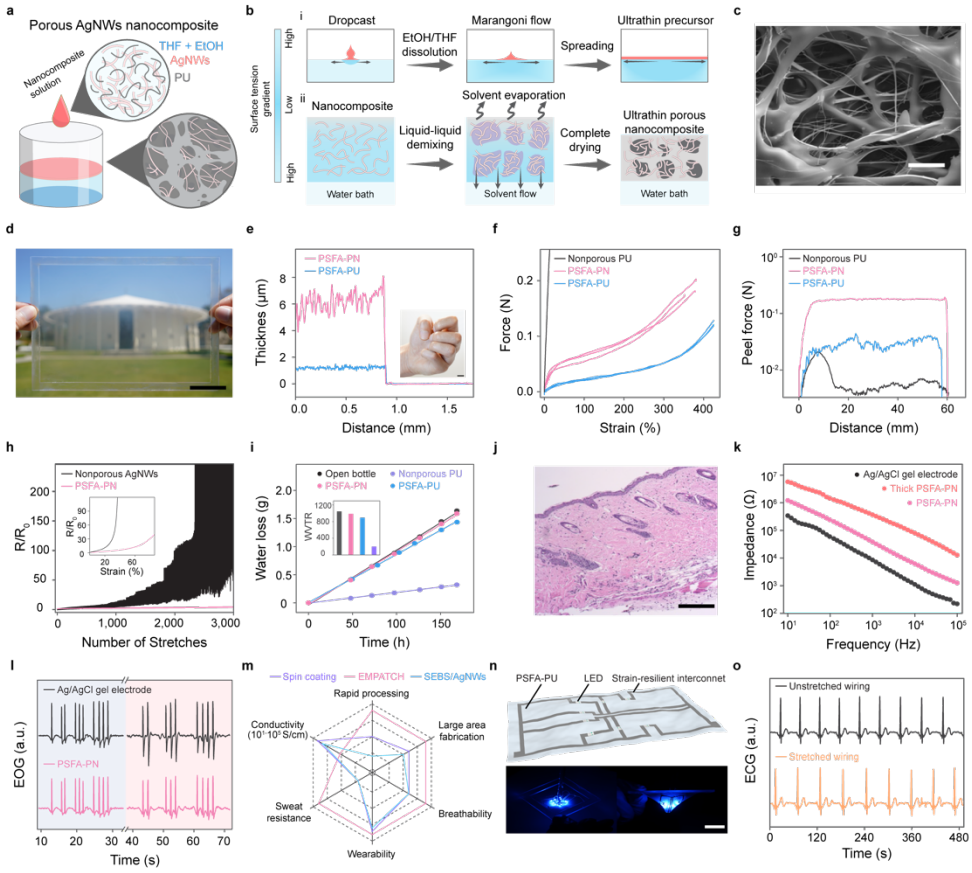

Figure 6.17 Fabrication and characterization of the EMPATCH. (A,B) Schematics of the phase-separated float assembly (PSFA) technique. The nanocomposite precursor solution is drop-casted into a water bath (A), initiating Marangoni flow and in situ phase separation to create a porous network (B). THF, tetrahydrofuran; EtOH, ethanol; PU, polyurethane; AgNWs, silver nanowires. C) Scanning electron microscopy (SEM) image of the ultrathin porous AgNW nanocomposite (PSFA-PN). Scale bar, 5 μm. D) A photograph of the ultrathin porous PU (PSFA-PU) supported by an acrylic frame. Scale bar, 4 cm. E) Thickness

profiles of the PSFA-PN (6 μm) and PSFA-PU (1 μm). The inset highlights intimate skin contact. Scale bar, 1cm. F) Tensile force as a function of tensile strain for PSFA-PN, PSFA-PU, and nonporous PU (20 μm thick) with a sample width of 5.0 mm. G) Peel force vs. displacement curves of PSFA-PN, PSFA-PU, and nonporous PU from human skin. H) Relative resistance changes of nonporous AgNWs and PSFA-PN subjected to 3,000 cycles of cyclic stretching at 25% strain. Inset: resistance variations under uniaxial stretching. I) Water vapor permeability tests comparing PSFA-PN and PSFA-PU with nonporous counterpart (20 μm). The inset shows extracted water vapor transmission rates (WVTR). J) Hematoxylin and eosin staining of mice tissue covered with PSFA-PN on day 7. Scale bar, 100 μm. K) Impedance profiles of the skin–electrode interface of the PSFA-PN compared with its thick counterpart (~200 μm) and commercial gel electrodes. L) EOG signals obtained from PSFA-PN and Ag/AgCl gel electrodes before and after sweating. M) Radar chart comparing EMPATCH fabricated using PSFA with other state-of-the-art wearable technologies. SEBS, styrene-ethylene-butylene-styrene. Note that these characteristics except for conductivity are qualitative values. N) Schematic and photographs of light-emitting diode (LED) arrays fabricated with strain resilient interconnects, demonstrating flexibility under mechanical strain. Scale bars, 1 cm. O) Real-time ECG signals recorded with strain-invariant electrical wiring before and after stretching.

The resulting porous nanocomposite consists of randomly distributed AgNWs confined in a porous PU matrix, creating interconnected conductive percolation pathways (**Fig. 3c**). Unlike conventional fabrication processes, PSFA enables rapid fabrication of large-area (>200 cm^2), ultrathin (1 μm for PSFA-PU, 6 μm for PSFA-PN), and highly stretchable (400%) porous films with intimate skin conformability, ideally suitable for emotion-responsive sensing (**Fig. 3d–g**). Electrical conductivity varies with AgNW weight fractions and achieves an

optimized value of ~89,380 S m^{-1} for 12.7 wt.% AgNWs following cold welding with sodium borohydride. The porous conductor also exhibits robust mechanical stability, with minimal resistance change (R/R_0 = 4.8) after 3,000 stretching cycles at 25% strain—substantially outperforming non-porous control (R/R_0 > 200; **Fig. 3h**). This superior electrical stability is attributed to the synergistic stress dissipation within the elastic PU matrix and strain-adaptive AgNW networks. Owing to these properties, EMPATCH sensors can therefore maintain stable electrical performance across various conditions.

To further enhance comfort and long-term wearability, we incorporated a sweat-pore-inspired architecture into the EMPATCH framework, promoting superior breathability and moisture transport. The platform exhibits high moisture permeability within water vapor permeability tests (**Fig. 3i**) and excellent long-term biocompatibility as confirmed by hematoxylin and eosin (H&E) staining in mice (**Fig. 3j**).

To assess EMPATCH for electrophysiological signal recording, we first evaluated electrode-skin contact impedance and signal stability. The ultrathin porous electrode exhibited notably lower impedance compared to its thicker counterpart (~200 μm), due to its intimate skin interface (**Fig. 3k**). Additionally, EOG signals recorded before and after sweating using the porous on-skin sensors closely matched those obtained with Ag/AgCl gel electrodes, demonstrating stable signal fidelity (**Fig. 3l**). When benchmarked against state-of-the-art

materials fabricated via spin-coating and float-assembly techniques[38,39], EMPATCH outperformed in processing efficiency, large-area fabrication, breathability, wearability, sweat resistance, and electrical conductivity (**Fig. 3m**).

To ensure mechanical stability under dynamic skin deformations, we integrated strain-resilient interconnects composed of a porous liquid metal composite[40]. These interconnects maintained consistent electrical performance during extensive mechanical deformation, as demonstrated by a functioning light-emitting diode (LED) array under bending, twisting, and stretching (**Fig. 3n**), due to their strain-invariant electromechanical properties. The interconnects also exhibited exceptional robustness, surviving scalpel punctures, hammer impacts, and tweezer pricks without performance degradation. Even during repeated stretching, EMPATCH sustained high-quality electrophysiological signal acquisition with negligible variation (**Fig. 3o**).

6.4 Affective dataset acquisition and characterization

6.4.1 Biomarker selection

Four affective physiological biomarkers were selected due to their abilities to monitor autonomic biological responses. The following provides an overview of each biomarker selected.

Electroencephalography measures extracellular voltage fluctuations generated by the synchronized postsynaptic potentials of pyramidal neurons in the cerebral cortex. Frontal EEG asymmetry has been implicated in emotional processing,

offering insights into both stable emotional traits and dynamic responses to stimuli. Davidson's Approach-Withdrawal model underscores the utility of EEG in distinguishing between trait-level emotional dispositions and state-dependent emotional responses. Individuals with a disposition toward positive affect, characterized by greater left frontal activity, are more inclined toward engaging behaviors, while those with a disposition toward negative affect, marked by greater right frontal activity, exhibit stronger withdrawal tendencies. Frontal EEG asymmetry reflects transient changes in response to varying emotional stimuli, capturing the dynamic interplay between brain activity and affective experiences.

Electrodermal activity reflects changes in skin conductance driven by sympathetic nervous system activity, serving as a key marker of autonomic emotional arousal. EDA signals can be decomposed into tonic (baseline) and phasic (event-related) components and have been shown to be stronger indicators of emotional arousal than of emotional valence. EDA responses are particularly sensitive to emotionally salient stimuli, including conditioned responses and decision-making processes, and are modulated by higher-order cortical regions such as the ventromedial prefrontal cortex and amygdala.

Skin temperature, regulated by the autonomic nervous system, serves as a physiological indicator of emotional and thermoregulatory responses. Certain emotional states, such as embarrassment or relaxation, are associated with vasodilation and increased peripheral blood flow, resulting in localized skin

warming. These thermoregulatory changes are primarily modulated by sympathetic nervous system activity, with norepinephrine-mediated vasomotor control regulating vasoconstriction and vasodilation.

Electrooculography (EOG) measures changes in the corneo-retinal potential associated with eye movements—including saccades, fixations, and blinks—providing physiological markers that correlate with affective and cognitive states. For instance, increased blink rates have been linked to heightened anxiety and cognitive fatigue, while certain patterns of saccadic activity—such as increased frequency or reduced latency—may reflect heightened emotional arousal or attentional engagement.

6.4.2 Dataset evaluation

Wearable affective computing explores how physiological processes regulate distinct emotional interpretations across varying external conditions. Similar to physical health models that contextualize biometric information to generalize sample-specific trends and observations[41], we compiled five widely used metadatasets to provide a robust framework for affective profiling across emotions, activities, and biomarkers. We further introduce an out-of-domain affective computing dataset evaluated across four sensory triggers—music (auditory), VR imagery (visual), biking exercise (physical exertion), and cold stimulation (tactile). Each condition represents a well-established affect modulation strategy—sound therapy, immersive relaxation, aerobic exercise, and

thermal regulations—supporting the development of personalized sensory-based interventions.

EMPATCH monitors four established physiological signals—EOG, EEG, EDA, and skin temperature—with data transmitted wirelessly via a securely encrypted protocol (**Fig. 4a**,**b**). Simultaneously, EMPATCH records 30 self-annotated affect labels through the Positive and Negative Affect Schedule (PANAS) and State-Trait Anxiety Inventory (STAI) Y1 questionnaires. These examinations capture a range of positive and negative affective states as well as indicators of clinically relevant state anxiety, with prior validity shown in our targeted demographics[42–44]. Each experimental session was divided into three distinct phases—baseline, sensory modulation, and recovery. All physiological signals were preprocessed using biomarker-specific algorithms (**Fig. 4c**) to ensure consistency and quality in downstream analysis.

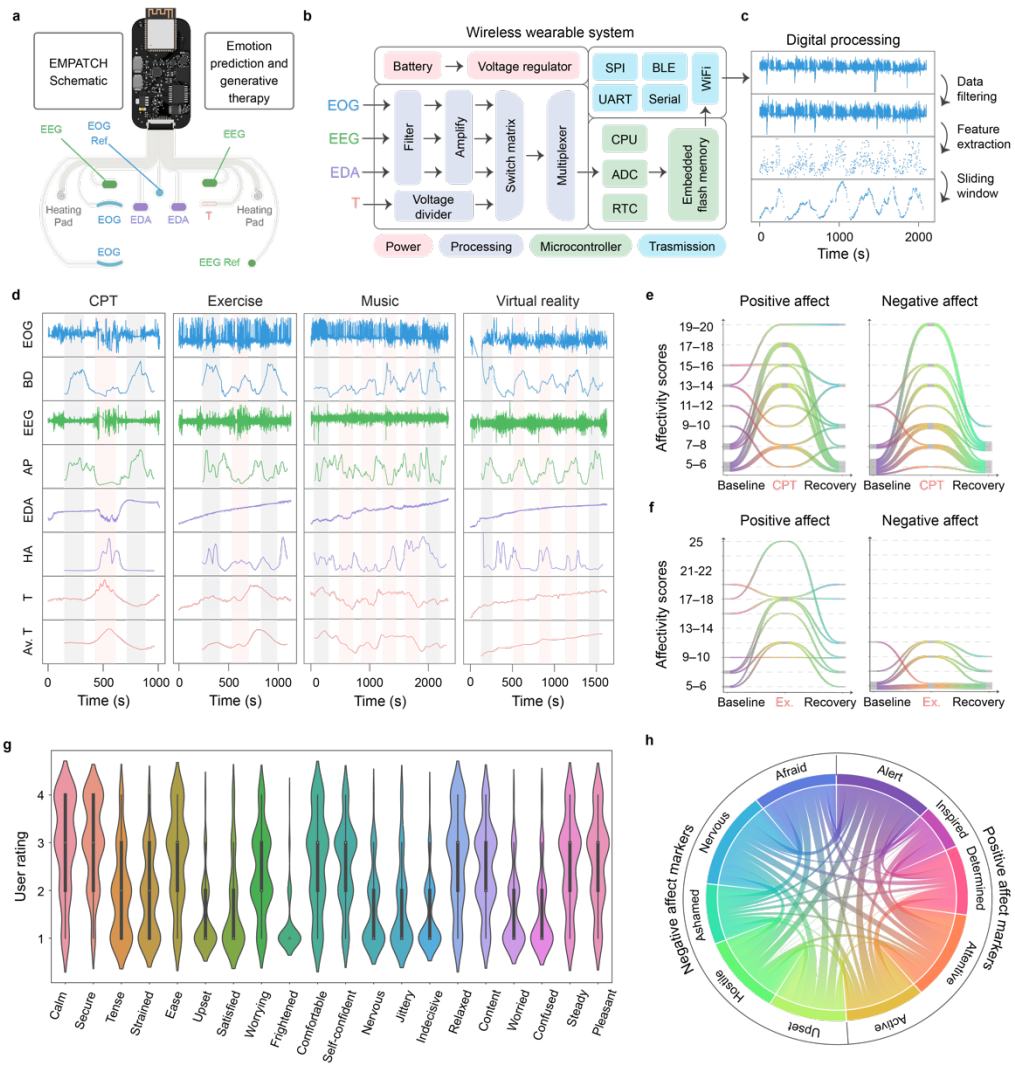

Figure 6.18 Signal acquisition, processing, and feature extractions. A) A schematic of the EMPATCH platform for monitoring EEG, EOG, EDA, and temperature as well as providing heat therapy. Ref, reference. B) A block diagram of the wireless wearable system that interfaces with the EMPATCH platform for signal acquisition. C) A digital processing pipeline, outlining signal progression from raw data, filtering, feature extraction, and 30-s sliding window averages. D) Selected EMPATCH physiological responses and features across four sensory conditions: cold pressure test, exercise, music, and virtual reality. From top to bottom, the rows represent EOG data, blink duration (BD), EEG data, EEG alpha

power (AP), EDA, EDA Hjorth activity, temperature, and mean temperature. (E–F), A Sankey diagram showing how the affective responses changed across all subjects (E) throughout the cold pressor test (CPT) and (F) exercise (Ex.) conditions. G) A violin plot showing self-labeled State-Trait Anxiety Inventory (STAI) emotion distributions across all subjects. H) A chord diagram displaying the correlations amongst Positive and Negative Affect Schedule (PANAS) markers across all subjects.

To confirm EMPATCH signal fidelity, we evaluated physiological (**Fig. 4d**) and affect (**Fig. 4e–h**) data against prior known responses from each condition. The CPT produced an observable reduction in alpha power, consistent with nociceptive stressor-induced cortical activation[45], along with concurrent increases in state anxiety (STAI-S), positive affect (PA), and negative affect (NA)—reflecting the dual experience of physiological discomfort and heightened awareness associated with acute pain (**Fig. 4e**). The main driving forces of PA fluctuations during the CPT were increased alertness and attentiveness, while NA fluctuations were dominated by increased hostility and nervousness. In contrast, biking exercise primarily triggered thermoregulatory adaptations—such as sweating and skin heating—with increases in STAI-S and PA associated with being more active, inspired, and alert from physical exertion, without substantially altering any NA indicators (**Fig. 4f**).

The final STAI-S, PA, and NA metrics are compiled from summing all affect annotations to generalize across different settings as subjects only recognize a subset of these emotions within any session. Across our sensory conditions, we

found a few emotions with minimal variability: notably, the sensory triggers did not substantially impact fear (**Fig. 4g**). However, there are high intercorrelations across affect annotations (**Fig. 4h**), reinforcing the idea that emotional expressions are linguistical constructs that share underlying influences[46,47]. This permits downstream affective computing algorithms to target shared primitives that connect each complex emotion, improving the adaptability and generalizability of affective models across evolving languages and cultural expressions, even within limited sample distributions.

6.5 Mental health interventions

The EMPATCH platform enables closed-loop, personalized emotion monitoring and modulation by integrating advanced sensory interventions—including thermal, auditory, and visual modalities (**Fig. 5a**). Built upon a Lie manifold neural architecture, the system generalizes affective dynamics encoded within the health profile across diverse platforms and cultural contexts. Personalized modulation is achieved using an adaptive A* algorithm and interfaces with thermal stimulation, binaural beats, virtual reality, holographic displays, and conversational AI agents, illustrating the scalability and robustness of the platform for next-generation affective therapies.

To model affective states across individuals and datasets, we performed a meta-analysis that extracts shared emotion primitives—basic emotions—from the health profile[47]. These primitives serve as building blocks for predicting complex

emotional states, with bidirectional traceability from model outputs back to individual physiological observations (**Fig. 2a**). Basic emotion predictions (**Fig. 5b**) were further adapted using user-specific weights to account for inter-individual variability and generate personalized complex emotion profiles (**Fig. 5c**). Human activity recognition was concurrently performed to provide contextual awareness (**Fig. 5d**). Following meta-training on AMIGOS, DAPPER, CASE, and EMOGNITON, the model was validated on both research-grade (EMPATCH) and commercial-grade (WESAD) datasets (**Fig. 5e**), achieving emotion and activity classification accuracies of 81–98%. These results were consistent with benchmark performance within each dataset while remaining extensible to new affective profiling tasks.

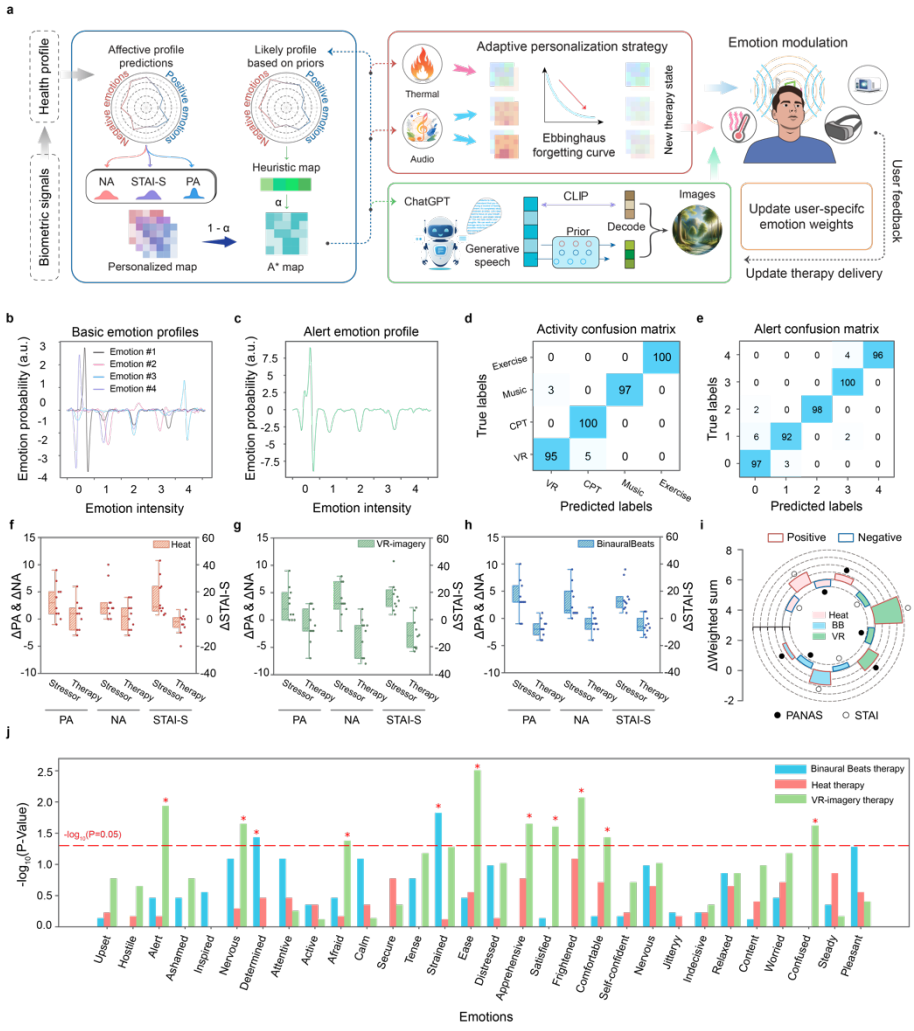

Figure 6.19 Model and experimental validations of emotion modulation. (A) Schematic of the emotion modulation therapy algorithm. Prior population-based heuristics were assessed for all potential therapy parameters, mitigating the cold start problem. Heuristics on potential affective profiles within different strategies are combined with the current emotion profile to assess future positive affect (PA), negative affect (NA), and state anxiety (STAI-S) scores from potential intervention parameters (blue box). This aids in choosing the next best intervention strategy, before the model fully relies on subject-specific trends (red box). Heuristic states are also integrated within ChatGPT's message history for AI-driven therapeutic

conversations and imagery (green box, CLIP: Contrastive Language–Image Pre-training). (B–C), All distributions are processed from a health profile of 256 elements, where class intensities are extracted from each output distribution by dividing the dimension into even class segments. A final emotion probability distribution with raw unnormalized logits is shown for the (B) basic emotions and (C) complex emotion (Alert). (D–E), Confusion matrices within the EMPATCH dataset for (D) human activity recognition and (E) predicting a complex emotion (Alert). (F–H), Therapy effectiveness comparisons on 10 different participants, evaluating PA, NA, and STAI-S changes before and after CPT-induced stress and therapy interventions. The box plot's center line represents the median bounded by first and third quartiles. Whisker extends to the maximum and minimum of 1.5 times interquartile range (IQR) of the box plot. I), Radar plot comparing cumulative changes in aggregated PANAS and STAI scores following therapy interventions. BB, binaural beats. For clarity, the radial axis values are labeled on the left, which correspond exactly to the concentric circles within the radar plot. J) Paired t-test analysis of emotion modulation effects for each therapy across PANAS and STAI emotions. A dashed line is placed at $-\log_{10}(p) \approx 1.3$ corresponding to a significance change with $(p = 0.05)$.

To translate model predictions into meaningful intervention strategies, we incorporated OpenAI's ChatGPT and DALL·E 3 APIs to generate conversational responses and adaptive visualizations in real-time, tailored to each user's affective state. These outputs were rendered through both virtual and holographic displays, aligning with user preferences to increase engagement. Prior affective annotations collected within each sensory module were embedded into ChatGPT's conversation history and the A* heuristic map, enhancing continuity and contextual relevance during parameter selection. This personalized framework enabled the model to converge toward an optimal intervention state

through iterative refinement, dynamically balancing exploration and exploitation. By integrating both population-level affective priors and real-time user-specific feedback, the system adaptively optimized parameter selection based on cumulative emotional history. To quantify affective outcomes across strategies, a weighted score was computed using PA, NA, and STAI-S values with respective weights of 0.1, 0.1, and 0.8. This aggregated metric provided a more stable and interpretable target for guiding ChatGPT-generated responses, binaural beat adjustments, and thermal modulations.

All intervention strategies were administered during CPT (**Fig. 5f–h**), which elicited the widest affective range in the EMPATCH database. Among the modalities tested, VR immersive imagery proved the most effective, producing a median increase of 3.5 points in PA, a 4.5-point reduction in NA, and a 28-point reduction in STAI-S. PA responses also improved by 20% with this immersive imagery. In contrast, binaural beat stimulation and heat therapy at the temples primarily modulated STAI-S, improving anxiety scores by 18.4- and 11-point reductions, respectively. These effects were more sensitive to individual preferences, suggesting that user-specific tuning is critical for non-visual interventions. Overall, each intervention strategy should be tailored to the dominant form of emotion regulation (**Fig. 5i**).

To determine how broadly each strategy influenced anxiety-related cognition, we conducted paired t-tests on item-level shifts within the STAI-S following

intervention. Virtual reality imagery significantly modulated nine STAI-S items, including those related to tension, calmness, and ease. Participants reported feeling notably more at ease during VR immersive imagery, with a statistically significant improvement, p-value of .003, and a 95% confidence interval indicating the true mean range lies between 0.35 and 1.25 points signifying the therapeutic effect of VR intervention. Binaural beats significantly modulated two anxiety items related to focused attention, while heat therapy did not yield significant changes, likely due to individual variability in thermal sensitivity at the temples (**Fig. 5j**). These results suggest that VR-based imagery offers more comprehensive, generalizable affective modulation, whereas auditory and thermal stimuli may provide more targeted benefits that should be tailored to the user[48].

6.6 Lie manifold neural architectures

6.6.1 Constructing Lie manifold neural architectures

W Lie manifold neural architectures are designed to extract meaningful temporal patterns from time-series signals, where biometric covariant properties propagate smoothly along each layer. Lie group transformations enable structured temporal analysis by preserving a signal's mean, variance, and L_2-normalization. These properties maintain signal magnitudes across linear layers, contributing to gradient stability. We structure the linear component $\hat{A}_h$ at any hidden layer h as the following scaled Lie group transformation.

$$\hat{A}_h = a_h e^{\hat{S}_h} \quad (1)$$

Here, we define $\hat{S}_h \in \mathbb{R}^{nxn}$ to be a skew-symmetric matrix operator satisfying $\hat{S}_h = -\hat{S}_h^T$. Within equation (1), the matrix exponential $e^{\hat{S}_h}$ maps $\hat{S}_h$ from the Lie algebra $\mathfrak{so}(n)$ to the Lie group $SO(n)$, inducing an orthogonal linear rotation that preserves relative spatial relationships. While biometric signals operate strictly within the real domain, this setup extends to complex subspaces by replacing $\hat{S}_h$ with a skew-Hermitian matrix, whose exponential is a unitary transformation. After the rotation, $a_h \in \mathbb{R}^n$ acts as a learnable normalization scale factor for controlled magnitude adjustments to ensure that the linear operator spans the same vector space as the input. For signal embedding, human activity recognition, and affective profiling, we empirically bound a_h within the range $[0.95, 1.05]$ to remove any large covariant shifts.

In addition to the linear component, the *universal approximation theorem* (UAT) states that a neural architecture with at least one non-linear activation can approximate any continuous function on a compact domain[49]. In practice, neural layers often separate non-linear operations $\hat{\sigma}_h$ and linear transformations $\hat{A}_h$ to achieve stable learning dynamics. Unfortunately, invertible non-linear activations in bidirectional models often disrupt temporal information through affine coupling layers[24–26]. This occurs because continuous, bijective, and analytically invertible activation functions must maintain a balance between diverging to $\pm\infty$ and converging towards a singular value. When converging

towards a constant, the bounded monotonic activation functions cause numerical precision loss during inversion when their derivatives vanish asymptotically.

To circumvent this limitation, we apply each Lie group operator $\hat{A}_h$ within a learnable bijective nonlinear coordinate system, where $\hat{A}_h$ remains nonlinear with respect to our original reference frame, thus satisfying the UAT requirement. We achieve this through a sequential non-linear compression $\hat{\sigma}_h^{-1}$, linear transformation $\hat{A}_h$, and non-linear expansion $\hat{\sigma}_h$. We define the Lie manifold neural architecture acting on incoming signals $X_h \in \mathbb{R}^n$ as the following expression.

$$X_{h+1} = \left(\hat{\sigma}_h \hat{A}_h \hat{\sigma}_h^{-1}\right) \cdot X_h \tag{2}$$

Within equation (2), $\hat{\sigma}_h$ represents a learnable nonlinear activation function that defines a new coordinate system for each linear operator. To prevent successive Lie group transformations from collapsing into a singular operation, we alternate nonlinear projections across successive layers.

$$X_{h+2} = \left(\hat{\sigma}_{h+1}^{-1} \hat{A}_{h+1} \hat{\sigma}_{h+1}\right) \cdot \left(\hat{\sigma}_h \hat{A}_h \hat{\sigma}_h^{-1}\right) \cdot X_h \tag{3}$$

This ensures that each linear transformation remains distinct, with a non-trivial nonlinear component separating successive linear adjustments. To maintain both monotonicity and invertibility across updates, we define $\hat{\sigma}_h$ as a superposition of a linear term and a softsign function.

$$\hat{\sigma}_h(X_h) = l_h X_h + \frac{1}{r_h} \cdot \frac{X_h}{1 + |X_h|} \tag{4}$$

$$\hat{\sigma}_h^{-1}(X_h) = \frac{sign(X_h)}{2}\left[\sqrt{1 + \frac{2(1 + r_h|X_h|)}{r_h l_h} + \frac{\left(r_h X_h - sign(X_h)\right)^2}{r_h^2 l_h^2}} - 1 - \frac{1}{r_h l_h}\right] + \frac{X_h}{2l_h} \tag{5}$$

Within equations (4,5), the linear coefficient l_h stabilizes gradients as softsign converges through a linear scaling factor. Meanwhile, the nonlinear coefficient $\frac{1}{r_h}$ allows the activation function to dynamically adjust its linear and nonlinear regions. For consistency, we restrict both coefficients to positive values, $r_h, l_h > 0$ and bound them to prevent the model from learning unstable or linear activation functions.

Notably, if the model begins learning large, unphysical amplitudes, the activation function collapses into a linear transformation.

$$\lim_{X_h \to \pm\infty} \hat{\sigma}_h(X_h) \approx \pm l_h X_h \tag{6}$$

This prevents uncontrolled growth that destabilizes the model. Similarly, the model can modulate its complexity in deep neural layers by increasing r_h, effectively dampening nonlinearity.

$$\lim_{r_h \to \pm\infty} \hat{\sigma}_h(X_h) \approx l_h X_h \tag{7}$$

In terms of gradient flow, the softsign function was chosen for its smooth asymptotic behavior and bounded first derivative. By superimposing the linear term $l_h X_h$, we maintain a non-zero first derivative at softsign's bounds, preventing vanishing gradients.

$$\hat{\sigma}_h'(X_h) = l_h + \frac{1}{r_h} \cdot \frac{1}{(1 + |X_h|)^2} \tag{8}$$

Gradients are thereby stable in both large and small amplitudes, with a minimum first derivative of l_h.

$$\lim_{X_h \to 0} \hat{\sigma}_h'(X_h) \approx l_h + \frac{1}{r_h} \tag{9}$$

$$\lim_{X_h \to \pm\infty} \hat{\sigma}_h'(X_h) \approx l_h \tag{10}$$

We therefore bound r_h and l_h to maintain a non-linear structure with non-zero gradients that remain stable across training updates.

To capture both long-term and transient temporal structures within physiological signals, we integrated Lie manifold neural architectures within biorthogonal wavelet neural operators (bior 3.1) through the decompositions of the discrete wavelet transform (DWT) in both shared and specific layers. To minimize weights within the specific layers, we stop the decomposition after one dyadic down-sampling, as DWT decomposition levels exhibit spatial redundancies. Meanwhile, we stop the shared layer decompositions after reaching 32 elements, chosen through empirical observations, balancing meaningful temporal information, lossless signal reconstruction, and training efficiency.

6.6.2 Bounding Lie manifold neural architecture parameters

Each free parameter in the Lie manifold neural architecture carries a well-defined mathematical and physical interpretation, allowing us to impose meaningful bounds that ensure stable signal propagation throughout hidden layers. All

parameters were bounded through a hyperbolic tangent function. By leveraging the intrinsic properties of matrix exponentials and the normalized amplitude of incoming signals, these bounds naturally constrained the searchable space within a periodic loss curve. Here, we formally define all assumptions underlying these constraints applied to both the linear and non-linear components.

Lie group transformation, $e^{\hat{S}_h}$*:* The matrix exponential of any skew-symmetric matrix is a part of the special orthogonal group SO(n), representing any arbitrary n-dimensional rotation. For each plane-rotation generator, the path $t \to e^{t\hat{S}_h}$ repeats every 2π seconds, where the range can be constrained to $[-\pi, \pi]$ without loss of generality. However, we can further constrain the weights in $\hat{S}_h$ to $\left[-\frac{\pi}{2}, \frac{\pi}{2}\right]$, as transformations beyond this range yield trivial phase shifts or amplitude inversions, which do not provide much representational power. Empirically, we found transformations generally remained between $\left[-\frac{\pi}{4}, \frac{\pi}{4}\right]$, although not strictly, likely due to adjacent points and similar amplitudes beginning at a $\frac{\pi}{4}$ phase shift within a Givens decomposition. We chose to apply the more restrictive $\left[-\frac{\pi}{4}, \frac{\pi}{4}\right]$ bound, without noticing any decrease is model accuracy. The predominance of angular parameters helps maintain a bounded, periodic loss landscape for stable convergence.

Linear scaling, a_h: Since the rotational parameters do not affect signal magnitudes, the normalization factor a_h solely determines the Lipschitz constant of the linear transformation. Since input signals were normalized between $[-1, 1]$, we constrain a_h between $[0.95, 1.05]$ to prevent large covariant shifts and unphysical intermediate states within each layer. However, more restrictive bounds can be applied for deeper models based on dataset-specific requirements.

Non-linear projection, $\hat{\sigma}_h$: The non-linear projection $\hat{\sigma}_h$, detailed in equation (4), includes both linear and non-linear terms. To maintain stable gradient propagation, we bound the linear coefficient l_h between the interval $[0.1, 0.9]$, which directly enforces a minimum first derivative of ± 0.1 in either direction; however, we note that for broader stability a more restrictive bound of $[0.25, 0.75]$ can enhance training stability. In terms of non-linearity, we find that the transition between predominantly non-linear and linear behaviors occur at $\left|\frac{r_h(1-l_h)-1}{r_h(1-l_h)}\right|$, where the forward and inverse projections intersect, $\hat{\sigma}_h\left(\frac{r_h(1-l_h)-1}{r_h(1-l_h)}\right) = \hat{\sigma}_h^{-1}\left(\frac{r_h(1-l_h)-1}{r_h(1-l_h)}\right)$. To maintain meaningful training dynamics, we constrain this intersection point to $2 \geq \left|\frac{r_h(1-l_h)-1}{r_h(1-l_h)}\right|$, ensuring that the transition remains within the min-max range of incoming signals, which were bounded between ± 1. We note that restricting this bound to $1.5 \geq \left|\frac{r_h(1-l_h)-1}{r_h(1-l_h)}\right| \geq 0.5$ can be beneficial based on dataset-specific requirements. These bounds

enable a controlled and adaptive non-linear projection, while maintaining stable gradient.

6.6.3 Integration of wavelet neural operators

Biorthogonal wavelet neural operators provide multi-resolution temporal insights into biometric signals by generating approximate (low-frequency) and detailed (high-frequency) coefficients that preserve both global and local patterns. This ensures a balanced representation between learning time and frequency information across large temporal scales. Unlike Fourier-based methods, which rely on global sinusoidal basis functions[7], wavelets provide localized transformations that convolve along a signal, making them well-suited for capturing short-lived affective fluctuations in wearable biosignals.

Unfortunately, each decomposition level propagates small precision errors during reconstruction. To ensure numerical stability and lossless reconstruction within our bidirectional model, we employ biorthogonal 3.1 (bior3.1) wavelets, selected for their symmetry, lossless nature, and balanced time-frequency localizations. Biorthogonal wavelets feature two dual wavelet pairs—one for decomposition and another for reconstruction—ensuring numerical consistency with exact reconstruction, which is important in invertible architectures with multiple hidden layers. By leveraging Lie group transformations within wavelet neural operators, this architecture maintains both long-term and short-term temporal attention for learning biologically meaningful features.

6.6.4 Model training

During training, the AMIGOS, DAPPER, CASE, and EMOGNITION datasets were split into 12 batches per epoch with 57, 31, 121, and 34 training instances per batch, respectively, while the WESAD and EMPATCH evaluation datasets were trained with 3 batches per epoch containing 20 and 55 training instances per batch respectively. For the signal embedding, emotion predictions, and human activity recognition models, 12.5% of all the signals and labels were held out for evaluation. For all training models, both the WESAD and EMPATCH datasets were held out for testing after training and evaluating the other four datasets.

A warmup of 10 epochs was applied to all models, where the learning rate of all parameters linearly increased by a factor of ten. The final learning rates of the HP Fourier coefficients and CNN-based generation model were 10^{-2} and $4 \cdot 10^{-4}$ respectively with weight decays of 10^{-4} and $4 \cdot 10^{-6}$ respectively. The angular parameters had a learning rate and weight decay of 0.05 degrees. For averaging basic emotion weights, we used a learning rate and weight decay of 10^{-3}. All normalization and activation parameters had a learning rate and weight decay of 10^{-3}. Training was carried out using the Nesterov-accelerated Adaptive Moment Estimation (NAdam) optimizer, with a momentum decay of 0.001, beta1 of 0.7, and beta2 of 0.8. All angular parameters used a Xavier initialization strategy,

randomly sampled from $uniform\left(\frac{-\pi}{180}\sqrt{\frac{3}{N}}, \frac{\pi}{180}\sqrt{\frac{3}{N}}\right)$ radians for an N-dimensional sequence.

To compare the signal embedding model's output with the fragmented input signals, each predicted hyper-sampled signal was linearly interpolated back to its original timestamps. A smooth L1 reconstruction loss was applied with L2 and L1 behaviors switching at a beta value of 1. To reduce the impact of noisy or isolated artifacts, the four highest loss values per signal were excluded during training. Each epoch had three stages: (1) training the health profile, signal-specific layers, and shared layers; (2) training the signal-specific layers; (3) resetting and regenerating the HP from 32 training epochs (or the maximum number of current epochs, with a minimum of 3 epochs).

For the activity and emotion models, all output distributions were converted to raw logits for cross-entropy loss computation. The final distribution was divided equally into class segments (ignoring any remainders), with each class probability computed as a weighted average of the output profile and a one-dimensional Gaussian distribution defined by a mean at the class center and a standard deviation equal to one-sixth of the class segment's size. Cross-entropy loss with 0.1 label smoothing was applied for both emotion and activity classification. Class weights were assigned based on the inverse frequency of each class, ensuring that less populated classes received higher weights.

After the ten warmup epochs, we began adaptively pruning insignificant angular parameters at the end of each full model pass. For dataset-specific training, angular pruning was performed after the dataset-specific pass as well as health profile regeneration. For shared layers, any angular parameter less than 0.01 degrees was removed. For signal-specific layers, we exponentially increased the threshold from 0.05 degrees (the model's learning rate) to 5 degrees, $threshold = \max(5, 0.05 \cdot epoch^{1.5})$, which was empirically chosen to allow the model time to learn which parameters to remove without overfitting early on.

6.7 Device design and fabrication

6.7.1 Printed-circuit board design of the EMPATCH system

The electronic system of the multimodal biosensing device consists of five main blocks: power management, signal acquisition, electrode multiplexing, skin temperature measurement, and closed-loop heat therapy. The power management block includes an ultra-low dropout voltage regulator (LP3964, Texas Instruments) that provides a stable 3.3V supply for the microcontroller and sensor interfaces. The microcontroller programming and debugging functionality is handled by a USB-to-UART bridge (CP2102, Silicon Labs), allowing seamless communication with the ESP32. The signal acquisition block is designed for multimodal biosensing, including EEG, EOG, and EDA. The EEG measurement system consists of an instrumentation amplifier (INA114, Analog Devices) for differential signal amplification, an operational amplifier (MCP609, Microchip Technology) for additional signal conditioning, and a precision voltage reference

(MAX6106, Maxim Integrated) to ensure stable baseline voltages. The EOG measurement system leverages a biopotential amplifier (AD8232, Analog Devices) for signal acquisition, commonly used for single-lead ECG applications but adapted here for eye-movement detection by changing the low pass filter capacitor from 0.33 uF to 47 uF. The EDA measurement block consists of two operational amplifiers (MCP606, Microchip Technology) configured to measure skin conductance changes, which correlate with physiological arousal.

The electrode multiplexing block enables efficient signal acquisition from multiple electrode sites. This is achieved using an 8-channel analog multiplexer/demultiplexer (74HC4051BQ, Nexperia), which sequentially connects different electrode inputs to the signal processing circuitry, optimizing hardware utilization while maintaining signal integrity. The skin temperature measurement block employs a simple voltage divider circuit with a thermistor, generating an analog voltage output that varies with temperature. This signal is digitized by the microcontroller for real-time monitoring. The closed-loop heat therapy system integrates a heating element controlled via pulse-width modulation (PWM) from the ESP32. To enable high-current switching, an N-channel MOSFET (DMN3731, Diodes Incorporated) is used, allowing the MCU to regulate power delivery efficiently. The microcontroller unit (ESP32-S3 WROOM-1, Espressif Systems) acts as the core of the system, performing real-time signal processing, executing closed-loop control for heat therapy, and handling wireless data transmission via Wi-Fi.

6.7.2 Material fabrication and characterization

To fabricate PSFA-PN, a precursor solution was prepared by mixing 1 ml of PU solution (50 mg ml^{-1} in THF; Texin RxT85A, Covestro) with 0.3 mL of AgNW solution (20 mg ml^{-1} in ethanol; Ag NW-40, ACS Material) and 0.1 ml of 1-butanol. 0.7 ml of this solution was then dropped onto the center of a water bath (200 mm in diameter) containing 5% ethanol to reduce surface tension. The polymer solution spread instantly across the water surface due to the Marangoni effect, forming an ultrathin film at the water–air interface. The film was left to dry for 10 min before being collected using an acrylic frame. The PSFA-PU substrate was fabricated using the same process, except with a PU precursor solution at a concentration of 70 mg ml^{-1} in THF.

The strain-resilient interconnects, composed of a porous liquid metal composite, were fabricated following a previously reported method[40]. Desired sensor and interconnect patterns were defined via laser cutting using a 50-W laser cutter (Universal Laser System). The EMPATCH was assembled by transferring predesigned PSFA-PN electrodes and strain-resilient interconnects onto the ultrathin PSFA-PU substrate, facilitated by Aquasol water-soluble tape. A waterborne PU adhesive (HydroMed D3, AdvanSource Biomaterial) was applied to ensure strong and robust adhesion between the PSFA-PU, interconnects, and substrate under strain.

Scanning electron microscopy (SEM) images were acquired using a ZEISS 1550VP FESEM. Thickness profiles were measured with a Dektak 3ST profilometer (Veeco). Water vapor transmission rates were determined according to ASTM 96 at 22 °C. Mechanical properties were evaluated using a Mark-10 ESM303 tensile tester. Electrical properties and electrode–skin impedance were measured using a CHI 660E electrochemical workstation. Biopotential signals from human subjects were recorded using a PowerLab C system coupled with an FE238 Octal Bio Amp (AD Instruments).

All animal experiments followed protocol approved by the Institutional Animal Care and Use Committee (protocol no. IA23-1800) at California Institute of Technology. In vivo testing was conducted using C57BL/6 mice (The Jackson Laboratory, Bar Harbor, ME, USA). Following anesthesia and analgesia, a 5 mm^2 area of dorsal skin was shaved, and two pieces of 0.5 mm^2 PSFA-PN film were applied to the skin surface and covered with an occlusive dressing.

6.7.3 Biocompatibility evaluation

For biocompatibility evaluation, tissue samples were collected on days 4 and 7 post-application. Samples were fixed in 4% paraformaldehyde at 4 °C overnight, followed by five washes with DPBS. They were then embedded in paraffin, sectioned, and processed for histological staining.

Histological analysis included hematoxylin and eosin (H&E) and immunohistochemistry (IHC) staining. For IHC, tissue sections were incubated

with the primary antibody anti-CD3 [SP7] (ab16669), followed by a secondary goat anti-rabbit IgG H&L antibody (Alexa Fluor® 488). To label macrophages, anti-CD68 [FA-11] (25-0681-82) conjugated with PE-Cyanine7 (Invitrogen) was used. Cell nuclei were counterstained with DAPI. Slides were mounted with ProLong™ Diamond Antifade Mountant (Invitrogen) and imaged using an LSM 800 confocal laser scanning microscope (ZEISS).

6.8 Data collection and therapy protocols

6.8.1 Data collection and therapy protocols

For evaluation of physiological signal changes under various conditions for affectivity applications, subjects were screened based on specific exclusion criteria, including non-English speakers unable to understand affective labels, inability to provide informed consent, medication use affecting psychiatric states, and pre-existing psychiatric or physical illnesses (e.g., depression, anxiety, hypertension, hyperlipidemia, or chronic cardiovascular disease).

To ensure high-fidelity signal acquisition, sensor placement was carefully optimized. EEG electrodes, FP1 and FP2, were placed along the forehead following the 10-20 system, with FP1 referenced against FP2. EDA and temperature sensors were placed near areas with a high concentration of sweat ducts, with high levels of heat modulation. EOG electrodes were placed around the left eye in the vertical direction to collect autonomic eye reactions, which

predominantly appear as blinks. We ignore cases of ocular dysmetria, while screening the subject beforehand for any eye conditions.

Prior to each experiment, participants provided demographic information, details on physiological conditions, and educational background. The EMPATCH device was then securely mounted on the forehead, ensuring precise electrode placement. EEG electrodes were positioned over the left and right frontal regions, with the reference electrode placed on the side of the cheek. EOG electrodes were placed above and below the left eye, with a reference electrode at the center of the forehead. Electrodermal activity (EDA) electrodes were positioned in the frontal region beneath the left frontal EEG electrode. A temperature sensor was placed above the eyebrows, below the right frontal EEG electrode. Additionally, a heating pad and supplementary temperature sensors were positioned at the temple region. Signal acquisition and processing were conducted using a custom circuit board and analyzed in Python (v3.12).

Participants were instructed to sit still, blink naturally, and focus on their emotional state. A 3-minute baseline recording was then conducted, during which physiological signals were continuously recorded. Participants were advised to minimize movement and concentrate on their internal state. Following baseline measurement, they completed the PANAS and STAI-Y1 questionnaires.

Varying experimental conditions. Depending on the assigned condition, participants underwent one of four experimental manipulations: the cold pressor

test, physical exercise, music exposure, or a virtual reality (VR) experience. Specifically, participants were instructed to either (1) fully submerge one hand in an ice-water bath (cold pressor test), (2) engage in cycling on a stationary bike (exercise), (3) listen to music through headphones (music condition), or (4) wear a VR headset (virtual reality condition). Each condition lasted approximately 3 minutes, during which participants were asked to fully engage in the assigned task. Immediately following the experimental phase, participants completed the PANAS and STAI-Y1 questionnaires again. Following each experimental condition, participants entered a 3-minute recovery phase, during which they remained seated, minimizing movement, and focusing on their emotional state. This was followed by a final round of PANAS and STAI-Y1 questionnaire assessments.

The efficacy of each therapy method was validated in a cohort of 10 healthy subjects aged 20–30 years. EMPATCH e-skin device is adhere to the skin on the forehead region with appropriate electrode alignment with the same setup as the EMPATCH dataset collection part.

Prior to each therapy experiment, subjects completed a demographic information form. Each therapy experiment was divided into five distinct phases: baseline, stressor, baseline with therapy, stressor with therapy, and recovery. Each phase lasted approximately 3 minutes. During all phases, subjects were instructed to

focus on their emotional states. Following each phase, subjects completed the PANAS and STAI-Y1 questionnaires.

For heat therapy, a heating pad was laser-patterned from a copper substrate, with temperature regulation controlled by an Arduino Uno Rev3. Before the experimental phases, an optimal temperature was determined based on the subject's feedback to ensure comfort. The therapy experiments proceeded through the five sequential phases: baseline, stressor (cold pressor test), baseline with therapy, stressor with therapy, and recovery followed by questionnaire answering.

In the binaural beats therapy, subjects wore noise-canceling headphones. An optimal binaural frequency was determined by a computational model for each subject, with the beats generated using a base frequency around 400 Hz and a delta frequency in the range of 8–15 Hz to stimulate alpha waves. Like the heat therapy protocol, the experimental phases involved the cold pressor test as the stressor, with binaural beats provided during the therapy phases.

For imagery-based therapy, subjects wore VR glasses that displayed calming nature scenes to promote relaxation. The same experimental protocol was followed, with CPT serving as the stressor and visual imagery as the therapy method during the respective phases. Holograph displays were also used for therapy experiments as another way to display virtual images.

6.8.2 Compilation of affective computing datasets

To support cross-platform generalization within affective computing, we compiled five widely used wearable physiological datasets—AMIGOS, DAPPER, CASE, EMOGNITION, and WESAD. These datasets were selected to capture a broad spectrum of biometric responses across varied sensor locations, physiological modalities, participant demographics, experimental stimuli, sampling frequencies, and emotion annotation strategies. Together, they provide a comprehensive testbed for evaluating both biomarker and emotion agnostic affective profiling.

AMIGOS: The AMIGOS dataset monitored participants viewing emotionally evocative videos in both individual and group settings. The frontal EEG signals (AF3, F3, F4, AF4), aligning with the EMPATCH EEG region, were recorded at 128 Hz using the Emotiv EPOC Neuroheadset. Right-arm ECG (256 Hz) and EDA (128 Hz) signals were collected via the Shimmer 2R platform. Emotion annotations were obtained from the Self-Assessment Manikin (SAM) and Positive and Negative Affect Schedule (PANAS). We integrated the following emotion labels: integer scores (1–9) for arousal, valence, dominance, liking, and familiarity; binary labels (0–1) for neutral, disgust, happiness, surprise, anger, fear, and sadness. These scores were collected from watching “August Rush”, “Love Actually”, “The Thin Red Line”, “House of Flying Daggers”, “The Exorcist”, “My Girl”, “My Bodyguard”, “Silent Hill”, “Prestige”, “Pink Flamingos”, “Black Swan”, “Airplane”, “When Harry Met Sally”, “Mr Beans'

Holiday", "Love Actually", "Hot Shots", "The Descent. Dir. Neil Marshall. Lionsgate. 2005.", "Back to School Mr. Bean. Dir. John Birkin. Tiger Aspect Productions. 1994.", "The Dark Knight. Dir. Christopher Nolan. Warner Bross. 2008.", "Up. Dirs. Pete Docter and Bob Peterson. Walt Disney Pictures and Pixar Animation Studios. 2009.".

DAPPER: The Daily Ambulatory Psychological and Physiological Recording for Emotion Research (DAPPER) dataset captured five consecutive days of affective monitoring in daily environments. Physiological data included heart rate measurements from photoplethysmography (PPG, 20 Hz) and electrodermal activity (EDA, 40 Hz), all recorded using a custom-designed wristband (Psychorus, HuiXin, Beijing, China). Participants self-reported emotional states using the Experience Sampling Method (ESM), prompted six times per day at random intervals. Emotion labels were scored on a 1–5 scale for valence, arousal, upset, hostile, alert, ashamed, inspired, nervous, determined, attentive, afraid, and active. Activity categories were self-annotated, including major-related academic (major), personal interest-related academic (interest), non-academic group (group), and non-academic personal (personal) activities.

CASE: The Continuously Annotated Signals of Emotions (CASE) dataset monitored continuous valence and arousal ratings from 0.5–9.5 through a joystick interface. ECG, blood volume pulse (BVP), EDA, respiration, and skin temperature were recorded at 1000 Hz using Thought Technology sensors placed

on the chest and fingers. Participants were exposed to emotion-inducing video clips labeled amusing, blue screen, boring, relaxed, and scary.

EMOGNITION: The EMOGNITION dataset exposed participants to short film clips labeled amusement, anger, awe, baseline, disgust, enthusiasm, fear, liking, neutral, sadness, and surprise. Blood volume pulse (BVP, 64 Hz), electrodermal activity (EDA, 4 Hz), and skin temperature (4 Hz) were collected via the Empatica E4 wristband. Additional heart information—including BVP (20 Hz) and peak-to-peak intervals (10 Hz)—was acquired from Samsung Galaxy smartwatches. Participants self-reported emotional experiences from 1–5 for awe, disgust, surprise, anger, enthusiasm, liking, fear, amusement, and sadness, and 1–9 for valence, arousal, and motivation.

WESAD: The Wearable Stress and Affect Detection (WESAD) dataset integrates multimodal physiological recordings from both chest-worn (RespiBAN Professional) and wrist-worn (Empatica E4) devices. The RespiBAN captured ECG, EDA, skin temperature, and respiration at 700 Hz. The Empatica E4 provided BVP (64 Hz), EDA (4 Hz), and skin temperature (4 Hz). Participants underwent three primary affective conditions—neutral (magazine reading), stress (public speaking and mental arithmetic), and amusement (comedy video viewing)—with additional meditation and recovery phases. Emotional self-assessments were collected from the PANAS, State-Trait Anxiety Inventory (STAI), and SAM. Emotion annotations were from 1–5 for expressions “I feel at

ease," "I feel nervous," "I am jittery," "I am relaxed," "I am worried," "I feel pleasant"; 1–4 for active, distressed, interested, inspired, annoyed, strong, guilty, scared, hostile, excited, proud, irritable, enthusiastic, ashamed, alert, nervous, determined, attentive, jittery, afraid, stressed, frustrated, happy, sad; and 1–9 for valence and arousal.

We summarize the metadata and EMPATCH distributions within the following table.

Dataset Name	**# of Points**	**# of Emotions**	**# of Activities**	**Platforms**	**Bodily Location**	**Biomarkers**	**Surveys**
AMIGOS	673	12	20	Emotiv EPOC; Shimmer 2R (x2)	Arm; head; finger; ankle;	EEG (AF3, F3, F4, AF4); ECG; EDA	SAM; PANAS
DAPPER	364	12	4	Psychorus	Wrist	PPG; EDA	ESM
CASE	1442	2	5	Thought Technology	Chest; fingers	ECG; BVP; EDA; T; respiration	Joystick module
EMOGNITION	407	12	11	Galaxy watch; Empatica E4	Wrist	EEG; BVP; EDA; T	Custom survey
WESAD	60	32	4	RespiBAN; Empatica E4	Wrist; chest	ECG; EDA; T; respiration; BVP	PANAS; STAI; SAM
EMPATCH	165	30	5	EMPATCH	Head	EOG; EEG; EDA; T	STAI; PANAS

6.8.3 Heat, binaural beats, and imagery-based interventions

Heat therapy has well-documented physiological benefits, improving endothelial function, reducing blood pressure, and enhancing overall cardiovascular health[53,54]. The application of heat activates thermoregulatory pathways within the hypothalamus, which in turn stimulate the parasympathetic nervous system (PNS) and aids in relaxation. By restoring autonomic balance, heat therapy has been shown to effectively reduces stress-related hormones, including cortisol and adrenaline, promoting a state of physiological and emotional calm.

Binaural beats harness auditory processing to modulate brainwave activity by presenting two sinusoidal tones with different frequencies to each ear simultaneously, where the brain perceives a third tone corresponding to the frequency difference between the two inputs. This perceived tone, localized between the ears, is typically chosen to fall within a 1–30 Hz range, aligning with key human EEG frequency bands. Distinct brainwave patterns are closely associated with specific mental states, where modulation has shown potential in inducing measurable changes in cognitive and emotional processes. To promote a state of conscious relaxation, we used a 400 Hz carrier frequency with offsets ranging from 8 to 12 Hz between the ears, corresponding to the alpha brainwave band associated with relaxation and reduced stress.

Image-based mental state intervention utilizes calming and positive visual stimuli, such as natural landscapes or soothing abstract patterns, to evoke feelings

of tranquility and alleviate stress-related thoughts. Exposure to aesthetically pleasing visuals has been shown to reduce activity in the amygdala, thereby attenuating the fight-or-flight response typically triggered by stress. Two prominent theories underpinning the stress-reducing effects of natural imagery are the Attentional Restoration Theory (ART) and Stress Recovery Theory (SRT). ART posits that exposure to nature engages effortless attention, which alleviates attentional fatigue and its associated stress responses. In contrast, SRT suggests that viewing natural scenes promotes parasympathetic involvement leading to physiological relaxation and a shift toward positively affected emotional states. The virtual representation of natural settings, facilitated by immersive virtual environment technologies, has been shown to elicit restorative effects comparable to those experienced in real-world environments.

In addition to the VR platform, we further integrated ChatGPT images within a holographic interface. In this setup, images produced by ChatGPT are directly displayed on a holographic fan, while synchronized audio feedback is provided via the computer's output. The image transfer process is automated using Python's watchdog library, which is monitored for the creation of PNG files. Upon detection, each file is automatically uploaded through a cloud-based service to a remote-control device with an application capable for managing the holographic display including image processing and uploading. Considering the complete processing pipeline, from image generation, file detection, and cloud upload to display update, a delay of approximately 30 seconds is observed

between the initiation of image generation and its corresponding showcase on the holographic fan. Concurrently, as ChatGPT continues to generate images based on dynamic emotional scores and provides real-time audio feedback, the holographic display is also continuously updated.

6.8.4 Mental state intervention algorithm

The efficacy of heat, binaural beats, and VR immersive calming imagery was assessed within 10 healthy participants and followed the EMPATCH protocols described within the subject recruitment, experimental steps, and participant preparation sections above. We drew inspiration from the A* pathfinding algorithm to identify optimal sensory parameters within each condition, defined as a combination of PA, NA, and STAI-S values. The final mental state was a weighted combination of all three values with weight fractions of $w_{PA} = 0.1$, $w_{NA} = 0.1$, $w_{STAI-S} = 0.8$, reflecting the dominant influence of state anxiety on the target distribution. The possible range of all PA (5–25), NA (5–25), and STAI-S (20–80) values were normalized between $[0, 1]$.

To mitigate the cold-start problem, heuristic maps were created by discretizing each intervention parameter into fixed-width bins (e.g. 30–50 °C for thermal intervention). Each bin was initially assigned a heuristic probability based on the expected affect modulation from prior testing, which were mapped onto a gaussian profile to smoothen the probability distribution. These independent heuristics were generated for PA, NA, and STAI-S, which were linearly

combined into the compiled heuristic map. This map provided a prior estimate of which intervention parameters were most likely to yield favorable mental states, serving as an early guide.

To personalize the model to each user, the heuristic map was dynamically updated with new subject-specific trends. Additionally, within each session, the model developed a separate time-dependent subject-specific map based on how the current parameter settings modulated PA, NA, and STAI-S. To prevent outdated data from exerting undue influence, we applied a decay factor modeled after the Ebbinghaus forgetting curve, $W_r = e^{(-\lambda t)}$, where λ was $\frac{1}{7200}\, s^{-1}$, and t was the elapsed time in seconds since the data was recorded. More recent observations thus carried more weight in shaping ongoing parameter selection.

To further support adaptation and prevent the model from becoming overly reliant on initial heuristics, we introduced a dynamic exploration weight α. Early in the session, this term encouraged exploration across the parameter space, even in regions where data was sparse, while slowly decaying to shift emphasis toward exploitation of the learned personalized map. This mechanism helped the algorithm remain flexible to user variability while still converging toward consistent preferences over time.

Optimal intervention parameters were selected by minimizing the compiled personalized and heuristic losses defined over the joint parameter-emotion space.

Unexplored bins were automatically assigned a higher exploration benefit, preventing premature fixation on local optima. At each iteration, the algorithm chose the parameter setting with the lowest overall loss from the combined heuristic and personalized maps, applied the intervention, received feedback on the modulation, and updated the maps accordingly. This loop continued until convergence criteria were met, defined as (1) the probability of selecting a specific parameter bin exceeds 90% relative to all others, and (2) the associated loss value is below 0.2.

Different therapy methods exhibit distinct capabilities in modulating emotions, and no single approach universally induces unidirectional emotional changes. To compare affective scores across trials, we normalized each emotion based on their baseline measurements. By averaging the weighted sums and calculating the difference between positive and negative emotions, we derived a metric quantifying the effectiveness of each therapy in modulating specific emotions.

Across all conditions, VR therapy elicited the most pronounced cumulative changes in PA, NA, and STAI-S (Fig. 5i). Median PA increased by 3.53 and NA decreased by 4.50 from stressor to therapy, with interquartile ranges (IQRs) shifting from (0.02, 5.01) to (−2.01, 2.03) for PA, and from (2.01, 7.01) to (−7.02, −1.01) for NA. STAI-S scores showed the largest overall reduction, dropping from 16.03 to −12.01, with IQR narrowing from (9.96, 22.08) to (−20.13, −1.96). Heat therapy produced smaller but consistent effects: PA increased by 2.01, NA

decreased by 1.51, and STAI-S declined from 9.02 to −2.04. IQRs shifted from (1.03, 5.01) to (−1.98, 1.99) for PA, from (−0.98, 3.01) to (−1.98, 2.01) for NA, and from (5.89, 24.14) to (−5.98, 0.97) for STAI-S. Binaural beats therapy yielded the greatest PA increase (5.04), a moderate reduction in NA (2.52), and a STAI-S drop from 12.49 to −5.93. Here, IQRs shifted from (3.07, 6.22) to (−3.01, −1.14) for PA, from (1.03, 5.02) to (−2.13, 0.37) for NA, and from (7.93, 16.09) to (−8.84, 0.15) for STAI-S.

To evaluate whether each therapy modality was able to alter the subjects' emotional state to a statistically significant degree, we performed a paired *t*-test to compare the user's emotions with and without therapeutic intervention. We define our null hypothesis as having no significant difference, with a mean different μ_0 of 0.

6.8.5 Sensory intervention strategies

Heat therapy. Thermal heating was delivered through a resistive heating pad, which was fabricated on a copper-polyimide substrate via laser ablation. Temperature regulation was controlled by an Arduino Uno Rev3 platform, which was calibrated to deliver temperatures between 35°C and 50°C through IR camera measurements. During initial data collection, an optimal temperature was determined based on the participant's feedback to ensure user-comfort without the risk of burning.

Binaural beats. Binaural beats were administered through noise-canceling AirPods. Sound frequencies were generated in Python (v3.12) using NumPy to create stereo sine-wave signals, the pygame mixer for audio playback, and the wavfile module from scipy for reading and writing 16-bit WAV files at a 44,100 Hz sample rate. During the sessions, a 400 Hz carrier frequency with delta offsets ranging between 8 and 15 Hz was applied between the ears, corresponding to the alpha brainwave band associated with relaxation and reduced stress.

VR immersive imagery. All images were generated using OpenAI's DALL·E 3 Python API and immediately cast to the Oculus Meta Quest 2 VR glasses for viewing. Holographic displays were employed as an alternative to virtual reality goggles, enabling image presentation without a headset. We used the Missyou 3D Hologram Fan Display—a 20.5-inch device featuring 624 high-brightness LED beads that generate vivid, high-fidelity holographic visuals. This device supports WiFi and Bluetooth connectivity, content management through a user-friendly mobile app (compatible with both Android and iOS), remote control, and smart scheduling features for seamless operation. The image transfer process was automated with Python's watchdog library, which monitored newly created image files; upon detection, each file was automatically uploaded via a cloud-based service to the remote-controlled fan. A delay of approximately 30 seconds was observed between image generation and its subsequent display on the holographic fan.

ChatGPT prompts: OpenAI's ChatGPT module was provided with initial instructions before each session, with the following prompt: '"You are a friendly and helpful virtual therapist performing Cognitive Behavioral Therapy. In your first response, introduce yourself and say your name is zenBot (only once). You are having a one-sided therapeutic conversation as you help a user to understand, control, and improve their mental state. You will not directly hear the users' verbal responses, only their state anxiety scores from the STAI-Y1 exam (range: 20 - 80) and positive and negative affects from the PANAS (range: 5 - 25). Do not mention these scores or their emotions back to the user.' Subsequent updates were then provided based on the users' emotions with the following prompt: 'The subject has a State-Trait Anxiety Inventory (STAI) Y1 score of {*STAI score*}. The patient's emotion profile from the STAI survey is {*STAI profile*} and from the PANAS survey is {*PANAS profile*}. Do not mention any of the results from the emotion profiles nor STAI score; instead provide a holistic review as you help a user to understand, control, and improve their mental state. Be extremely concise in your response, no more than 30 seconds.' For image generation, another line was added as follows 'As a friendly and helpful virtual therapist, please think about the subject and generate a relevant image to help them feel better.'

6.9 Conclusion

The EMPATCH platform establishes a unified framework for continuous, closed-loop affective assessment and modulation, built upon a soft, comfortable,

and sweat-permeable bioelectronic interface. By reversibly embedding physiological signals into a shared health profile, the platform leverages Lie manifold neural architectures to support robust activity recognition and affective profiling, even within small and fragmented datasets. Lie architectures preserve biometric temporal properties with intrinsic invertibility, offering a mathematically grounded approach to modeling temporal information.

By addressing the pervasive issue of data fragmentation in wearable sensing, the EMPATCH architecture successfully reconstructed over 118,000 missing data points across 205 biomarkers and achieved 81–98% classification accuracy across six heterogeneous affective datasets. Real-time, context-aware interventions—including thermal, auditory, and immersive VR-based methods—yielded measurable reductions in state-anxiety indicators during pilot sessions involving up to ten participants. These results demonstrate the platform's capacity to adaptively modulate emotional states through personalized and responsive intervention strategies.

Beyond sensory interventions, the Lie manifold framework offers a new foundational intrinsically invertible architecture for interpretable scientific computing, providing intuitive two-dimensional visualizations of deep learning dynamics and weight optimizations. As wearable technologies evolve, future work will focus on expanding sensor modalities, refining closed-loop interventions, and validating EMPATCH in diverse sample cohorts. The Lie

manifold architecture serves as a basis for this generalization by connecting affective information across diverse datasets. These advancements will help transition wearables from passive monitoring tools into active collaborators in emotional health—delivering timely, personalized, and scalable support in everyday settings.

References

1. Chaudhry, B. M. & Debi, H. R. User perceptions and experiences of an AI-driven conversational agent for mental health support. *mHealth* **10**, 22 (2024).
2. Zhang, Z. & Wang, J. Can AI replace psychotherapists? Exploring the future of mental health care. *Front. Psychiatry* **15**, 1444382 (2024).
3. Vos, G., Trinh, K., Sarnyai, Z. & Rahimi Azghadi, M. Generalizable machine learning for stress monitoring from wearable devices: A systematic literature review. *Int. J. Med. Inf.* **173**, 105026 (2023).
4. Schachter, S. & Singer, J. Cognitive, social, and physiological determinants of emotional state. *Psychol. Rev.* **69**, 379–399 (1962).
5. Bechara, A. & Damasio, A. R. The somatic marker hypothesis: A neural theory of economic decision. *Games Econ. Behav.* **52**, 336–372 (2005).
6. Van Kleef, G. A. How emotions regulate social life: The emotions as social information (EASI) model. *Curr. Dir. Psychol. Sci.* **18**, 184–188 (2009).
7. McEwen, B. S. Physiology and neurobiology of stress and adaptation: Central role of the brain. *Physiol. Rev.* **87**, 873–904 (2007).
8. Mongelli, F., Georgakopoulos, P. & Pato, M. T. Challenges and opportunities to meet the mental health needs of underserved and disenfranchised populations in the United States. *Focus J. Life Long Learn. Psychiatry* **18**, 16–24 (2020).
9. Saxena, S., Thornicroft, G., Knapp, M. & Whiteford, H. Resources for mental health: scarcity, inequity, and inefficiency. *The Lancet* **370**, 878–889 (2007).
10. Matsumoto, D. & Willingham, B. Spontaneous facial expressions of emotion of congenitally and noncongenitally blind individuals. *J. Pers. Soc. Psychol.* **96**, 1–10 (2009).
11. Darwin, C. *The Expression of the Emotions in Man and Animals*. (J. Murray, 1904).
12. Ekman, P. & Friesen, W. V. Nonverbal leakage and clues to deception. *Psychiatry* **32**, 88–106 (1969).
13. Vrij, A., Edward, K., Roberts, K. P. & Bull, R. Detecting deceit via analysis of verbal and nonverbal behavior. *J. Nonverbal Behav.* **24**, 239–263 (2000).
14. Ekman, P., Friesen, W. V. & O'Sullivan, M. Smiles when lying. *J. Pers. Soc. Psychol.* **54**, 414–420 (1988).
15. Xu, C. *et al.* A physicochemical-sensing electronic skin for stress response monitoring. *Nat. Electron.* **7**, 168–179 (2024).
16. Xu, C., Solomon, S. A. & Gao, W. Artificial intelligence-powered electronic skin. *Nat. Mach. Intell.* **5**, 1344–1355 (2023).
17. Devlin, J., Chang, M.-W., Lee, K. & Toutanova, K. BERT: Pre-training of deep bidirectional transformers for language understanding. in *Proceedings of the 2019 Conference of the North* 4171–4186 (Association for Computational Linguistics, Minneapolis, Minnesota, 2019). doi:10.18653/v1/N19-1423.
18. Miranda-Correa, J. A., Abadi, M. K., Sebe, N. & Patras, I. AMIGOS: A dataset for affect, personality and mood research on individuals and groups. *IEEE Trans. Affect. Comput.* **12**, 479–493 (2021).

19. Shui, X. *et al.* A dataset of daily ambulatory psychological and physiological recording for emotion research. *Sci. Data* **8**, 161 (2021).
20. Sharma, K., Castellini, C., Van Den Broek, E. L., Albu-Schaeffer, A. & Schwenker, F. A dataset of continuous affect annotations and physiological signals for emotion analysis. *Sci. Data* **6**, 196 (2019).
21. Saganowski, S. *et al.* Emognition dataset: emotion recognition with self-reports, facial expressions, and physiology using wearables. *Sci. Data* **9**, 158 (2022).
22. Schmidt, P., Reiss, A., Duerichen, R., Marberger, C. & Van Laerhoven, K. Introducing WESAD, a multimodal dataset for wearable stress and affect detection. in *Proceedings of the 20th ACM International Conference on Multimodal Interaction* 400–408 (ACM, Boulder CO USA, 2018). doi:10.1145/3242969.3242985.
23. Mironenco, M. & Forré, P. Lie Group decompositions for equivariant neural networks. Preprint at https://doi.org/10.48550/arXiv.2310.11366 (2024).
24. Dinh, L., Sohl-Dickstein, J. & Bengio, S. Density estimation using Real NVP. Preprint at https://doi.org/10.48550/arXiv.1605.08803 (2017).
25. Dinh, L., Krueger, D. & Bengio, Y. NICE: Non-linear independent components estimation. Preprint at https://doi.org/10.48550/arXiv.1410.8516 (2015).
26. Gomez, A. N., Ren, M., Urtasun, R. & Grosse, R. B. The reversible residual network: Backpropagation without storing activations. Preprint at https://doi.org/10.48550/arXiv.1707.04585 (2017).
27. Yoshida, Y. & Miyato, T. Spectral Norm Regularization for Improving the Generalizability of Deep Learning. Preprint at https://doi.org/10.48550/arXiv.1705.10941 (2017).
28. Virmaux, A. & Scaman, K. Lipschitz regularity of deep neural networks: analysis and efficient estimation.
29. Gouk, H., Frank, E., Pfahringer, B. & Cree, M. J. Regularisation of neural networks by enforcing lipschitz continuity. Preprint at https://doi.org/10.48550/arXiv.1804.04368 (2020).
30. Li, Z. *et al.* Fourier neural operator for parametric partial differential equations. Preprint at https://doi.org/10.48550/arXiv.2010.08895 (2021).
31. He, K., Zhang, X., Ren, S. & Sun, J. Identity mappings in deep residual networks. Preprint at https://doi.org/10.48550/arXiv.1603.05027 (2016).
32. Wang, W. *et al.* Neuromorphic sensorimotor loop embodied by monolithically integrated, low-voltage, soft e-skin. *Science* **380**, 735–742 (2023).
33. Kim, Y. *et al.* Chip-less wireless electronic skins by remote epitaxial freestanding compound semiconductors. *Science* **377**, 859–864 (2022).
34. Jiang, Z. *et al.* A 1.3-micrometre-thick elastic conductor for seamless on-skin and implantable sensors. *Nat. Electron.* **5**, 784–793 (2022).
35. Kim, D. H. *et al.* Epidermal electronics. *Science* **333**, 838–43 (2011).
36. Zhao, C., Park, J., Root, S. E. & Bao, Z. Skin-inspired soft bioelectronic materials, devices and systems. *Nat. Rev. Bioeng.* **2**, 671–690 (2024).

37. Xu, Y. *et al.* Phase-separated porous nanocomposite with ultralow percolation threshold for wireless bioelectronics. *Nat. Nanotechnol.* **19**, 1158–1167 (2024).
38. Guan, Y.-S. *et al.* Air/water interfacial assembled rubbery semiconducting nanofilm for fully rubbery integrated electronics. *Sci. Adv.* **6**, eabb3656 (2020).
39. Jung, D. *et al.* Highly conductive and elastic nanomembrane for skin electronics. *Science* **373**, 1022–1026 (2021).
40. Xu, Y. *et al.* Porous liquid metal–elastomer composites with high leakage resistance and antimicrobial property for skin-interfaced bioelectronics. *Sci. Adv.* **9**, eadf0575 (2023).
41. Wilson, P. W. F. *et al.* Prediction of coronary heart disease using risk factor categories. *Circulation* **97**, 1837–1847 (1998).
42. Gustafson, L. W. *et al.* Validity and reliability of State-Trait Anxiety Inventory in Danish women aged 45 years and older with abnormal cervical screening results. *BMC Med. Res. Methodol.* **20**, 89 (2020).
43. Thomas, C. L. & Cassady, J. C. Validation of the state version of the State-Trait Anxiety Inventory in a university sample. *Sage Open* **11**, 21582440211031900 (2021).
44. Vitasari, P., Wahab, M. N. A., Herawan, T., Othman, A. & Sinnadurai, S. K. Re-test of State Trait Anxiety Inventory (STAI) among engineering students in Malaysia: Reliability and validity tests. *Procedia - Soc. Behav. Sci.* **15**, 3843–3848 (2011).
45. Venturella, I., Crivelli, D., Fossati, M., Fiorillo, F. & Balconi, M. EEG and autonomic responses to nociceptive stimulation in disorders of consciousness. *J. Clin. Neurosci.* **60**, 101–106 (2019).
46. Ekman, P. & Friesen, W. V. Constants across cultures in the face and emotion. *J. Pers. Soc. Psychol.* **17**, 124–129 (1971).
47. Ekman, P. An argument for basic emotions. *Cogn. Emot.* **6**, 169–200 (1992).
48. Ravaglioli, R. Music therapy in mental health for illness management and recovery. *J. Music Ther.* **62**, thae022 (2025).
49. Hornik, K., Stinchcombe, M. & White, H. Multilayer feedforward networks are universal approximators. *Neural Netw.* **2**, 359–366 (1989).